united nations
educational, scientific
and cultural
organization

international atomic
energy agency

the
abdus salam
international centre for theoretical physics

H4.SMR/1241-9

"Workshop on Three-Dimensional Modelling
of Seismic Waves Generation and their Propagation"

25 September - 6 October 2000

INTRODUCTORY LECTURES IN SURFACE WAVE SEISMOLOGY

M.H. RITZWOLLER

University of Colorado
Boulder, U.S.A.

Introductory Lectures in Surface Wave Seismology

Prepared for:
The Fifth Workshop on Three-Dimensional Modelling of Seismic Waves:
Generation, Propagation, and their Inversion

International Centre for Theoretical Physics
25 September - 6 October, 2000
Trieste, Italy

Prepared by:
Michael H. Ritzwoller

http://ciei.colorado.edu/ICTP/sw_lectures_00.pdf

September 21, 2000

Table of Contents

1. Foreword

The study of surface wave dispersion was begun independently by *Love* [1911] and *Golitzin* [1912]. Surface wave dispersion studies applied to understanding the structure of the Earth date from the 1920s and 1930s with the early works or *Gutenberg* [1924, 1926], *Jeffreys* [1928, 1935], *Stoneley* [1926, 1928], *Byerly* [1930], *Gutenberg and Richter* [1936], and others. The "modern era" of surface wave dispersion research probably began with the studies of *Press* [1956] and *Press et al.* [1956] and was ushered in by the text of *Ewing et al.* [1957]. The flurry of surface wave studies that took place in late 1950s and continued throughout the 1960s defined "classical dispersion analysis" but is too voluminous to list. However, *Ewing et al.* [1957] presents a review that is relatively complete into the late 1950s, and subsequent reviews were presented by *Oliver* [1962], *Dziewonski* [1971], and *Knopoff* [1972, 1983]. In the 1980s, surface waveform fitting became popular and *Nolet* [1987] and *Snieder* [1993] present reviews. However, classical dispersion studies based on both single-station and multistation or multievent methods continue in common practice today. Most current dispersion studies are little different from those in the 1960s other than that computers are far faster, seismic i nstrumentation has been vastly improved, and there is now much more complete path coverage across most regions of interest. Together, these improvements allow tomographic methods to be applied to very large numbers of surface wave dispersion measurements to produce broadband maps of surface wave dispersion over wide areas.

The purpose of these lectures is to present in some detail a discussion of modern single-station surface wave dispersion analyses, the subsequent estimation of dispersion maps using standard tomographic methods, and the interpretation of these maps in terms of 3-D models of the shear velocity of the crust and uppermost mantle. A particular emphasis will be placed on providing material relevant to performing regional and continental scale surface wave tomography and inversion.

Contemporary studies are distinguished from the earlier studies listed above by their broadbandedness, the relatively high resolution of the dispersion maps, and their large spatial scope. For example, we will show surface wave maps across various regions of the world between 15 s and 200 s period. The measurements, in fact, are regularly obtained down to 8 - 10 s and up to 250 s period. The reliability of the group velocity maps across large regions, however, degrades sharply below 15 s and above about 150-200 s for Rayleigh waves and 100-125 s for Love waves. Surface wave maps at and below 30 s period are particularly important because they provide significant constraints on crustal thickness by helping to resolve Moho depth from the average shear velocity of the crust [e.g., *Das and Nolet*, 1995]. Although there have been numerous studies of surface wave dispersion that have produced measurements of group and/or phase velocities between 10 and 40 s period, these studies have typically been confined to areas of about 15° or less in lateral extent.

There appear to be two main motivations for surface wave studies. First, phase and group velocity maps provide constraints on the shear velocity structure of the crust and uppermost mantle.

New dispersion maps on continental scales that have emerged within the past few years display better resolution and should be more reliable (lower variance and bias) than such maps that are computed from current global models of the crust and mantle. Dispersion maps also summarize huge volumes of data, and provide valuable, transportable data to be used in future inversions for the shear velocity structure of the crust and uppermost mantle. Second, accurate high-resolution group velocity maps, in particular, are useful in monitoring clandestine nuclear tests. These maps guide the identification and extraction of surface waveforms which emanate from small seismic events. The estimation of surface wave magnitude, M_s, is thereby facilitated for use as part of, for example, the $M_s : m_b$ method of discriminating underground explosions from naturally occurring earthquakes [e.g.,*Stevens and Day*, 1985].

The scale lengths on which we will concentrate in these lectures are somewhat unusual in surface wave studies. Most surface wave studies are performed either locally (average path lengths $\Delta <$ 1500 km) or globally ($\Delta >$ 10,000 km). There have been a very large number of relatively narrow band local surface wave studies in Eurasia. Some of these from the last 20 years, segregated coarsely by geographical region, include those in the following lists. In Europe there are the largest number of studies, they include *Nolet* [1977], *Calcagnile and Panza* [1978, 1979, 1980, 1990], *Mueller and Sprecher* [1978], *Calcagnile et al.* [1979, 1985], *Levshin and Berteussen* [1979], *Panza et al.* [1978, 1980], *Neuenhofer et al.* [1981], *Mantovani et al.* [1985], *Snieder* [1988], *Mindevalli and Mitchell* [1989], *Dost* [1990], *Yanovskaya et al.* [1990], *Stange and Friederich* [1993], *Vaccari and Panza* [1993], *Pedersen et al.* [1994], and *Lomax and Snieder* [1995]. In the Middle East, central Asia, and China there are the studies of *Chen and Molnar* [1975], *Knopoff and Fouda* [1975], *Bird and Toksoz* [1977], *Chun and Yoshii* [1977], *Pines et al.* [1980], *Knopoff and Chang* [1981], *Wier* [1982], *Romanowicz* [1982], *Feng et al.* [1983], *Jobert et al.* [1985], *Brandon and Romanowicz* [1986], *Lyon-Caen* [1986], *Bourjot and Romanowicz* [1992], *Levshin et al.* [1992], *Wu and Levshin* [1994], *Levshin et al.* [1994], *Levshin and Ritzwoller* [1995], *Ritzwoller et al.* [1996b], *Zhang* [1997], *Wu et al.* [1997], *Curtis and Woodhouse* [1997], *Griot et al.* [1998]. In northern Asia, surface wave studies are fewer in number but include *Lander et al.* [1985], *Kozhevnikov and Barmin* [1989], *Zeng et al.* [1989], and *Kozhevnikov et al.* [1992]. Dispersion studies performed on a global scale usually are based on waveform fitting. Some of the more recent of these include the studies of *Zhang and Tanimoto* [1993], *Su et al.* [1994], *Laske* [1995], *Trampert and Woodhouse* [1995, 1996], *Laske and Masters* [1996], *Li and Romanowicz* [1996], *Masters et al.* [1996], and *Ekström et al.* [1997]. A review is given by *Ritzwoller and Lavely* [1995].

Recent improvements in resolution and bandwidth result from a mixture of measurements obtained from surface waves which propagate both regionally ($\Delta <$3000 km) and continent-wide ($\Delta >$6000 km). Regionally propagating surface waves provide many of the measurements at the short-period end of the spectrum and improve resolution appreciably. Their use alone, however, would provide rather patchy path coverage, would result in very strong sensitivity to errors caused by event mislocation and azimuthal anisotropy, and would not yield many measurements at periods longer than about 60 s. Utilizing measurements from both the regional and continental scales allows one to combine the best characteristics of regional and global studies and provides a data set that is strongly and differentially sensitive to both crustal and upper mantle structures. Other studies of Eurasia on a continental scale include those of *Patton* [1980], *Feng and Teng* [1983a], *Lerner-Lam and Jordan* [1983], and *Curtis et al.* [1998]. There are, however, advantages to the local- and global-scale studies. Resolution can be better in the local studies, especially those based on multistation or multievent methods, and global studies may be more reliable at long periods at and beyond about 150 s for Rayleigh waves and 125 s for Love waves.

These lecture notes concentrate on the measurement and interpretation of group velocity rather than phase velocity for two main reasons. although phase velocity data are brought into the inversions for ashear velocity model. First, measurements of group velocities are much less sensitive to source effects than phase velocities [e.g., *Knopoff and Schwab*, 1968; *Muyzert and Snieder*, 1996] because they derive from measurements of the wave packet envelopes rather than the constituent phases. This is particularly true at shorter periods and longer ranges. This allows one to use small events for which no moment tensor has been estimated. Second, as Figure 1 shows, group velocity sensitivity kernels are compressed nearer to the surface than the related phase velocity kernels. which should provide further help in resolving crustal from mantle structures. It should be noted that the group velocity maps that are presented here are intrinsically different from group velocity maps derived from the frequency derivative of phase velocity maps or approximate relationships between phase and group velocity. We estimate group velocities on the group envelope rather than the phases that constitute the envelope. Hence group velocities place constraints on the velocity structure of Eurasia independent of phase information.

A number of recent surface wave studies have produced phase velocity maps that possess azimuthal anisotropy [e.g., *Tanimoto and Anderson*, 1985; *Nishimura and Forsyth*, 1988; *Montagner and Tanimoto*, 1990, 1991; *Trampert and Woodhouse*, 1996; *Griot et al.*, 1998] and polarization anisotropy (transverse isotropy, horizontal fast axis). Polarization anisotropy is expressed as a specific differential perturbation to the Rayleigh and Love wave velocities at each spatial point [*Montagner and Nataf*, 1986]. In general, relative to the best fitting isotropic model, polarization anisotropy manifests itself by speeding up the Love wave and slowing down the Rayleigh wave. The estimated maps presented here contain this information and therefore should not be seen as isotropic but rather as transversely isotropic. In many locations, no realistic isotropic model can be found that will simultaneously fit both the Rayleigh and Love waves, especially at periods above about 100 s.

Most of the lectures have already been published elsewhere or will soon appear in print. Chapter 2, which briefly discusses the measurement of group velocities, is taken from Ritzwoller and Levshin [1995]. Chapter 3 on surface wave tomography has been taken from *Barmin et al.* [2000]. The estimation of both isotropic and azimuthally anisotropic tomographic maps is discussed in this chapter. The discussion of the use of perturbation methods in surface wave invesions is the subject of Chapter 4 and derives from *James and Ritzwoller* [1999]. The results of the application of surface wave tomography to estimate group velocity maps is the subject of Chapters 5 - 8, which compose parts of *Ritzwoller and Levshin* [1998], *Vdovin et al.* [1999], *Ritzwoller et al.* [1998], and *Levshin et al.* [2000]. Chapter 9 on the inversion for a 3-D shear velocity model across Central Asia is from *Villasenor et al.* [2000]. Chapter 10, on the construction and use of phase matched filters in monitoring the Comprehensive Nuclear Test-Ban Treaty (CTBT), is from *Levshin and Ritzwoller* [2000].

There are several key assumptions or approximations on which many surface wave dispersion studies rest, including those in the following list: (1) the deviation of ray paths from the great-circles linking the sources to the receivers is small, (2) multipathing is not so severe to inhibit accurate measurements, (3) azimuthal anisotropy is small enough not to contaminate the isotropic maps, (4) mislocations of earthquake epicenters have little effect on dispersion maps, and (5) source phase and group time shifts have little cumulative effect. We refer to errors in these assumptions generically as "theoretical errors." We refer the student to the papers by *Ritzwoller and Levshin* [1998], *Muyzert and Snieder* [1998], and *Levshin et al.* [1999] for a discussion of some of these factors. Some relatively exotic surface wavefield phenomena (multi-pathing, polarization anomalies) have

been discussed recently by *Levshin and Ritzwoller* [1995] and *Levshin et al.* [1994], and we refer the student to these papers for a discussion.

2. Measuring Group Velocities

Summary

We describe methods designed to obtain accurate broadband surface wave dispersion measurements on two spatial/frequency scales: continent-wide (e.g., Eurasia; 15 - 300 s) and regionally (e.g., Central Asia, within 20^0 of KNET; 5 - 50 s). These methods are based on well developed frequency-time and floating-filter analyses, and are included within procedures that utilize relational parametric and waveform database structures with rapid graphics, which allow measurements to be made quickly on relatively large volumes of data from a variety of source regions recorded on heterogeneous networks. These methods have been and continue to be applied systematically to data from a wide variety of global and regional networks to yield Rayleigh and Love wave group velocity, phase velocity, polarization, and amplitude measurements. The complexity of structures in the continental crust and uppermost mantle implies that the crucial problem is to extract the desired signals, related to nearly directly arriving waves that can be interpreted deterministically, from the essentially stochastic interfering multipaths and coda. Experiments are underway to automate this method, which currently depends critically on human interaction.

2.1 Measurement Procedures

Problems associated with the estimation of accurate surface wave characteristics (wave velocities, amplitudes, polarizations) do not change in nature with the spatial scale or frequency band of interest, although they do change in magnitude. The most significant issues concern the accrual of high quality data, the identification and extraction of unwanted signals, and the measurement of the signals of interest.

Data quality from both global and regional networks has improved markedly in the past few years, as exemplified by the record sections shown in Figure 2.2. The main problem to be faced is that continents are structurally complicated. This not only makes interpretation in terms of structural models difficult, but also greatly complicates measurements; or more accurately complicates the identification of the aspects of the waveforms on which measurements are to be applied. Our aim, then, is to extract the signals we desire, related to nearly directly arriving waves that can be interpreted deterministically, from the potentially interfering multipaths and coda that are essentially stochastic in nature. Figures 2.3 and 2.4 demonstrate the analysis procedure, in which unwanted signals, in particular surface wave coda, overtones, and body waves are greatly reduced in the filtered seismogram on which measurements are obtained.

The basic characteristics of the current measurement procedure is based on a long history of

development of surface wave analysis (e.g., Dziewonski *et al.* 1969, 1972; Levshin *et al.*, 1972, 1989, 1992. 1994; Cara, 1973; Russell *et al.*, 1988). The recent innovation is that code has been developed which allows measurements to be made rapidly on relatively large volumes of data from heterogeneous networks and a variety of source regions. The innovations have required the development of rational parametric and waveform database structures (more on below) and the development of relatively rapid graphical routines for human interaction with the data. Some results of the use of this method are described in the following chapters.

The general form of the measurement procedure is as follows. Group velocity - period diagrams for the vertical, radial, and transverse components are constructed. An analyst manually traces the apparent group velocity curve for the Rayleigh wave (on the vertical and radial components) and the Love wave (on the transverse component). Time-variable filters are applied around the selected curve to separate the desired signal from the 'noise'. This results in filtered group velocity - period diagrams for which contamination from interfering signals should be reduced. Group velocity, phase velocity, amplitude, and polarization measurements are automatically obtained on the filtered images. Figures 2.3a and 2.4a attempt to display this procedure.

An unfortunate, but currently still necessary, characteristic of this procedure is that it depends crucially on direct human interaction with potentially large volumes of seismic waveform data. The success of this method is based on the analyst accurately identifying the main dispersion ridge of the fundamental modes, separating the 'direct arrival' from surface wave coda at periods below about 30 seconds, inspecting interpolation near spectral holes, and truncating the measurements appropriately at long periods as the signals weaken. This interaction limits the speed with which the method can be applied, and, therefore, the volume of data that can be processed.

To date (September, 2000), the method has been applied to waveform data from approximately 3000 events globally yielding about 50,000 Rayleigh wave and somewhat fewer Love wave group velocity dispersion curves. The analysis of significantly larger volumes of data will require the automation of the technique. Attempts at automation will be based on initial continent-wide group and phase velocity maps which are currently under development. This will increase the volume of data that can be processed and should result in improved resolution of the group/phase velocity maps at long periods and the resulting structural models, but is far from a trivial problem at periods below about 20 s. Some preliminary results are presented in a later chapter.

2.2 Measurements on a Continental Scale

Due to the high, average efficiency of surface wave propagation across Eurasia, surface wave measurements can be made at periods up to 100 - 150 seconds for earthquakes as small as $M_s = 5.0$ that propagate across the entire continent. Of course, measurements can be extended to longer periods for substantially larger events.

As an example, group velocity measurements for a single station (KEVO, Finland) for one event (Kuril event, 10/9/94, $M_s = 7.0$) are shown in Figure 2.3b for the Rayleigh wave (measured on the vertical and radial components) at periods between about 20 and 300 seconds and for the Love wave at periods between about 30 and 250 seconds. Predictions for the spherical model PREM (Dziewonski and Anderson, 1980) are shown for comparison.

A useful by-product of these analyses are 'cleaned' or 'filtered seismograms'. Figure 2.3b shows a comparison between the raw and filtered seismograms for a single station:event pair. Surface

wave coda, overtones and body waves have been greatly diminished from the cleaned seismograms, making them an ideal target for surface wave fitting techniques during a later stage of this research.

2.3 Measurements on a Regional Scale

On a regional scale at shorter periods, smaller events ($M_s < 5.0$) can be analyzed similarly. KNET, situated in a complex tectonic setting in Central Asia surrounded to the East, West and South by significant seismicity, is a natural site to focus studies of regional scale measurements.

Figure 2.4b presents an example of the analysis of these data. Seven KNET stations were operating during the passage of surface waves from an event in the Qinghai Province, China on 1/17/94 ($\Delta \approx 16$ degrees, $M_s = 4.8$). Rayleigh and Love wave group velocity measurements are shown in Figure 2.4b. Rayleigh wave measurements are quite similar across the array above about 20 seconds period and for Love waves above about 30 seconds period at this azimuth. Variations across the array at shorter periods result both from real differences along the various wave paths near the network and also from Rayleigh - Love interference, which can be significant since the group velocities of the two wave types are similar in this period range. Cleaned and raw waveforms are presented in Figure 2.4c.

2.4 Data Base Structure

We store all waveform and parametric data as well as surface wave measurements are stored in the CSS v. 3.0 relational database (Anderson *et al.*, 1990) plus extensions. The standard relations (affiliation, event, gregion, instrument, network, origin, sensor, site, sitechan, sregion, wfdisc) are augmented with two event relations modified slightly from CSS v. 2.8 (centryd, moment) and three extensions (disp, ftdisc, wfedit). The wfedit relation contains information about the time, duration and nature of waveform problems (e.g., clips, gaps, nonlinearities, interfering events, etc.). The disp and ftdisc relations point to dispersion measurements and group velocity - period images, respectively. For each station:event pair, raw and filtered group velocity images are output and pointed to by the ftdisc relation. Dispersion measurements (group velocity, phase velocity, spectral amplitude, polarization) are output and pointed to by the disp relation. Cleaned or filtered waveforms are output and pointed to by a cleaned wfdisc relation.

2.5 Conclusions

The ability to make relatively rapid and accurate surface wave measurements (phase and group velocities, amplitudes, polarizations) on fairly large volumes of data has allowed us to begin to process systematically surface waves propagating across a number of continents globally, as will be discussed further in other chapters below. These developing data sets provide significantly higher resolution than previous models, which promises more accurate lithospheric models.

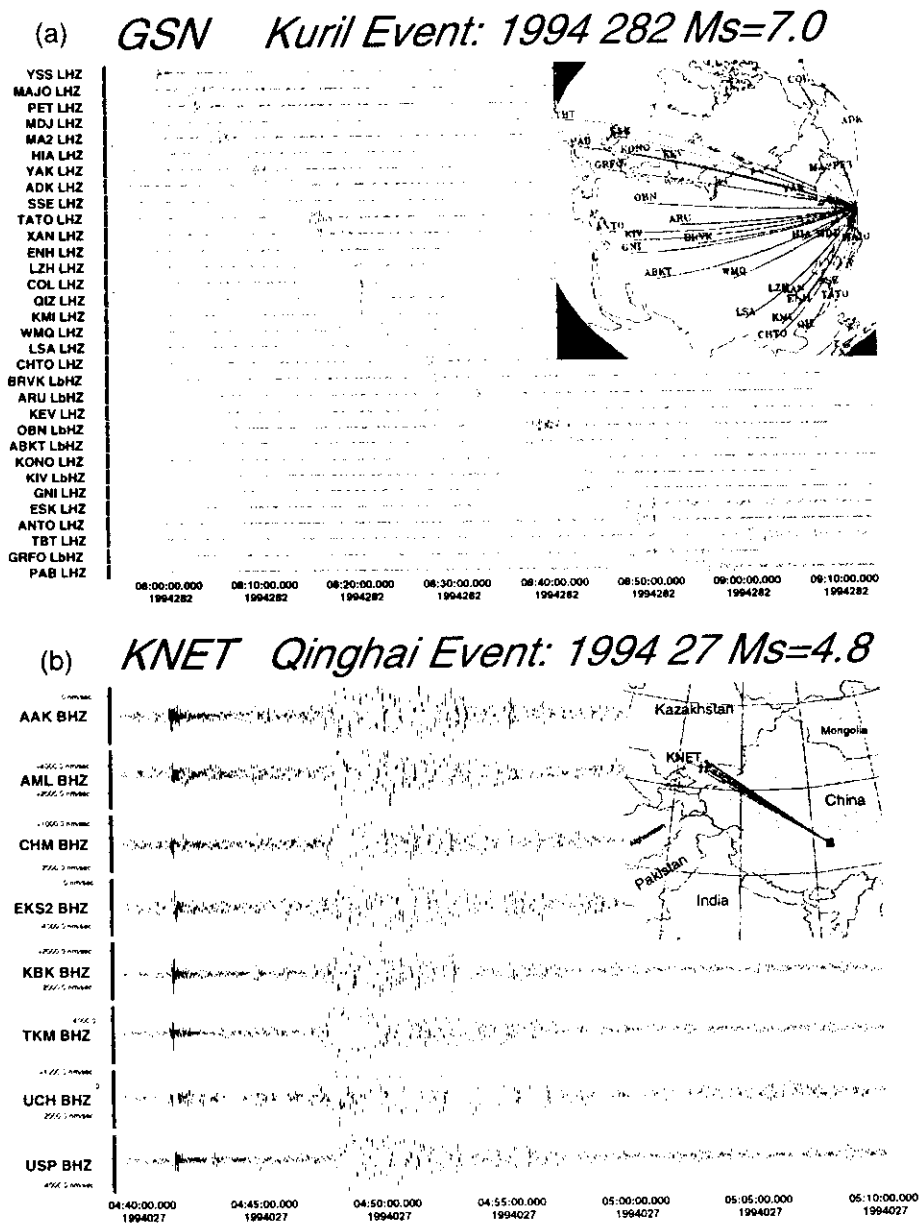

Figure 2.2: (a) Records sections for IRIS/GSN vertical waveforms recorded after the Kuril event sof Oct. 9, 1995 (M_s = 7.0. Waveforms have been low pass filtered with a high frequency corner at 20 s period. (b) Record section of KNET vertical waveforms recorded following the Quinghai, China event of January 27, 1994 (M_s = 4.8).

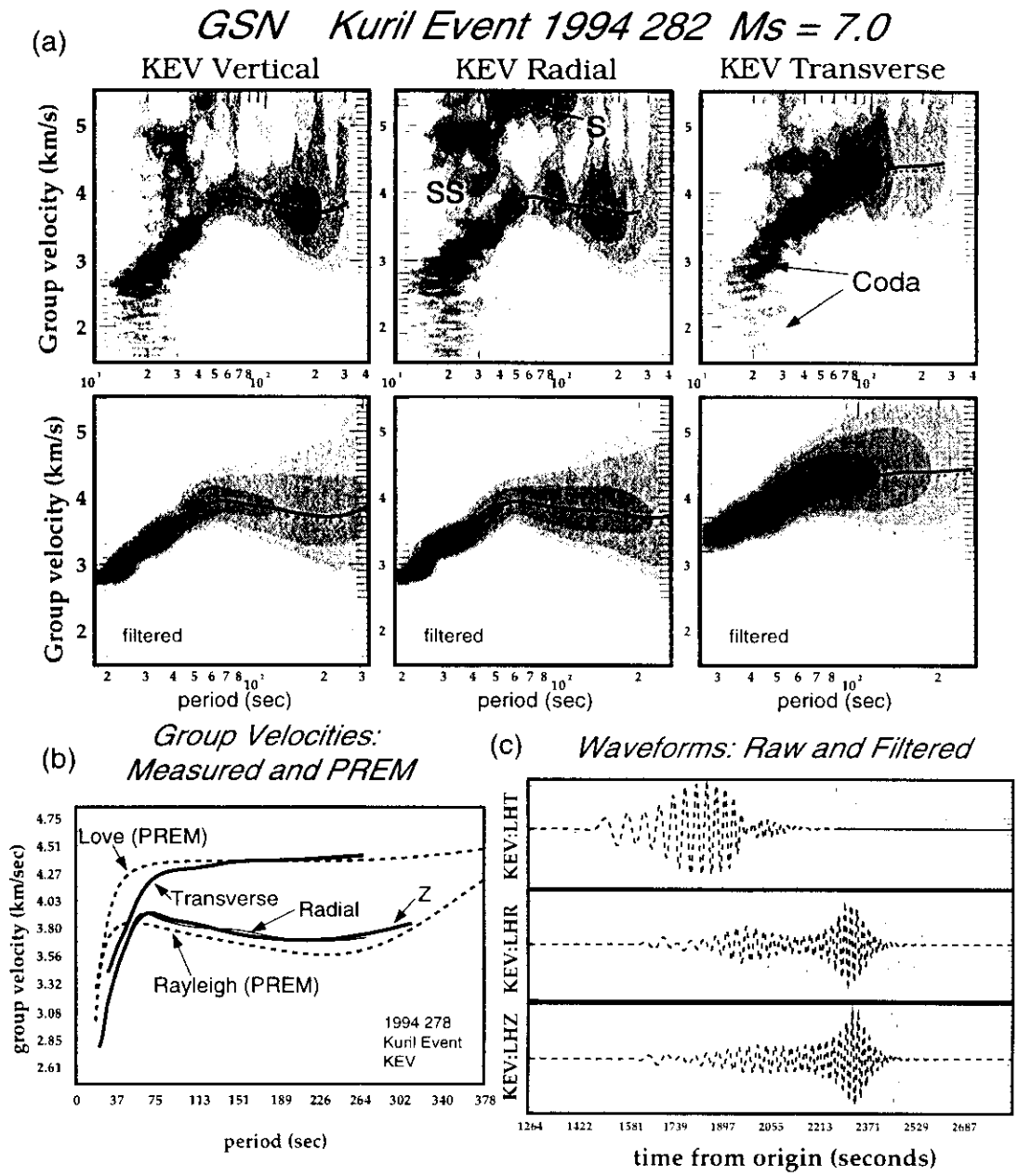

Figure 2.3: (a) Group velocity versus period diagrams for the vertical, radial, and transverse components recorded at the GSN station at Kevo, Finland for an event in the Kuril Islands (Oct. 9, 1994, $\Delta = 58.5°$, $M_s = 7.0$). estimated group velocity curves are shown. (b) Rayleigh and Love wave group velocity measurements compared with the predictions from PREM. (c) Raw (thin solid) and filtered (bold dashed lines) waveforms for KEV.

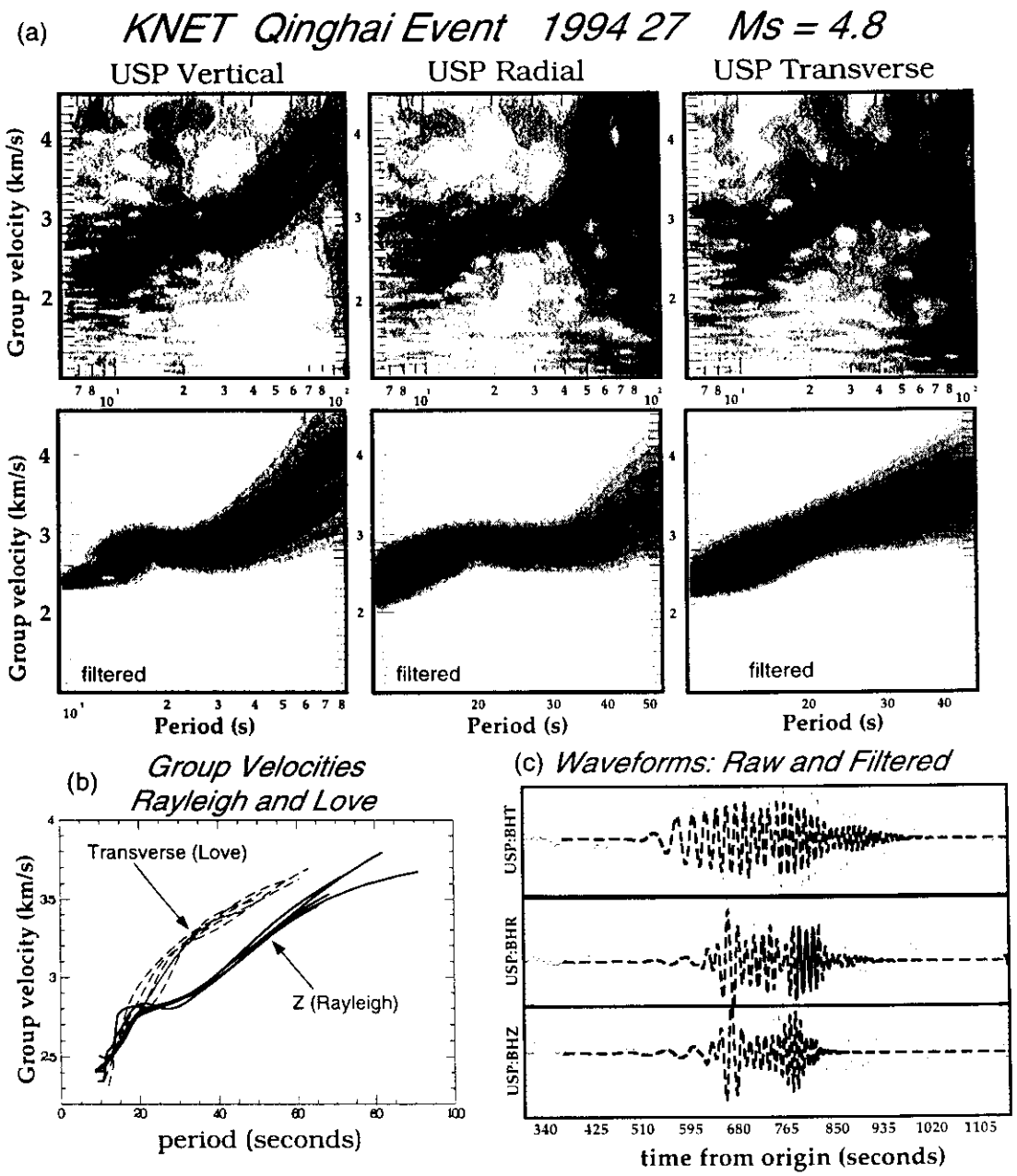

Figure 2.4: (a) Same as Figure 2.3, but for the KNET station USP following an event in the Qinghai Province (Jan. 27, 1994, $\Delta = 16°$, $M_s = 4.8$). (b) Rayleigh and Love wave group velocities measured across the KNET array for the same event. (c) Raw and filtered waveforms for the station USP.

3. Surface Wave Tomography

Summary

We describe a method to invert regional or global scale surface wave group or phase velocity measurements to estimate 2-D models of the distribution and strength of isotropic and azimuthally anisotropic velocity variations. The purpose of this paper is to describe one useful path through the large number of options available in an inversion of surface wave data. Our method appears to provide robust and reliable dispersion maps on both global and regional scales. The technique we describe has a number of features that have motivated its development and commend its use: (1) it is developed in a spherical geometry; (2) the region of inference is defined by an arbitrary simple closed curve so that the method works equally well on local, regional, or global scales; (3) spatial smoothness and model amplitude constraints can be applied simultaneously; (4) the selection of model regularization and the smoothing parameters is highly flexible which allows for the assessment of the effect of variations in these parameters; (5) the method allows for the simultaneous estimation of spatial resolution and amplitude bias of the images; and (6) the method optionally allows for the estimation of azimuthal anisotropy. We present examples of the application of this technique to observed surface wave group and phase velocities globally and regionally across Eurasia and Antarctica.

3.1 Introduction

We present and discuss a method to invert surface wave dispersion measurements (frequency dependent group or phase velocity) on regional or global scales to produce two dimensional (2-D) isotropic and azimuthally anisotropic maps of surface wave velocities. Such "tomographic" maps represent a local spatial average of the phase or group velocity at each location on the map and summarize large volumes of surface wave dispersion information in a form that is both useful and easily transportable. Dispersion information in this form can be applied naturally to a number of problems relevant to monitoring the nuclear Comprehensive Test Ban Treaty (CTBT); for example, (1) to create phase-matched filters (e.g., Herrin & Goforth, 1977; Russell *et al.*, 1988; Leach *et al.*, 1998; Levshin & Ritzwoller, 2000, this volume) designed to detect weak surface wave signals immersed in ambient and signal-generated noise as a basis for spectral amplitude measurements essential to discriminate explosions from earthquakes (e.g., Stevens & Day, 1985; Stevens & McLaughlin, 1997) and (2) in inversions to estimate the shear velocity structure of the crust and upper mantle (e.g., Villaseñor *et al.*, 2000) which is useful to improve regional event locations. The method we discuss here is designed to produce accurate and detailed regional surface wave maps efficiently and reliably, as well as to provide information about the quality of the maps.

The method may be applied, perhaps with a few extensions, to other 2-D inverse problems such as P_n and S_n tomography (e.g., Levshin *et al.*, 2000).

We note, as a preface to further discussion, that the relationship between observed seismic waveforms and an earth model is not linear. Thus, the problem of using surface wave data to constrain the structure of the crust and upper mantle is nonlinear. In surface wave inversions, however, the inverse problem is typically divided into two parts: a nearly linear part to estimate 2-D dispersion maps and a nonlinear part in which the dispersion maps are used to infer earth structure. It is the nearly linear part that we call surface wave tomography and that is the subject of this paper. Some surface wave inversion methods linearize the relation between the seismic waveforms and an earth model (e.g., Nolet, 1987; Snieder, 1988; Marquering *et al.*, 1996) and iteratively estimate the earth model. Therefore, these methods do not estimate dispersion maps on the way to constructing structural models. We take the path through the dispersion maps for the following reasons.

- Surface wave dispersion maps, like a seismic model, summarize large volumes of data in a compact form, but remain closer to the data than the models.
- They are less prone to subjective decisions made during inversion and contain fewer assumptions (both hidden and explicit).
- Because of the foregoing, dispersion maps are more likely than models to be consumed and utilized by other researchers.
- Dispersion maps are directly applicable to detect and extract surface waves from potentially noisy records, which is important in discriminating explosions from earthquakes for CTBT monitoring.

On the negative side, dispersion maps contain only part of the information about earth structure in the seismogram, are the products of inversions themselves, and contain uncertainties due to both observational and theoretical errors.

There are a number of surface wave tomographic techniques currently in use by several research groups around the world. These techniques differ in geometry (i.e., Cartesian versus spherical), model parameterization (e.g., global versus local basis functions), certain theoretical assumptions (particularly about wave paths and scattering), the regularization scheme, and whether azimuthal anisotropy can be estimated simultaneously with the isotropic velocities. Because surface wave tomographic inversions are invariably ill-posed, the regularization scheme is the focal point of any inversion method. There is a large, general literature on ill-posed linear or linearized inversions that applies directly to the surface wave problem (e.g., Tikhonov, 1963; Backus and Gilbert, 1968, 1970; Franklin, 1970; Aki & Richards, 1980; Tarantola and Valette, 1982; Tarantola, 1987; Menke, 1989; Parker, 1994; Trampert, 1998). We do not intend to extend this literature, rather the purpose of this paper is to describe one useful path through the large number of options available to an inversion method. Our method appears to provide robust and reliable dispersion maps on both global and regional scales.

The surface wave tomographic method we describe here has the following characteristics.

- **Geometry:** spherical;
- **Scale:** the region of inference is defined by an arbitrary simple closed curve;

- **Parameterization:** nodes are spaced at approximately constant distances from one another, interpolation is based on the three nearest neighbors;
- **Theoretical Assumptions:** surface waves are treated as rays sampling an infinitesimal zone along the great circle linking source and receiver, scattering is completely ignored;
- **Regularization:** application of spatial smoothness (with a specified correlation length) plus model amplitude constraints, both spatially variable and adaptive, depending on data density;
- **Azimuthal Anisotropy:** may optionally be estimated with the isotropic velocities.

The theoretical assumptions that we make are common in most of surface wave seismology. The method we describe generalizes naturally to non-great circular paths, if they are known, with finite extended Fresnel zones (e.g., Pulliam & Snieder, 1998). The incorporation of these generalizations into surface wave tomographic methods is an area of active research at this time. The use of the scattered wavefield (the surface wave coda) is also an area of active research (e.g., Pollitz, 1994; Friederich, 1998), but usually occurs within the context of the production of a 3-D model rather than 2-D dispersion maps.

The choices of parameterization and regularization require further comment.

3.1.1 Parameterization

There are four common types of basis functions used to parameterize velocities in surface wave tomography: (1) integral kernels (the Backus-Gilbert approach), (2) a truncated basis (e.g., polynomial, wavelet, or spectral basis functions), (3) blocks, and (4) nodes (e.g., Tarantola and Nersessian, 1984). In each of these cases, the tomographic model is represented by a finite number of unknowns. Blocks and nodes are local whereas wavelets and polynomials are global basis functions. (To the best of our knowledge, wavelets have not yet been used in surface wave tomography.) Backus-Gilbert kernels are typically intermediary between these extremes. Blocks are 2-D objects of arbitrary shape with constant velocities and are typically packed densely in the region of study. They are typically regularly shaped or sized, but there are notable exceptions (e.g., Spakman and Bijwaard, 1998; Spakman and Bijwaard, 2000). Nodes are discrete spatial points, not regions. A nodal model is, therefore, defined at a finite number of discrete points and values in the intervening spaces are determined by a specific interpolation algorithm in the inversion matrix and travel-time accumulation codes. Nodes are not necessarily spaced regularly. The ability to adapt the characteristics of these basis functions to the data distribution and other a priori information is a desirable characteristic of any parameterization, and is typically easier with local than with global basis functions. Blocks can be thought of as nodes with a particularly simple interpolation scheme. Thus, we use nodes rather than blocks because of their greater generality.

To date, most surface wave travel time tomographic methods have been designed for global application and have utilized truncated spherical harmonics or 2-D B-splines as basis functions to represent the velocity distribution (e.g., Nakanishi and Anderson, 1982; Montagner and Tanimoto, 1991; Trampert & Woodhouse, 1995, 1996; Ekström *et al.*, 1997; Laske and Masters, 1996; Zhang and Lay, 1996). There are two notable exceptions. The first is the work of Ditmar and Yanovskaya (1987) and Yanovskaya and Ditmar (1990) who developed a 2-D Backus-Gilbert approach utilizing first-spatial gradient smoothness constraints for regional application. This method has been extensively used in group velocity tomography (e.g., Levshin *et al.* 1989; Wu & Levshin, 1994;

Wu *et al.*, 1997; Ritzwoller & Levshin, 1998; Ritzwoller *et al.*, 1998; Vdovin *et al.*, 1999) for studies at local and continental scales. The main problem is that the method has been developed in Cartesian coordinates and sphericity is approximated by an inexact earth flattening transformation (Yanovskaya, 1982; Jobert & Jobert, 1983) which works well only if the region of study is sufficiently small (roughly less than one-tenth of the Earth's surface). Yanovskaya and Antonova (2000) recently extended the method to a spherical geometry, however. The second is the irregular block method of Spakman and Bijwaard (2000).

We prefer local to global basis functions due to the simplicity of applying local damping constraints, the ability to estimate regions of completely general shape and size, and the ease by which one can intermix regions with different grid spacings. For example, with local basis functions it is straightforward to allow damping to vary spatially, but it is much harder to target damping spatially with global basis functions. This spatially targeted damping is a highly desirable feature, particularly if data distribution is inhomogeneous.

3.1.2 Regularization

The term 'regularization', as we use it, refers to constraints placed explicitly on the estimated model during inversion. These constraints appear in the "penalty function" that is explicitly minimized in the inversion. We prefer this term to 'damping' but take the terms to be roughly synonymous and will use them interchangeably. Regularization commonly involves the application of some combination of constraints on model amplitude, the magnitude of the perturbation from a reference state, and on the amplitude of the first and/or second spatial gradients of the model. It is typically the way in which a priori information about the estimated model is applied and how the effects of inversion instabilities are minimized. The strength of regularization or damping is usually something specified by the user of a tomographic code, but may vary in an adaptive way with information about data quantity, quality, and distribution and about the reliability of the reference model or other a priori information. As alluded to above, the practical difference between local and global basis functions manifests itself in how regularization constraints (e.g., smoothness) are applied as well as the physical meaning of these constraints.

As described in section 2, the regularization scheme that we have effected involves a penalty function composed of a spatial smoothing function with a user defined correlation length and a spatially variable constraint on the amplitude of the perturbation from a reference state. The weight of each component of the penalty function is user specified, but the total strength of the model norm constraint varies with path density. Our experience to date is that Laplacian or Gaussian smoothing methods are preferable to gradient smoothing methods. The first-spatial gradient attempts to produce models that are locally flat, not smooth or of small amplitude. This works well if data are homogeneously distributed, but tends to extend large amplitude features into regions with poor data coverage and conflicts with amplitude penalties if applied simultaneously. The model amplitude constraint smoothly blends the estimated model into a background reference in regions of low data density, such as the areas on the fringe the region under study. In such areas the path density is very low, and the velocity perturbations will be automatically overdamped due to amplitude constraints. The dependence on data density is also user specified.

3.2 Surface Wave Tomography

Using ray theory, the forward problem for surface wave tomography consists of predicting a frequency dependent travel time, $t_{R/L}(\omega)$, for both Rayleigh (R) and Love (L) waves from a set of 2-D phase or group velocity maps, $c(\mathbf{r},\omega)$:

$$t_{R/L}(\omega) = \int_p c^{-1}_{R/L}(\mathbf{r},\omega)ds. \tag{3.1}$$

where $\mathbf{r} = [\theta,\phi]$ is the surface position vector, θ and ϕ are co-latitude and longitude, and p specifies the wave path. The dispersion maps are nonlinearly related to the seismic structure of the earth, $\mathcal{M}(\mathbf{r},z)$, where for simplicity of presentation we have assumed isotropy, and $\mathcal{M}(\mathbf{r},z) = [v_s(z),v_p(z),\rho(z)](\mathbf{r})$ is the position dependent structure vector composed of the shear and compressional velocities and density. Henceforth, we drop the R/L subscript and, for the purposes of discussion here, do not explicitly discriminate between group and phase velocities or their integral kernels.

By surface wave tomography we mean the use of a set of observed travel times $t^{obs}(\omega)$ for many different paths p to infer a group or phase velocity map, $c(\mathbf{r})$, at frequency ω. We assume that

$$t^{obs}(\omega) = t(\omega) + \epsilon(\omega),$$

where ϵ is an observational error for a given path. The problem is linear if the paths p are known. Fermat's Principle states that the travel time of a ray is stationary with respect to small changes in the ray location. Thus, the wave path will approximate that of a spherically symmetric model, which is a great-circle linking source and receiver. This approximation will be successful if the magnitude of lateral heterogeneity in the dispersion maps is small enough to produce path perturbations smaller than the desired resolution.

3.2.1 The Forward Problem

Because surface wave travel times are inversely related to velocities, we manipulate equation (7.1) as follows. Using a 2-D reference map, $c_\circ(\mathbf{r})$, the travel time perturbation relative to the prediction from $c_\circ(\mathbf{r})$ is:

$$\delta t = t - t_\circ = \int_p \frac{ds}{c} - \int_p \frac{ds}{c_\circ} = \int_p \frac{m}{c_\circ} ds \tag{3.2}$$

$$m = \frac{c_\circ - c}{c} \tag{3.3}$$

where we have suppressed the $\mathbf{r} = [\theta,\phi]$ dependence throughout and have assumed that the ray paths are known and are identical for both c and $c_\circ$.

For an anisotropic solid with a vertical axis of symmetry, the surface wave velocities depend on the location $\mathbf{r}$ and the local azimuth ψ of the ray. In the case of a slightly anisotropic medium, Smith and Dahlen (1973) show that phase or group velocities can be approximated as:

$$c(\mathbf{r}) = c_I(\mathbf{r}) + c_A(\mathbf{r}) \tag{3.4}$$

$$c_I(\mathbf{r}) = A_0(\mathbf{r}) \tag{3.5}$$

$$c_A(\mathbf{r}) = A_1(\mathbf{r})\cos(2\psi) + A_2(\mathbf{r})\sin(2\psi) + A_3(\mathbf{r})\cos(4\psi) + A_4(\mathbf{r})\sin(4\psi)\ , \tag{3.6}$$

where c_I is the isotropic part of velocity, c_A is the anisotropic part. A_0 is the isotropic coefficient, and $A_1, \ldots, A_4$ are anisotropic coefficients. If we assume that $|c_A/c_I| \ll 1$ so that $(1 + c_A/c_I)^{-1} \approx (1 - c_A/c_I)$, and if the reference model $c_\circ$ is purely isotropic, then by substituting equations (10.5) - (3.6) into (10.4) we get:

$$m \approx \frac{\frac{c_\circ - c_I}{c_I} - \frac{c_A}{c_I} - \left(\frac{c_A}{c_I}\right)\left(\frac{c_\circ - c}{c_I}\right)}{\frac{c_\circ - c_I}{c_I} - \frac{c_A}{c_I^2} c_\circ} \approx \tag{3.7}$$

where the latter equality holds if $|c_A/c_I| \ll 1$ as before. Equation (3.7) can be rewritten as:

$$m(\mathbf{r}, \psi) = \sum_{k=0}^{n} \gamma_k(\psi) m_k(\mathbf{r}), \tag{3.8}$$

where n should be 0, 2 or 4 for a purely isotropic model, a 2ψ anisotropic model, or a 4ψ anisotropic model, respectively, and γ_k and m_k are defined as follows:

$$\begin{array}{ll} \gamma_0(\psi) = 1 & m_0(\mathbf{r}) = (c_\circ(\mathbf{r}) - c_I(\mathbf{r}))/c_I(\mathbf{r}) \\ \gamma_1(\psi) = -\cos(2\psi) & m_1(\mathbf{r}) = A_1(\mathbf{r}) c_\circ(\mathbf{r})/c_I^2(\mathbf{r}) \\ \gamma_2(\psi) = -\sin(2\psi) & m_2(\mathbf{r}) = A_2(\mathbf{r}) c_\circ(\mathbf{r})/c_I^2(\mathbf{r}) \\ \gamma_3(\psi) = -\cos(4\psi) & m_3(\mathbf{r}) = A_3(\mathbf{r}) c_\circ(\mathbf{r})/c_I^2(\mathbf{r}) \\ \gamma_4(\psi) = -\sin(4\psi) & m_4(\mathbf{r}) = A_4(\mathbf{r}) c_\circ(\mathbf{r})/c_I^2(\mathbf{r}). \end{array} \tag{3.9}$$

3.2.2 The Inverse Problem

Our goal is to estimate the vector function $\mathbf{m}(\mathbf{r}) = [m_0(\mathbf{r}), \ldots, m_n(\mathbf{r})]$ using a set of observed travel time residuals d relative to the reference model $c_\circ(\mathbf{r})$:

$$d = \delta t^{obs} = \; t^{obs} - t_\circ = \int_p \frac{m}{c_\circ} ds + \epsilon \tag{3.10}$$

From $\mathbf{m}(\mathbf{r})$ we can reconstruct $c_I, A_1, \ldots, A_4$ for substitution into equations (10.5) - (3.6):

$$c_I = \frac{c_\circ}{1 + m_0} \tag{3.11}$$

$$A_k = \frac{m_k}{1 + m_0} c_I \quad (k \neq 0). \tag{3.12}$$

We define the linear functionals G_i as:

$$G_i(\mathbf{m}) = \sum_{k=0}^{n} \int_{p_i} \left(\gamma_k\left(\psi(\mathbf{r})\right) c_\circ^{-1}(\mathbf{r})\right) m_k(\mathbf{r}) ds, \tag{3.13}$$

By substituting equations (3.8) and (3.13) into equation (3.10) for each path index $(1 \leq i \leq N)$ we obtain the following:

$$d_i = \delta t_i^{obs} = G_i(\mathbf{m}) + \epsilon_i \,. \tag{3.14}$$

To estimate $\mathbf{m}$ we choose to minimize the following penalty function:

$$(\mathbf{G}(\mathbf{m}) - \mathbf{d})^T \mathbf{C}^{-1} (\mathbf{G}(\mathbf{m}) - \mathbf{d}) + \sum_{k=0}^{n} \alpha_k^2 ||F_k(\mathbf{m})||^2 + \sum_{k=0}^{n} \beta_k^2 ||H_k(\mathbf{m})||^2, \tag{3.15}$$

where $\mathbf{G}$ is a vector of the functionals G_i . For an arbitrary function $f(\mathbf{r})$ the norm is defined as: $||f(\mathbf{r})||^2 = \int_S f^2(\mathbf{r})d\mathbf{r}$.

The first term of the penalty function represents data misfit ($\mathbf{C}$ is the *a priori* covariance matrix of observational errors ϵ_i). The second term is the spatial smoothing condition such that

$$F_k(\mathbf{m}) = m_k(\mathbf{r}) - \int_S S_k(\mathbf{r}, \mathbf{r}')m_k(\mathbf{r}')d\mathbf{r}' \ . \tag{3.16}$$

where S_k is a smoothing kernel defined as follows:

$$S_k(\mathbf{r}, \mathbf{r}') = K_{0k} \exp\left(-\frac{|\mathbf{r} - \mathbf{r}'|^2}{2\sigma_k^2}\right) \tag{3.17}$$

$$\int_S S_k(\mathbf{r}, \mathbf{r}')d\mathbf{r}' = 1. \tag{3.18}$$

and σ_k is spatial smoothing width or correlation length. The minimization of the expression in equation (7.3) explicitly ensures that the estimated model will approximate a smoothed version of the model.

The final term in the penalty function penalizes the weighted norm of the model,

$$H_k(\mathbf{m}) = \mathcal{H}(\rho(\mathbf{r}), \chi(\mathbf{r}))m_k, \tag{3.19}$$

where $\mathcal{H}$ is a weighting function that depends on local path density ρ for isotropic structure and a measure of local azimuthal distribution χ for azimuthal anisotropy. Thus, for $k = 0$, $\mathcal{H} = \mathcal{H}(\rho)$ and for $k = 1, \ldots, 4$, $\mathcal{H} = \mathcal{H}(\chi)$. Path density is defined as the number of paths intersecting a circle of fixed radius with center at the point $\mathbf{r}$. For isotropic structure, we choose $\mathcal{H}$ to approach zero where path density is suitably high and unity in areas of poor path coverage. The function $\mathcal{H}(\rho)$ can be chosen in various ways. We use $\mathcal{H} = \exp(-\lambda\rho)$, where λ is a user defined constant. An example is shown in Figure 3.1. To damp azimuthal anisotropy in regions with poor azimuthal coverage, we define $\chi(\theta, \phi)$ to measure the azimuthal distribution of ray paths at point (θ, ϕ). To find χ we construct a histogram of azimuthal distribution of ray paths in the vicinity of (θ, ϕ) for a fixed number n of azimuthal bins in the interval between 0° and 180°, and evaluate the function

$$\chi = \frac{\sum_{i=1}^{n} f_i}{n \max_i f_i}, \tag{3.20}$$

where f_i is the density of azimuths in the ith bin. Values of χ are in the range $1/n \leq \chi \leq 1$. $\chi \approx 1$ characterizes an almost uniform distribution of azimuths, and $\chi \approx 1/n$ is an indicator of the predominance of a single azimuthal direction (large azimuthal gap). We assume that the anisotropic coefficients cannot be determined reliably in regions where χ is less than ~ 0.3. Examples of a χ map and the histogram of azimuthal density, $f(\psi)$, are given in Section 3.4 (Figure 3.8c,d).

Because $\mathbf{m}$ is a perturbation from a reference state, the effect of the third term in the penalty function is to merge the estimated model smoothly and continuously into the isotropic reference state in regions of poor data coverage. In regions of good coverage, this term has no effect so that the only regularization is the smoothness constraint represented by the second term in expression (3.15).

The user supplied regularization constants, α_k and β_k, define the relative strengths of the three terms in the penalty function. The smoothing width or correlation length σ_k is also specified by the user. These parameters should be varied systematically in applying the method. In practice, we often estimate the isotropic and anisotropic maps simultaneously. In this case we normally use slightly different values of all three constants α_k, β_k, σ_k for the isotropic and anisotropic maps to make anisotropic maps more smooth. Typically $\alpha_1 = \alpha_2$ and $\alpha_3 = \alpha_4$, $\sigma_1 = \sigma_2$, $\sigma_3 = \sigma_4$, and $\beta_k = \beta$.

3.2.3 Discretization

The discretization of the equations in the preceding section involves two steps: (1) the formation of a discrete grid and the evaluation of the model on this grid and (2) the discretization of the penalty function. We discuss each in turn.

3.2.3a Grid, Nearest Neighbors, and Interpolation

The goal is to generate a discrete grid with nodes that are approximately constantly spaced on a sphere such that nearest neighbors can be identified and the model evaluated at these points quickly. Significant advances in nonconstant grid generation have been made in recent years by several researchers (e.g., Sambridge, 1995; Spakman & Bijwaard, 1998), particularly for application in 3-D body wave tomography. The tomographic method that we describe is applicable irrespective of grid. However, because path coverage for regional surface waves tends to be less variable than for body waves and surface wave tomography is only in 2-D (e.g., Bijwaard *et al.*, 1998; Van der Hilst *et al*, 1997; Grand *et al.*, 1997; Zhou, 1996), we find that a constant grid is sufficient for our purposes. Generalization to nonconstant grids for surface wave tomography is, however, a useful direction for future research (e.g., Spakman and Bijwaard, 2000).

We create a nearly constant grid on a sphere by performing a central projection onto the sphere of a grid on a reference cube, such that the cube and the sphere share a common center. The advantage of using this reference cube is that nearest neighbors on each of the six faces of the cube are identified trivially. Efficient neighbor identification for interpolation during model evaluation is important for travel time accumulation, which occurs during the construction of the inversion matrix, and in the application of the smoothness constraint. Thus, this method is computationally very efficient because it imposes a natural ordering for the nodes on the sphere, which avoids the need for the creation and use of an adjacency matrix (e.g., Sloan, 1987; Sambridge *et al.*, 1995). To ensure that the distances between nodes on the sphere are approximately constant, the grid on the reference cube must be non-constant. Without providing the details, Figure 3.2 demonstrates the mapping between the face of a cube and the spherical shell related to the face. The current method of grid generation guarantees that the areas defined by adjacent quadruples of nodes on the sphere differ by no more than 10% from the average area. One could produce a mapping with smaller variation in these areas, but this is good enough for our purposes.

The value of the model at each location on the sphere is evaluated from the values at the three nearest nodes. This is done by constructing Delaunay triangles from the set of nodes on the sphere (e.g., Aurenhammer, 1991; Braun and Sambridge, 1997). Each triangle defines a flat plane between the three nodes at the vertices on the plane which is nearly the tangent plane to the sphere. We define a local Cartesian coordinate system on this plane and determine the distances between the point of interest and the three defining nodes approximately. Typical internodal distances, even for

global inversions, are 200 km or less, so this local Cartesian approximation is accurate enough for our purposes. Three-point linear interpolation is used to evaluate the model within each Delaunay triangle. Thus, the value of the model at some arbitrary point $\mathbf{r}$ can be expressed as the weighted sum of the values at the three neighboring nodes:

$$m_k(\mathbf{r}) = \sum_{j=1}^{M} m_k(\mathbf{r}_j) w_j(\mathbf{r}), \tag{3.21}$$

where $\mathbf{r}_j$ are the locations of the M nodes (vortices of triangles) defining the model. The weights $w_j(\mathbf{r})$ are non-zero only inside the triangles surrounding $\mathbf{r}_j$ and linearly depend on two local coordinates inside the Delaunay triangle enclosing $\mathbf{r}$. The weights $w_j(\mathbf{r})$ form the set of the local basis functions such that the values of the basis functions range from 0 to 1 with a maximum value of 1 at the point $\mathbf{r}_j$.

3.2.3b The Inversion Matrix

To construct the inversion matrix, we have to substitute equation (3.21) into expression (3.15). After integrating, the penalty function can be rewritten in matrix form as the sum of two quadratic forms,

$$(\mathbf{Gm} - \mathbf{d})^T \mathbf{C}^{-1} (\mathbf{Gm} - \mathbf{d}) + \mathbf{m}^T \mathbf{Q} \mathbf{m}, \tag{3.22}$$

in which the second term is the regularization condition that includes both smoothness and model norm constraints. Let N be the number of data, n be the isotropic/anisotropic index (0 for isotropic, 2 for isotropic plus 2ψ anisotropic, 4 for isotropic plus both 2ψ and 4ψ anisotropic), and M be the number of nodes defining the model such that $k = 0, \ldots, n$, $i = 1, \ldots, N$, $j = 1, \ldots, M$.

Let us define now our discrete model as a vector $\mathbf{m}$ in the following way:

$$\mathbf{m} = (m_0(\mathbf{r}_1), m_0(\mathbf{r}_2), \ldots m_0(\mathbf{r}_M), \ldots, m_n(\mathbf{r}_1), m_n(\mathbf{r}_2), \ldots m_n(\mathbf{r}_M))^T .$$

Without changing notation we discretize $\mathbf{G}$ to create a $N \times (n+1)M$ matrix in the following way. Let $\mathbf{G}$ to be composed of a set of n submatrices, $\mathbf{U}^k$,

$$\begin{aligned} \mathbf{G} &= \left[\mathbf{U}^0\right] && (n = 0) \\ \mathbf{G} &= \left[\mathbf{U}^0 \vdots \mathbf{U}^1 \vdots \mathbf{U}^2\right] && (n = 2) \\ \mathbf{G} &= \left[\mathbf{U}^0 \vdots \mathbf{U}^1 \vdots \mathbf{U}^2 \vdots \mathbf{U}^3 \vdots \mathbf{U}^4\right] && (n = 4) \end{aligned} \tag{3.23}$$

where $\mathbf{U}^k$ is defined as follows:

$$U_{ij}^k = \int_{p_i} \left(\gamma_k(\psi)\, c_0^{-1}(\mathbf{r})\right) w_j(\mathbf{r})\, ds. \tag{3.24}$$

The $(n+1)M \times (n+1)M$ regularization matrix $\mathbf{Q}$ is the result of discrete numerical integration of the last two terms in equation (3.15), and can be determined in the following way:

$$\mathbf{Q} = \mathbf{F}^T \mathbf{F} + \mathbf{H}^T \mathbf{H}, \tag{3.25}$$

where the smoothing constraint is incorporated within the $(n+1)M \times (n+1)M$ block-diagonal matrix $\mathbf{F}$ as follows:

$$\mathbf{F} = \begin{bmatrix} \alpha_0\mathbf{F}^0 & \dots & 0 & \dots & 0 \\ \vdots & \vdots & \vdots & \vdots & \vdots \\ 0 & \dots & \alpha_k\mathbf{F}^k & \dots & 0 \\ \vdots & \vdots & \vdots & \vdots & 0 \\ 0 & \dots & 0 & \dots & \alpha_n\mathbf{F}^n \end{bmatrix} \tag{3.26}$$

The $M \times M$ matrices $\mathbf{F}^k = \left(F^k_{jj'}\right)$ $(k = 0, \dots, n;\ j, j' = 1, \dots, M)$ are:

$$F^k_{jj'} = \begin{cases} 1 & j = j' \\ -S_k(\mathbf{r}_j, \mathbf{r}_{j'})/p_k & j \neq j' \end{cases}, \quad p_k = \sum_{j'} S_k(\mathbf{r}_j, \mathbf{r}_{j'}). \tag{3.27}$$

The model norm constraint is encoded within the $(n+1)M \times (n+1)M$ matrix $\mathbf{H}$ which consists of $(n+1)$ diagonal matrices $\mathbf{H}^k = \left(H^k_{jj'}\right)$:

$$\mathbf{H} = \begin{bmatrix} \beta_0\mathbf{H}^0 & \dots & 0 & \dots & 0 \\ \vdots & \vdots & \vdots & \vdots & \vdots \\ 0 & \dots & \beta_k\mathbf{H}^k & \dots & 0 \\ \vdots & \vdots & \vdots & \vdots & \vdots \\ 0 & \dots & 0 & \dots & \beta_n\mathbf{H}^n \end{bmatrix} \tag{3.28}$$

where

$$H^k_{jj'} = \begin{cases} \mathcal{H}\left(\rho(\mathbf{r}_j), \chi(\mathbf{r}_j)\right) & j = j' \\ 0 & j \neq j' \end{cases} \tag{3.29}$$

With these definitions the forward problem for the travel time perturbation relative to an isotropic reference model is:

$$\delta\mathbf{t} = \mathbf{G}\mathbf{m}, \tag{3.30}$$

and the estimated model is:

$$\hat{\mathbf{m}} = \mathbf{G}^\dagger\mathbf{C}^{-1}\delta\mathbf{t} \tag{3.31}$$

where the inversion operator, $\mathbf{G}^\dagger$, is defined as follows:

$$\mathbf{G}^\dagger = \left(\mathbf{G}^T\mathbf{C}^{-1}\mathbf{G} + \mathbf{Q}\right)^{-1}\mathbf{G}^T \tag{3.32}$$

3.2.4 Resolution Analysis

We agree with Leveque *et al.* (1993) who argue that the estimation of the resolution matrix is generally preferable to checkerboard tests such as those performed by Ritzwoller and Levshin (1998). Note that from equations (3.30) - (3.32):

$$\hat{\mathbf{m}} = \mathbf{G}^\dagger\mathbf{C}^{-1}\delta\mathbf{t} = \left(\mathbf{G}^\dagger\mathbf{C}^{-1}\mathbf{G}\right)\mathbf{m} = \mathcal{R}\mathbf{m} \tag{3.33}$$

$$\mathcal{R} = \left(\mathbf{G}^T\mathbf{C}^{-1}\mathbf{G} + \mathbf{Q}\right)^{-1}\mathbf{G}^T\mathbf{C}^{-1}\mathbf{G}. \tag{3.34}$$

The matrix $\mathcal{R}$ is the resolution matrix. In this application, each row of $\mathcal{R}$ is a resolution map defining the resolution at one spatial node. Thus, the resolution matrix is very large and the information it contains is somewhat difficult to utilize. We attempt to summarize the information in each resolution map by estimating two scalar quantities at each point: spatial resolution and ampltidue bias.

To estimate spatial resolution we fit a cone to each resolution map. This cone approximates closely the response of the tomographic procedure to a δ-like perturbation at the target node. Figure 3.3a shows a δ-like input perturbation (the local basic function) at the specified spatial location. Figure 3.3b displays the resolution map for that spatial location for the 50 s Rayleigh wave. The cone that best-fits the resolution surface for this point is shown in Figure 3.3c and the difference between the fit cone and the resolution map appears in Figure 3.3d. We define the resolution σ_R as the radius of the base of the fit cone. This value may be interpreted as the minimum distance at which two δ-shaped input anomalies (i.e., Figure 3.3a) can be resolved on a tomographic map. Of course, resolution cannot be less than 2ℓ, where ℓ is the distance between the nodes. In the example in Figure 3.3, nodes are separated by 2 equatorial degrees ($\sim$ 222 km). Therefore, if σ_R is estimated to be less than 2ℓ or 444 km, we redefine resolution as $\sigma_R = 2\ell = 444$ km.

It is also useful to know how reliably the amplitude of the estimated anomalies may be determined. To do this, we apply the appropriate row of the resolution matrix (eq. 33) associated with node (θ_0, ϕ_0) to a test model consisting of a cylinder of unit height with a diameter equal to $2\sigma_R$ centered at (θ_0, ϕ_0). We then define the amplitude of the fit surface as the average amplitude within σ_R of the center of the input cylinder. The relative difference between the input and estimated amplitudes is then taken as the amplitude bias estimate for this point on the map.

Examples of the estimated resolution and amplitude bias are shown in Figure 3.4 for the 20 s Rayleigh wave. Across much of Eurasia, the 20 s Rayleigh wave data yields nearly optimal resolution for a $2^\circ \times 2^\circ$ grid spacing; about 450 km. Amplitude bias at the estimated resolution is typically within about $\pm 10\%$ at each spatial point. Near the periphery of the map where data coverage degrades, estimates of spatial resolution become unreliable but amplitude bias grows rapidly. Thus, amplitude bias is a more reliable means of estimating the reliability of dispersion maps in regions of extremely poor data coverage using the method we describe here.

3.2.5 Computational Requirements

The following formulas summarize computational time (550 MHz, DEC Alpha) and memory requirements for a purely isotropic inversion:

$$t \sim 68\left(\frac{k}{d}\right)^4 \text{ hours} \qquad \text{(computational time in hours)} \tag{3.35}$$

$$M \sim 29\left(\frac{k}{d}\right)^4 \text{ Gb} \qquad \text{(memory usage in Gb)}, \tag{3.36}$$

where k is the fraction of the earth's surface covered and d is the distance between nodes in equatorial degrees. For Eurasian tomography, about half of the earth's surface is covered ($k \sim 0.5$) and $d = 2$ degrees $= 222$ km, thus $t \sim 15$ minutes and $M \sim 115$ Mb.

3.3 Examples of Applications

3.3.1 Preliminaries

The technique described above has been extensively tested using different cell sizes, regularization parameters, and data sets from different regions of the world: Eurasia, Antarctica, South America, and the Arctic. The two conditions necessary for constructing reliable tomographic images are preliminary outlier rejection (data "cleaning") and a careful choice of regularization (or damping) parameters appropriate for a given path coverage.

Data cleaning is based on a two part process. First, we identify outliers in a preliminary way by clustering measurements into summary rays. Second, the resulting data are inverted for an overdamped, smooth tomographic map and outliers are then identified by comparing observed group travel times with those predicted from the smooth map. The usual percentage of the rejected measurements is about 2-3% of all observations.

The choice of regularization parameters is made after several iterations using different combinations of the parameters α_k, β_k, σ_k. The criteria for choosing the best combination are subjective and are based on common sense and some *a priori* information about the region under study. We select a combination of parameters that produces a map free from aphysical features like speckling, streaking, and other artifacts and that also reveals the well known features of the region (sedimentary basins, mountain ranges, etc.) appropriate for the type of map under construction. Ritzwoller & Levshin (1998) describe this procedure in some detail. For example, a typical combination of parameters selected for an isotropic inversion of the 20 s Rayleigh wave data for Eurasia on a $2^\circ \times 2^\circ$ grid is: $\alpha_0 = 800$, $\beta_0 = 1$, and $\sigma_0 = 200$. The resulting maps are relatively insensitive to small (20-30%) changes in the damping parameters. Similar robustness of maps of azimuthal anisotropy to changes in the anisotropy damping parameters was demonstrated by Vdovin (1999) for Antarctica, but in other areas of the world both the pattern and the amplitude of anisotropy change strongly with damping (e.g., Eurasia and the Arctic, Levshin *et al.*, 2000) as discussed further in section 3.4.

3.3.2 Regional Isotropic Group Velocity Maps

Regional group and phase velocity maps have been produced by a number of researchers (e.g., Suetsugu and Nakanishi, 1985; Curtis *et al.*, 1998; Ritzwoller *et al.*, 1998; and many others). Using the protocol described in section 3.1, we have recently constructed a set of isotropic group velocity maps of Eurasia and surrounding areas for Rayleigh and Love waves from 15 s to 200 s period. An example for the 20 s Rayleigh wave is shown in Figure 3.5a. As input data we used 12900 Rayleigh group velocity measurements obtained from records of both global (GSN, GEOSCOPE) and regional (CDSN, CSN, USNSN, MEDNET, Kirgiz and Kazak networks) networks. The basic characteristics of the measurement procedure, data control and weighting are described in detail in Ritzwoller & Levshin (1998). Because 20 s Rayleigh waves are most sensitive to upper crustal velocities, the corresponding group velocity map clearly shows the significant sedimentary basins across Eurasia and on the periphery of the Arctic Ocean as low velocity anomalies (e.g., Barents Sea shelf, western Siberian sedimentary complex, Pre-Caspian, South Caspian, Black Sea, Tadzhik Depression, the Tarim Basin, Dzhungarian Basin, Ganges Fan and Delta, etc.) There is qualitative agreement between the observed group velocity map and the prediction of a hybrid model composed

of crustal structure from the model CRUST5.1 (Mooney *et al.*, 1998) and mantle velocities from the model S16B30 (Masters *et al.*, 1996). The comparison is shown in Figures 3.5b,c. The estimated r.m.s. group velocity misfit at 20 s period is significantly less for our maps (0.08 km/s) than for the map computed from the model CRUST5.1/S16B30 (0.14 km/s). The numbers for the 50 s Rayleigh wave are correspondingly 0.05 km/s and 0.16 km/s. Similar results are reported by Ritzwoller and Levshin (1998) which used the tomographic method of Ditmar & Yanovskaya (1987).

Figure 3.6 presents group travel time correction surfaces for the 40 s Rayleigh wave for several stations in Central Asia. These surfaces summarize travel time information in group velocity maps to be used to improve detection and discrimination schemes in nuclear monitoring (Levshin & Ritzwoller, 2000, this volume). Levshin & Ritzwoller (2000) also present an example of travel time correction surfaces for the 20 s Rayleigh waves.

3.3.3 Global Isotropic Phase Velocity Maps

The tomographic method described above identifies the region of interest by requiring the user to define a simle closed curve on the sphere and identify a single point outside the contour that distinguishes the inside from the outside of the region of interest. If the contour is a very small circle surrounding the point, then the region of interest becomes nearly the entire sphere. In this way, our method can be used to produce global tomographic maps on a regular grid. An example is shown in Figure 3.7a, in which we have inverted the 100 s Rayleigh wave phase velocity data of Trampert and Woodhouse (1995, 1996). Trampert and Woodhouse's map is shown in Figure 3.7b, where they used spherical harmonics up through degree and order 40. The major features of these maps are nearly identical. We have chosen the damping parameters, however, to accentuate smaller scale features than those apparent in the spherical harmonic parameterization. There is much signal remaining in the data set of Trampert and Woodhouse to be fit by smaller scale features than those apparent in Figure 3.7b. For example, the rms misfit to Trampert and Woodhouse's data produced by the map in Figure 3.7a is about 8.1 s compared with the 10.8 s produced by the spherical harmonic map in Figure 3.7b; about a 40% reduction in variance.

3.3.4 Azimuthal Anisotropy

We follow the majority of the studies of azimuthal anisotropy and our discussion above (equations (4) - (6)) by parameterizing azimuthal anisotropy for group velocity as:

$$U(\mathbf{r},\psi) = U_0(\mathbf{r}) + U_1(\mathbf{r})\cos 2\psi + U_2(\mathbf{r})\sin 2\psi + U_3(\mathbf{r})\cos 4\psi + U_4(\mathbf{r})\sin 4\psi, \tag{3.37}$$

where U_0 is isotropic group velocity at spatial point $\mathbf{r} = (\theta, \phi)$, U_1 and U_2 define the 2ψ part of azimuthal anisotropy, and U_3 and U_4 the 4ψ part of azimuthal anisotropy.

Figure 3.8 presents examples of the 2ψ component of group velocity azimuthal anisotropy for the 50 s Rayleigh wave across Antarctica and the surrounding oceans. We took the approximately 2200 observations and divided them into two separate sets of about 1100 measurements each which we then inverted separately for the two maps in Figure 3.8a,b. Both maps display spatially smooth anisotropy patterns, and the fast axes at many locations tend to be parallel to the directions of plate motions. The main features of the maps are similar, but there are differences in detail. In order to quantify the correlation between these two 2ψ maps we use the coherence function defined by Griot

et al. [1998] which takes into account differences in the fast axes directions ($\alpha_1(\theta,\phi)$, $\alpha_2(\theta,\phi)$) and the amplitudes ($A_1(\theta,\phi)$, $A_2(\theta,\phi)$: $A = (U_1^2 + U_2^2)^{1/2}$) of the two maps. The coherence K as a function of rotation angle α, varying between $-90°$ and $90°$, is defined as follows:

$$K(\alpha) = \frac{\sum_{\theta}\sum_{\phi} A_1(\theta,\phi)\ A_2(\theta,\phi)\ \sin\theta\ \exp\left(-\dfrac{(\alpha_1(\theta,\phi) - \alpha_2(\theta,\phi) + \alpha)^2}{2D_{cor}^2}\right)}{\left(\sum_{\theta}\sum_{\phi} \sin\theta\ A_1^2(\theta,\phi)\right)^{1/2}\left(\sum_{\theta}\sum_{\phi} \sin\theta\ A_2^2(\theta,\phi)\right)^{1/2}}. \tag{3.38}$$

Here D_{cor} is the uncertainty in the anisotropic direction, and was set to equal 10°. The resulting curve is shown in Figure 3.9. It is evident that the two maps are correlated, and the average absolute difference in orientation of the fast axes across the maps is less than 20°. The low value of the maximum coherence (~ 0.45) reflects differences in amplitudes of the anisotropic coefficients between the two maps.

The azimuthal coverage of the region is illustrated by Figure 3.8c where the behavior of the function $\chi(\theta,\phi)$ defined by equation (7.7) is shown. The area in which $\chi > 0.3$ covers about 60% of the region. An example of a histogram of azimuthal distribution for a single point is shown in Figure 3.8d. In the vicinity of this point, $\chi = 0.53$ which indicates a small azimuthal gap and acceptable azimuthal coverage.

The estimated maps, in addition, correlate fairly well with the global phase velocity maps of Trampert and Woodhouse (1996), particularly for the Rayleigh 50 s and 100 s period maps, but there are notable differences.

In summary, across Antarctica and the surrounding oceans azimuthal anisotropy appears to be a fairly robust observable. Across Eurasia and the Arctic this is not true, however. We find that similar data subsetting and arbitrary changes in damping and parameterization can produce substantial changes in both the pattern and amplitude of the estimated anisotropy (e.g., Levshin *et al.*, 2000). Although azimuthal anisotropy can be rapidly and efficiently estimated with the algorithm described above, it remains a difficult target to estimate reliably with surface wave data, particularly in continental regions.

3.4 Conclusions

We have described a rapid method for constructing surface wave tomographic maps on local, regional or global scales. Extensive testing of this technique on data sets obtained from a variety of regions around the globe have confirmed its efficiency in producing detailed and reliable surface wave group and phase velocity tomographic maps together with useful measures of map quality.

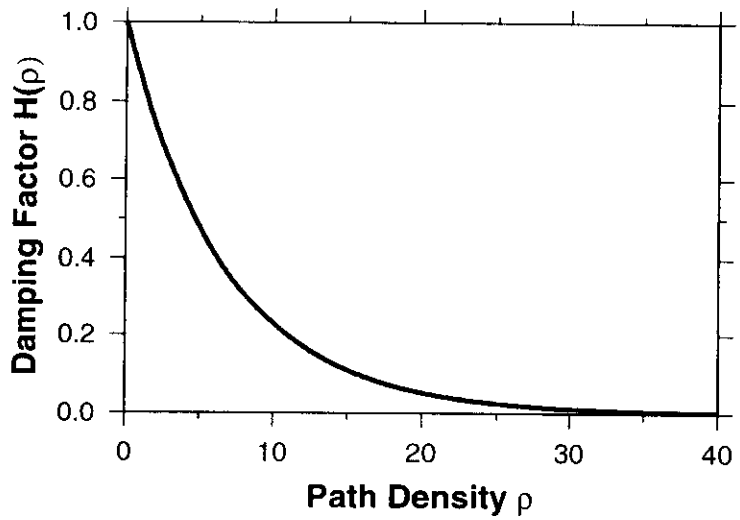

Figure 3.1: Example of the model norm weighting function, $\mathcal{H}(\rho)$ that we commonly use; e.g., as Figure 3.5. Here we choose the constant $\lambda \sim 0.147$ so that when path density (ρ) is less than about 20 paths per 50,000 km^2 damping toward the input reference model becomes increasingly strong.

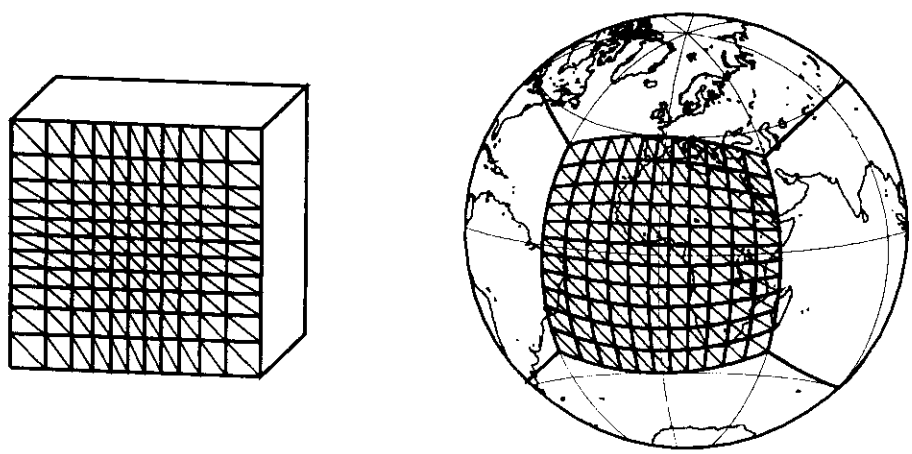

Figure 3.2: An example of the Delaunay triangulation on a sphere by defining a variable triangular grid on a reference cube and performing a central projection of the grid onto the sphere.

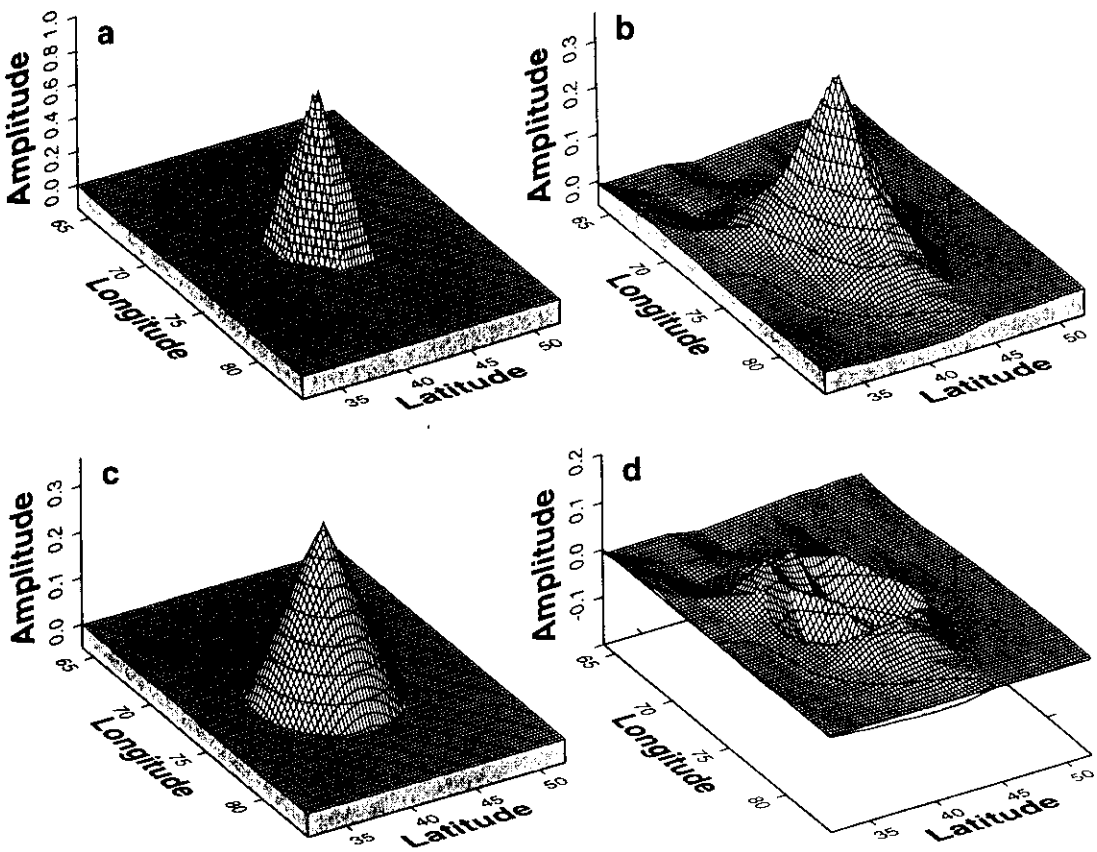

Figure 3.3: Graphical description of the resolution analysis. (a) Minimum sized function that can be estimated with a 2° × 2° grid. The function is centered at 42°N latitude and 73° E longitude. (b) The row of the resolution matrix (a resolution map) for the point specified in (a) for the 50 s Rayleigh wave. (c) The cone that best fits the row of the resolution matrix shown in (b). A comparison of (a) with (b) and (c) demonstrates the spatial spreading produced in the tomographic procedure. (d) The difference between the resolution map and the best fitting cone.

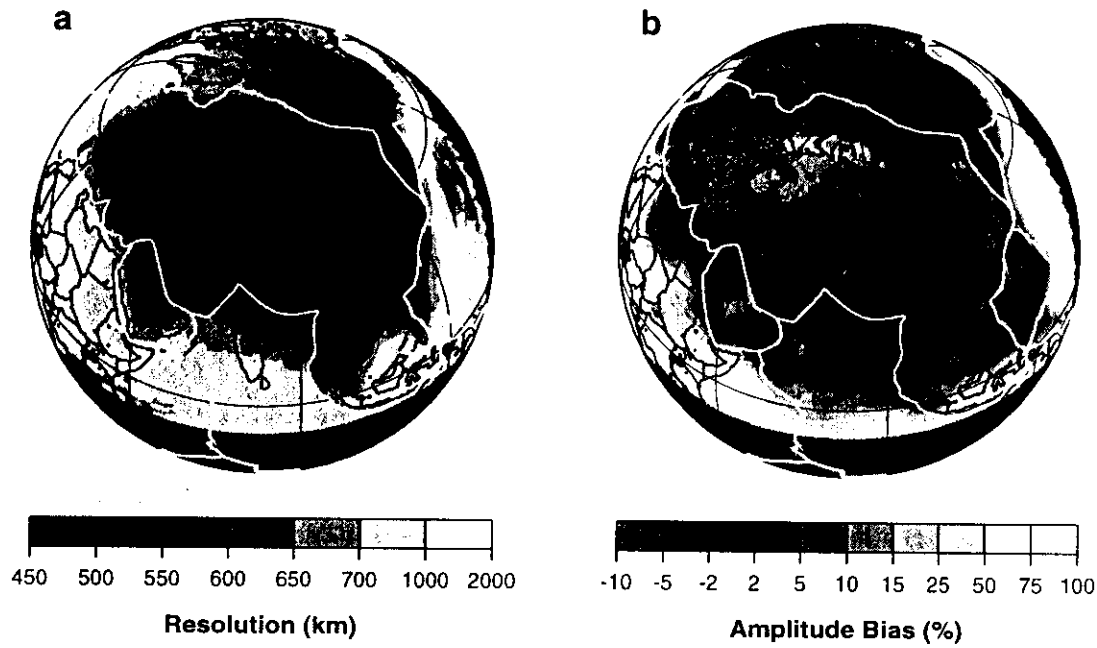

Figure 3.4: (a) Spatial resolution in km for the 20 s Rayleigh wave across Eurasia. Resolution depends on data coverage. In the central part of Eurasia the resolution is high ($\sim$ 450 – 500 km) in areas of high path density and degrades rapidly on the periphery of the region where path density (Figure 3.5d) is low. (b) Amplitude bias for Rayleigh waves at 20 s period. Units of amplitude bias are percent such that 0% means that the cylindrical test function's amplitude has been fully recovered upon inversion. Amplitude bias across the region varies between about $\pm$10% depending on path coverage.

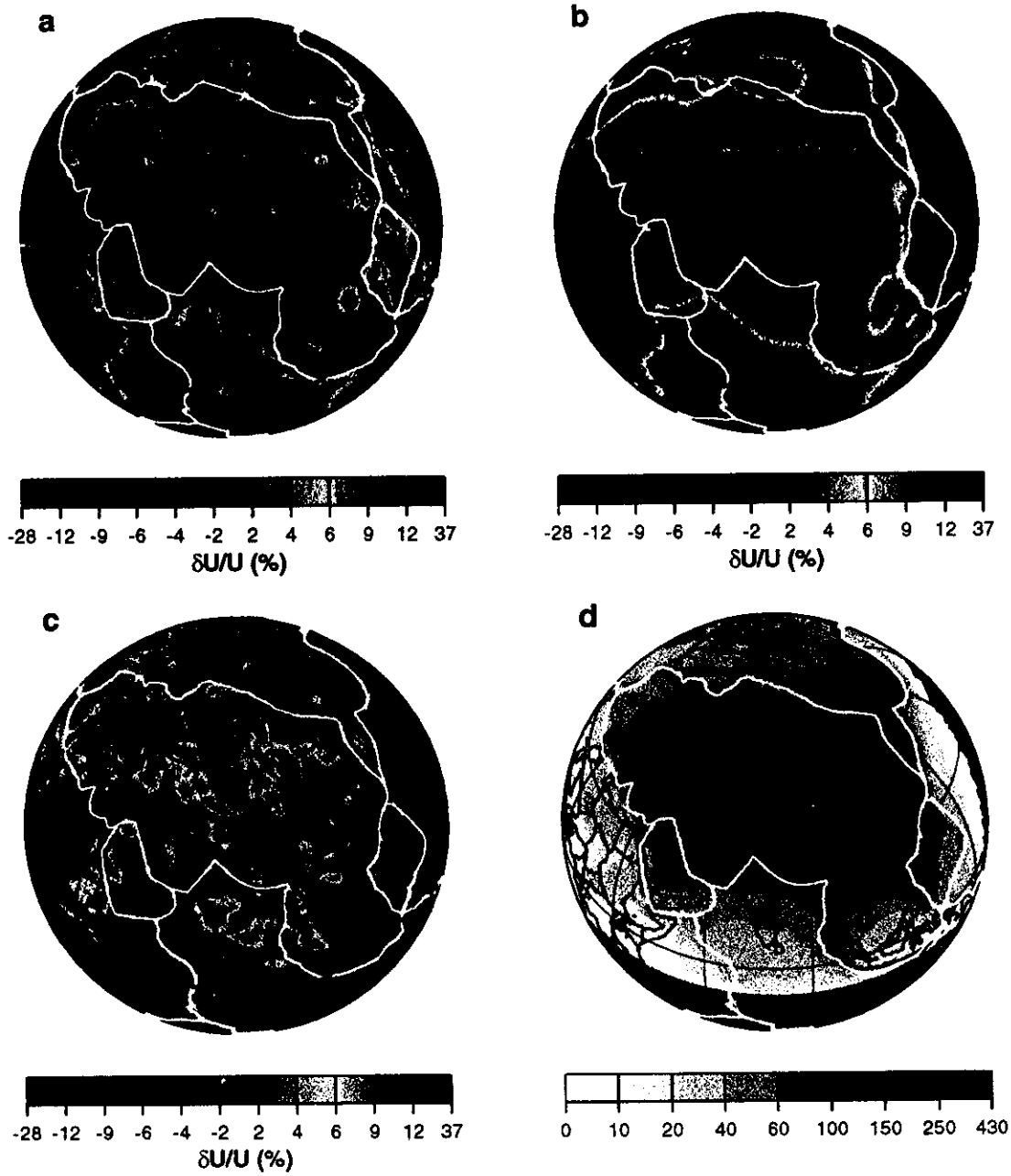

Figure 3.5: (a) The group velocity map across Eurasia for the 20 s Rayleigh wave using the method described in this paper. A 2° × 2° grid is used. (b) The group velocity map computed from the smoothed version of the model CRUST5.1/S16B30. Maps (a) and (b) are plotted in percent relative to the same average velocity. (c) The difference between maps (a) and (b) relative to the same average in (a) and (b). (d) Path density, defined as the number of rays intersecting a 2° square cell ($\sim 50,000$ km^2). White lines are plate boundaries. The red lines show the contour of 20 paths per 50,000 km^2. Inside this contour we have the greatest confidence in the estimated maps. Outside it, model norm damping begins to take effect.

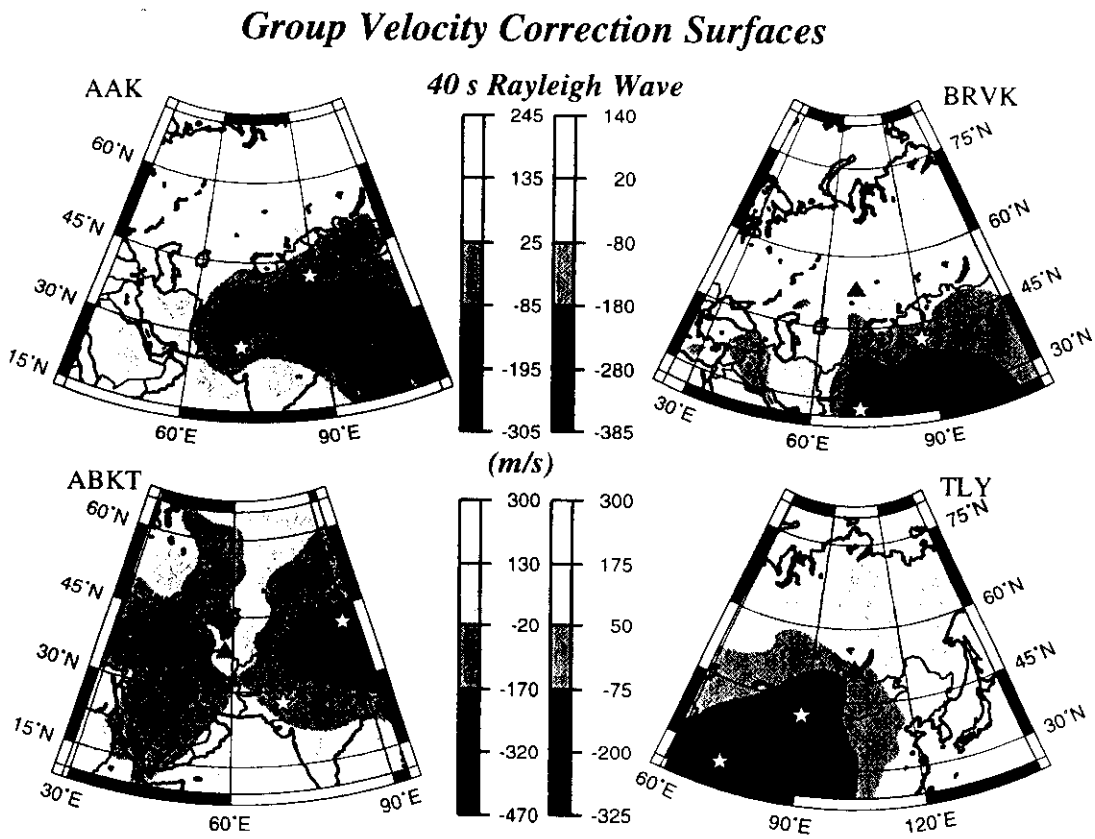

Figure 3.6: Group velocity correction surfaces for four stations in Central and Southern Asia for the 40 s Rayleigh wave. For each geographical point, the maps define the group velocity perturbation that should be applied to a 40 s Rayleigh wave observed at a station if an event were located at the chosen point. Perturbations are relative to the group velocity at the station. Units are m/s. The locations of the Chinese and Indian test sites are indicated with stars.

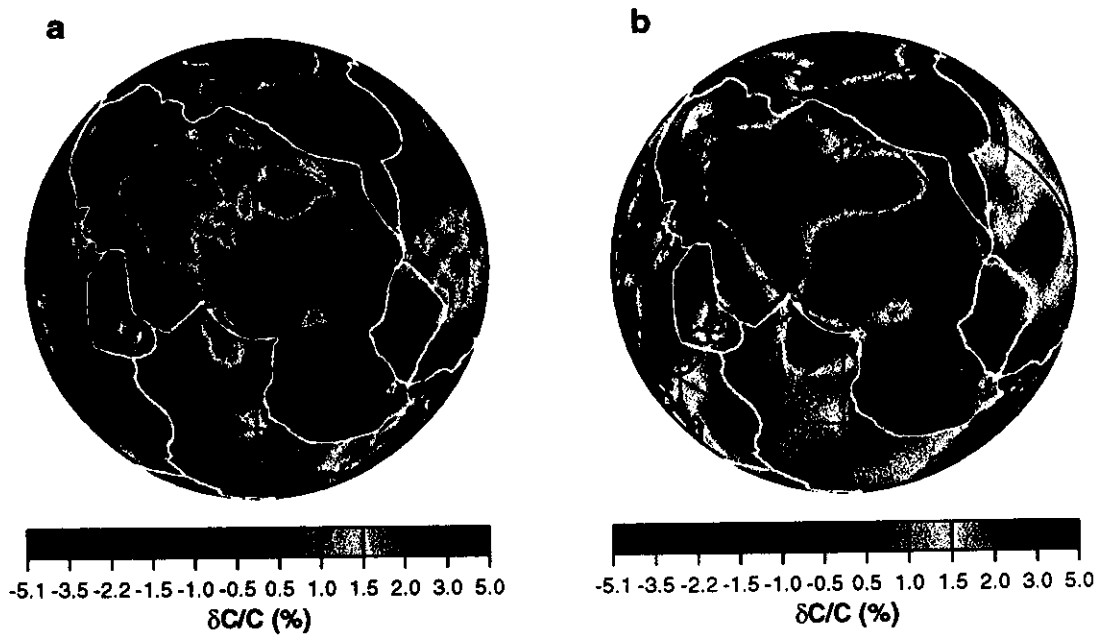

Figure 3.7: (a) Global 100 s Rayleigh wave phase velocity map estimated with the procedure described in this paper using the data of Trampert and Woodhouse (1995, 1996). (b) Trampert and Woodhouse's map using a degree 40 spherical harmonic parameterization using the same data as in (a).

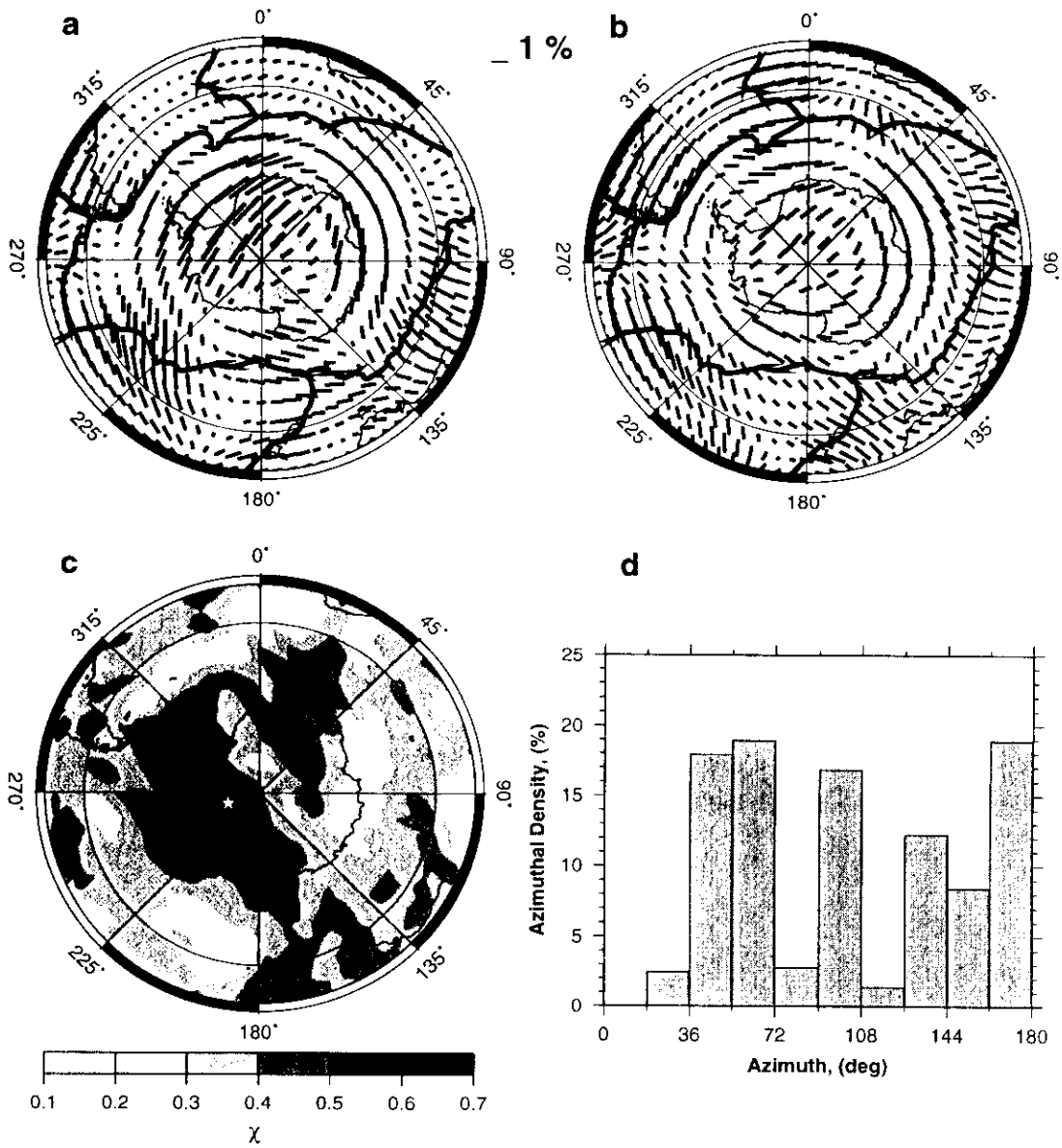

Figure 3.8: (a) and (b). The 2ψ component of the 50 s Rayleigh wave group velocity anisotropy across Antarctica and the surrounding oceans. Results from two equal data subsets of about 1100 measurements each are shown for comparison. (c) Distribution of the function $\chi(\theta, \phi)$ characterizing the azimuthal coverage for the whole set of 2200 Rayleigh wave paths. (d) Histogram of azimuthal distribution at the fixed point $\theta = 173°$ (83°S), $\phi = 267°$ (93°W) shown by the star in (c).

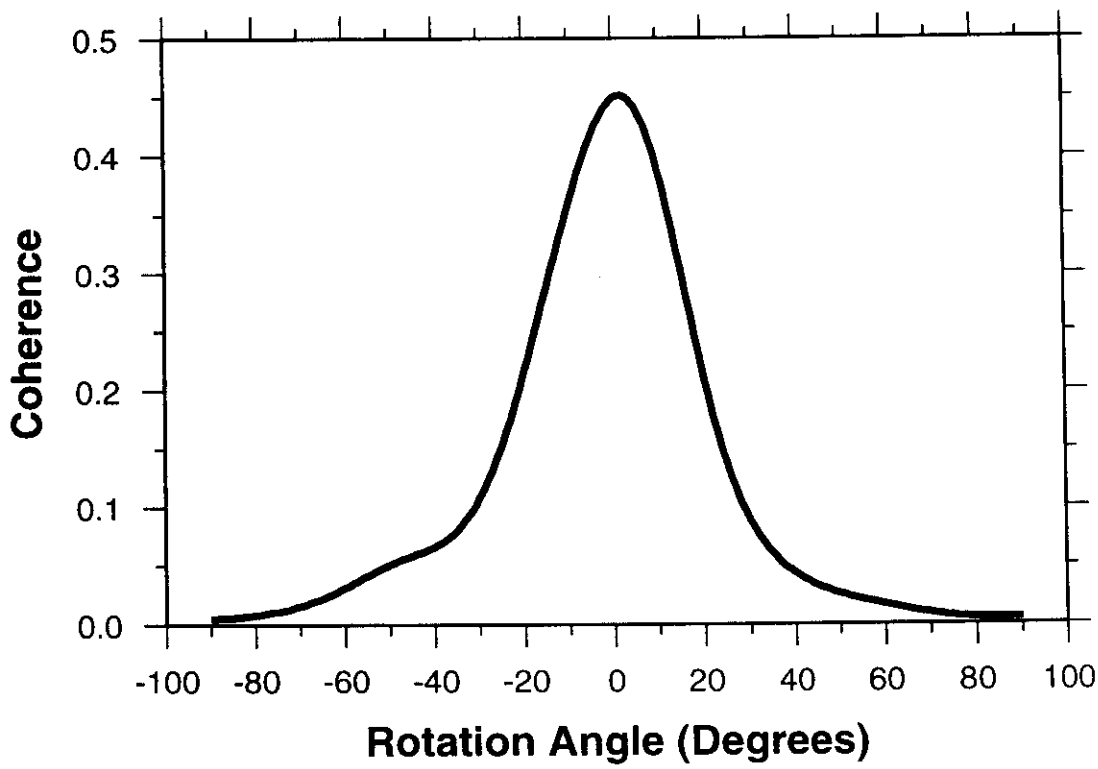

Figure 3.9: Coherence as defined by Griot *et al.* (1998) between the two 2υ anisotropy maps shown in Figure 3.8.

7. Continental Scale Tomography: the Arctic

Summary

We present the results of a study of surface wave dispersion across the Arctic region (> 60°N) and compare the estimating group velocity maps with new maps of the body wave phases P_n and S_n. Data recorded at about 250 broadband digital stations from several global and regional networks were used to obtain Rayleigh and Love wave group velocity measurements following more than 1100 events with magnitudes $M_s > 5.0$ that occurred in the Northern hemisphere from 1977 to 1998. These measurements were used to construct both isotropic and 2Ψ azimuthally anisotropic group velocity maps from 15 s to 200 s period. As elsewhere in the world, the observed maps display the signatures of sedimentary and oceanic basins, crustal thickness variations, and upper mantle anomalies under both continents and oceans. We also present P_n and S_n maps produced from a groomed data set of travel times from the ISC and NEIC bulletins. The long period group velocity maps correlate well with P_n and S_n velocities. Finally, at long wavelengths the estimated 2Ψ azimuthal anisotropy in Rayleigh wave group velocity correlates well with the azimuthal anisotropy in phase velocity obtained in a global scale study of Trampert and Woodhouse. Because attempts to improve the resolution to regional scales change both the amplitude and the pattern of the inferred azimuthal anisotropy, caution should be exercised in interpreting the anisotropy maps.

7.1 Introduction

There have been significant recent advances in a number of Arctic solid earth geophysical disciplines using a variety of observing platforms (ocean subsurface, ocean surface, airborne, satellite) and methodologies (e.g., sea floor topography, gravity and magnetic anomalies, marine drilling, improved coverage of seismic refraction and multi-channel reflection surveys in both oceanic and continental areas). (Johnson and Brass, 1998 provide a recent review of a subset of these developments). Nevertheless, as a whole, the Arctic solid earth remains among the most poorly characterized and understood regions of the Earth. In particular, it is probably fair to say that large-scale natural-source seismology has provided little insight into the structure or tectonic history of the Arctic. By the 'Arctic' we refer to regions above about 60° N latitude, including both the oceanic and the continental regions, and tacitly mean the crust and uppermost mantle. Some of the principal physiographic features of this region are shown in Figure 7.1.

The historical shortage of seismic stations and the inhomogeneous distribution of earthquakes in high northern latitudes has limited the ability of large-scale natural-source seismology to reveal significant information about the Arctic solid earth. Body wave receiver functions and shear wave

splitting studies would provide valuable information near the few seismic stations that have existed across the Arctic historically, and, as shown later, coverage produced by the uppermost mantle turning phases P_n and S_n is somewhat patchy. Because of the station and earthquake distribution at high northern latitudes, the structure of the Arctic crust and uppermost mantle is best explored with surface waves. Until recently, however, constraints on the Arctic solid earth have come largely from global scale studies which have not been designed to provide optimal coverage or resolution in high latitude regions (e.g., Montagner and Tanimoto, 1991; Trampert and Woodhouse, 1995; Ekström et al., 1997; Masters et al., 1996; Van der Hilst et al., 1997; Bijwaard et al., 1998). In addition, surface wave studies dedicated to the Arctic were completed before the installation of the large number of stations at high northern latitudes that occurred during the 1990s. For example, in the study of Zeng et al. (1989) fewer than 100 surface wave paths were available. Other surface wave studies that took place in the late 1970s and 1980s were also severely limited in number of available paths and concentrated on a few widely separated regions: e.g., the Barents Sea shelf (Calcagnille and Panza, 1978; Levshin and Berteussen, 1979; Kijko and Mitchell, 1983; Chan and Mitchell, 1985, 1986; Egorkin et al., 1988); the Laptev Sea shelf (Lander et al., 1985; Lander, 1989), and Northern Canada (Chan and Mitchell, 1986.)

Therefore, seismic models at high northern latitudes continue to display poorer resolution than elsewhere on the globe. Our goal is to begin to address this situation by providing reliable information for building a significantly improved seismic model of the Arctic crust and uppermost mantle. The information reported here includes new Rayleigh and Love wave group velocity maps and maps of the regional body wave phases P_n and S_n. These maps provide information similar to that produced by Arctic satellite gravity (e.g., Sobczak et al., 1990) and magnetic maps (e.g., Coles and Taylor, 1990), although at a higher resolution, by providing a large-scale context in which to place smaller scale studies.

This paper summarizes the current state of the continually improving maps of surface wave dispersion, P_n, and S_n across the Arctic. Although still emerging, the current results demonstrate much better spatial resolution than preceding seismological studies of the area. The observed maps clearly display the signatures of sedimentary and oceanic basins, crustal thickness variations, and upper mantle anomalies under both continents and oceans. This study is on-going, and future efforts will improve data coverage significantly. The construction of a 3-D shear velocity model of the crust and uppermost mantle is a natural use of the data presented here.

7.2 Data Selection and Processing

To estimate Rayleigh and Love wave group velocities, we used data obtained from about 250 broadband digital stations from a number of global and regional networks, including GSN, GEOSCOPE, USNSN, GEOPHONE, CNSN, MEDNET, KNET, and KAZNET. Data from PASSCAL deployments in Saudi Arabia and Tibet were also used. Seismograms following about 1100 earthquakes with magnitude $M_s \geq 5.0$ that occurred in the Northern hemisphere from 1977 to 1998 were selected for processing. Station and earthquake locations are shown in Figure 7.2. These data were processed using the frequency-time analysis method described in detail by Levshin et al. (1992) and Ritzwoller and Levshin (1998).

The measurements used to estimate group velocity maps are chosen rather carefully in an iterative multi-part process. First, at each period and wave type, group travel times are computed using a smoothed global map obtained from the hybrid model composed of the crustal model

CRUST5.1 of Mooney *et al.* (1998) and the mantle model S16B30 of Masters *et al.* (1996). Measurements that fit the predictions from this model better than three times the overall rms misfit are retained. Second, these measurements are clustered into summary rays that sample nearly identical 'unique' paths. Third, we use these clustered measurements to estimate very smooth group velocity maps. Finally, the process is restarted from the beginning with the initial data set, measurements are rejected with the estimated smooth maps, and the remaining measurements are reclustered. The resulting data set is what we use to estimate the group velocity maps discussed in the following sections.

The number of unique paths depends on period and wave type. Path numbers maximize near 40 s period and decrease at both shorter and longer periods. Thus, there are about 11000 unique Rayleigh wave paths at 40 s period across the region of study, but only about 1500 at 15 s and 6000 at 150 s period. The corresponding numbers for Love waves are 7500, 900 and 6000. Path densities at different periods for both Rayleigh and Love waves are shown in Figures 7.3 and 7.4. For Rayleigh waves, path densities are high across most of the region North of the 60° N latitude, but are higher in the Eastern hemisphere due to the large number of measurements we obtained as part of an on-going study of Eurasia (e.g., Ritzwoller and Levshin, 1998). Path densities for Love waves are generally lower than for Rayleigh waves, particularly in North America, again due to the priorities of previous studies.

The procedure for estimating P_n and S_n maps follows that described by Ritzwoller *et al.* (2000). P_n and S_n travel times are taken from a groomed version of the ISC and NEIC data bases described, in part, by Engdahl et al. (1998). ISC travel times are for events that occurred from 1964 through 1997 and NEIC data are from 1998 and 1999. The locations of the events are replaced with local ground truth locations whenever possible (e.g., Sultanov et al., 1999). We define the phases P_n and S_n as arriving between epicentral distances of 3° and 15°. Truncation of the data set to include rays only for shorter maximum epicentral distances (e.g., Hearn and Ni, 1994), severely restricts path coverage in the Arctic.

Data are selected for analysis if the residual relative to the prediction from the spherical model ak135 (Kennett et al., 1995) is less than 7.5 s for P and 15 s for S, if the event depth is within the crust or less than 50 km deep, if the azimuthal gap to all reporting stations for the event is less than 180°, and if the nominal error ellipse is less than 1000 km^2 in area. In order to reject late arriving phases (e.g., PmP, P_b, SmS, S_b) misidentified as P_n or S_n we apply a stricter misfit threshold between epicentral distances from $3° - 7°$. Altogether, about 1,132,500 P_n travel times and 310,800 S_n travel times are left for tomographic inversion across the Arctic (latitudes higher than 50° N). Path densities are shown in Figure 7.5.

7.3 Tomographic Method

The group velocity maps and the P_n and S_n maps are defined over a two-dimensional surface (latitude θ, longitude ϕ). Thus, they may be estimated with the same tomographic method. We use the method of Barmin et al. (2000). In this method, the model is constructed on an equally spaced grid such that the following figure-of-merit is minimized:

$$(\mathbf{Gm} - \mathbf{d})^T \mathbf{C}^{-1} (\mathbf{Gm} - \mathbf{d}) + \sum_{k=0}^{n} \alpha_k^2 ||F_k(\mathbf{m})||^2 + \sum_{k=0}^{n} \beta_k^2 ||H_k(\mathbf{m})||^2, \tag{7.1}$$

which is a linear combination of data misfit, model roughness, and the amplitude of the perturbation to a reference model. The vector $\mathbf{m}$ represents the estimated model over the region of interest, i.e. values of velocity perturbations relative to the reference model at grid points. $\mathbf{G}$ is the forward operator that computes travel time from the estimated model, $\mathbf{d}$ is the data vector which components are observed travel time residuals relative to the reference model, $\mathbf{C}$ is the data covariance matrix or matrix of data weights, F is a Gaussian smoothing operator, and H is an operator that penalizes the norm of the model in regions of poor path coverage for the isotropic component of the model or poor azimuthal coverage for the anisotropic model coefficients. The model $\mathbf{m}$ is azimuthally anisotropic such that m_0 is an isotropic perturbation to the reference model and $m_1, \ldots, m_4$ represent azimuthally anisotropic perturbations (Smith and Dahlen, 1973; Trampert and Woodhouse, 1996):

$$m(\mathbf{r}, \Psi) = m_0(\mathbf{r}) + m_1(\mathbf{r}) \cos 2\Psi + m_2(\mathbf{r}) \sin 2\Psi + m_3(\mathbf{r}) \cos 4\Psi + m_4(\mathbf{r}) \sin 4\Psi, \tag{7.2}$$

where $\mathbf{r} = (\theta, \phi)$, and Ψ is the azimuth of the wave path at point $\mathbf{r}$. The spatial smoothing operator is defined over the 2-D model as follows

$$F_k(\mathbf{m}) = m_k(\mathbf{r}) - \int_S S_k(\mathbf{r}, \mathbf{r}') m_k(\mathbf{r}') d\mathbf{r}' \,, \tag{7.3}$$

where S_k is a smoothing kernel:

$$S_k(\mathbf{r}, \mathbf{r}') = K_{0k} \exp\left(-\frac{|\mathbf{r} - \mathbf{r}'|^2}{2\sigma_k^2} \right) \tag{7.4}$$

$$\int_S S_k(\mathbf{r}, \mathbf{r}') d\mathbf{r}' = 1, \tag{7.5}$$

and σ_k is the spatial smoothing width or correlation length.

The final term in the penalty function penalizes the weighted norm of the model,

$$H_k(\mathbf{m}) = \mathcal{H}(\rho(\mathbf{r}), \chi(\mathbf{r})) m_k. \tag{7.6}$$

where $\mathcal{H}$ is a weighting function that depends on local path density ρ for isotropic structure and a measure of local azimuthal distribution χ for azimuthal anisotropy. Thus, for $k = 0$, $\mathcal{H} = \mathcal{H}(\rho)$ and for $k = 1, \ldots, 4$, $\mathcal{H} = \mathcal{H}(\chi)$. Path density is defined as the number of paths intersecting a circle of fixed radius with center at the point $\mathbf{r}$. For isotropic structure, we choose $\mathcal{H}$ to approach zero where path density is suitably high and unity in areas of poor path coverage. The function $\mathcal{H}(\rho)$ can be chosen in various ways. We use $\mathcal{H} = \exp(-\lambda\rho)$, where λ is a user defined constant. To damp azimuthal anisotropy in regions with poor azimuthal coverage, we define $\chi(\theta, \phi)$ to measure the azimuthal distribution of ray paths at point (θ, ϕ). To find χ we construct a histogram of azimuthal distribution of ray paths in the vicinity of (θ, ϕ) for a fixed number n of azimuthal bins in the interval between 0° and 180°, and evaluate the function

$$\chi = \frac{\sum_{i=1}^{n} f_i}{n \max_i f_i}, \tag{7.7}$$

where f_i is the density of azimuths in the ith bin. Values of χ are in the range $1/n \leq \chi \leq 1$. $\chi \approx 1$ characterizes an almost uniform distribution of azimuths, and $\chi \approx 1/n$ is an indicator of the

predominance of a single azimuthal direction (large azimuthal gap). We assume that the anisotropic coefficients cannot be determined reliably in regions where χ is less than ~ 0.3.

The minimization of the expression in equation (7.1) explicitly ensures that the estimated model approximates a smoothed version of the model.

The inversion for P_n and S_n is described in detail by Ritzwoller *et al.* (2000). The observed P_n or S_n travel time, t_{obs}, is modeled as follows:

$$t_{obs} = t_m + t_{crust\_sta} + t_{crust\_evt} + \delta t_{sta} + \delta t_{evt} + \delta t(\Delta) + \delta t_m, \tag{7.8}$$

where t_m is the predicted travel time for rays through the mantle part of the input reference model, the contributions to the travel time due to the crustal part of the reference model on the event and station sides are t_{crust_sta} and t_{crust_evt}, the station and event statics are δt_{sta} and δt_{evt}, $\delta t(\Delta)$ is the distance correction, δt_m is the travel time correction for the mantle part of the path, and Δ is epicentral distance. Thus, t_m, t_{crust_sta}, and t_{crust_evt} are predicted by the reference model and $\delta t_{sta}, \delta t_{evt}, \delta t(\Delta)$, and δt_m are estimated. If v_m is the velocity along path p in the reference model and δv_m is the model perturbation along the same path, then

$$t_m = \int_p \frac{ds}{v_m} \tag{7.9}$$

$$\delta t_m = -\int_p \frac{\delta v_m}{v_m^2} ds. \tag{7.10}$$

We assume that the ray through the perturbed model, $v_m + \delta v_m$, takes the same path as the ray through the reference model. In practice, we estimate the 2-D quantity δv_m from which we compute δt_m for each ray p.

We used CRUST5.1 (Mooney *et al.*, 1998) as the reference model in the crust and for mantle P and S. At each geographical point, CRUST5.1 only has one value of P and one value of S for the mantle, intended to characterize the velocity immediately below Moho. For this reason, we assume that the mantle leg of each path p is essentially horizontal, following directly below Moho. Although this is a common approximation in P_n and S_n tomography, it introduces an error relative to real rays that depends on the depth of penetration of the ray, which itself depends on the vertical gradient of velocity in the mantle. To compensate for this error, we introduce into equation (7.8) a term that is a smooth function of distance, which we call the distance correction, $\delta t(\Delta)$. The correction $\delta t(\Delta)$, therefore, attempts to reduce the mantle velocities distributed in 3-D to a single 2-D datum surface which, by design, lies directly below Moho. The distance correction is shown in Figure 7.6 along with the density of residuals for P_n and S_n travel times relative to the reference model.

The application of the distance correction allows us to fit data over a broader distance range than would be possible without the correction. We find that with this correction the tomographic maps agree well with those produced with short path data alone (epicentral distances less than 10°) in those regions where tomographic maps can be constructed reliably using only the short path data.

We follow Hearn and collaborators (e.g., Hearn and Clayton, 1986; Hearn *et al.*, 1991; Hearn and James, 1994; and elsewhere) and estimate event and station corrections or statics. The station and event statics are designed to compensate for errors in the reference crustal model, errors in the prediction of the location of the mantle piercing points, and errors in event locations and origin

times. A static correction is estimated for a station if there are phase picks from at least 7 events made at that station and an event correction is estimated for all events for which there are at least 20 reporting stations. The asymmetry in this condition is due to the fact that there are more physical phenomena modeled with the event static than with the station static (e.g., mislocation, origin time error). The station and event statics are undamped at present.

There are, therefore, many parameters that need to be set to estimate a 2-D map, including grid spacing, $\alpha_0, \ldots, \alpha_4$, $\sigma_0, \ldots, \sigma_4$, and $\beta_0, \ldots, \beta_4$. In practice, the model norm damping constants are all set to the same value $\beta_k = \beta = 1$, and the anisotropic damping constants and correlation lengths are also equal: $\sigma_{anis} = \sigma_1 = \sigma_2$ and $\alpha_{anis} = \alpha_1 = \alpha_2$. We estimate only the 2Ψ component of azimuthal anisotropy here, so $\alpha_3, \alpha_4, \sigma_3$, and σ_4 are all effectively infinite. The parameters used here are shown in Table 1 where U is group velocity, an x indicates that the structure was not estimated for the specified map, and all units are km.

Table 1. Table of inversion parameters. All units are km.

wave-type	σ_0	σ_{anis}	α_0	α_{anis}	*isotropic grid spacing*	*anisotropic grid spacing*
U	200	600	1000 if < 100 s 1300 if ≥ 100 s	1500, 3000, 5000	200	250
P_n	100	x	600	x	100	x
S_n	100	x	600	x	100	x

7.4 Isotropic Group velocity, P_n, and S_n Tomography

The estimated maps are perturbations to the predictions from a reference model. For group velocities, the reference model is ina smoothed version of a hybrid model composed of CRUST5.1 in the crust and S16B30 in the mantle. For P_n and S_n, the reference model is CRUST5.1. As Barmin et al. (2000) show, estimates of spatial resolution and amplitude bias are obtained as by-products of the inversion. We do not discuss these estimates here, but merely state some of the results of the resolution analysis.

As discussed by Ritzwoller and Levshin (1998), the principal source of error in the estimated group velocity maps is expected to be caused by errors in the theory that underlies the tomography rather than errors in the data themselves. Measurement errors are fairly well reduced by the data cleaning procedure discussed in section 2. Ritzwoller and Levshin (1998) discussed four theoretical errors that may potentially affect the results of a tomographic study. Our recent improvements in the tomographic algorithm have effectively eliminated two of these problems: geometrical distortions due to earth flattening approximations and the bias of isotropic structures caused by azimuthal anisotropy. The first has been eliminated by formulating the inversion in spherical coordinates from the outset. The second has been greatly attenuated by simultaneously estimating azimuthal anisotropy with isotropic velocities. The remaining two problems are the mislocation of seismic events and deviation of surface waves from great circle paths. The effects of event mislocation are shown by Ritzwoller and Levshin (1998) to only be important at the periphery of a studied region because data from paths crossing the region containing mislocated events constrain the errors caused by the mislocations. Thus, the major remaining theoretical error that may be of sufficient magnitude to bias the estimated maps is the deviation of surface waves from great circle paths. An evaluation of the bias caused by this effect and attempts to reduce it are the subject of current research. The effect is expected to be most significant at short and intermediate periods

(<50 s) where lateral heterogeneities in the phase velocities are strongest. It will manifest itself as a smearing of the maps in regions of strong heterogeneity that will result in a reduced effective resolution precisely in the most interesting regions.

We estimated group velocity maps for Rayleigh waves at periods from 15 s to 200 s and for Love waves from 20 s - 125 s. A selection of these maps is shown in Figures 7.7 (Rayleigh waves) and 7.8 (Love waves). The spatial resolution changes geographically and with period, but in general is reasonably good; 300 - 500 km between 20 s and 150 s for Rayleigh waves, but worse everywhere for Love waves particularly at very short and very long periods.

The estimated P_n and S_n maps are shown in Figure 7.9. As discussed above, our tomographic method penalizes the amplitude of the maps in regions of poor data coverage. Because the estimated maps are perturbations to a reference state, the maps will revert to the reference model where data coverage is poor; i.e., less than 15 - 20 paths for each 2° × 2° cell. Except for the shortest period Love waves, the vast majority of the group velocity maps shown in Figures 7.7 and 7.8 display sufficient coverage to guarantee that they will be independent of the reference model. This is not true for the P_n and S_n maps because, by definition, these phases only exist to an epicentral distance of 15°. There are large regions of the Arctic in which either earthquakes do not regularly occur or there have been few historical seismic stations that reported phase picks to the ISC. As a result, we identify areas of poor data coverage in Figure 7.9 as grey-shaded regions. The S_n map in particular is very patchy, but we show it for comparison with P_n map in regions where there is sufficient data coverage. The spatial resolution of the P_n map is about 250 - 350 km in Northern Europe, the North Atlantic, and along the Arctic Ocean coasts in the Bering Sea, off Alaska and Western Canada. It is between 400 and 450 km along the Arctic Mid-Oceanic Ridge. Other regions, such as North-Western Siberia or the Amerasia Basin, possess path densities below about 20 paths per 2° × 2° cell and are very poorly resolved.

Misfit statistics for the isotropic maps are presented in Table 2. RMS misfit is presented relative to the two reference models.

Table 2. Misfits between observed and predicted values of group velocities/travel times before and after inversion

wave-type	Reference model $\overline{\delta U}$ (km/s)†	After inversion $\overline{\delta U}$ (km/s)	Variance reduction %
Rayleigh 20 s Group	0.128	0.089	51
Rayleigh 40 s Group	0.133	0.067	75
Rayleigh 100 s Group	0.076	0.049	58
Rayleigh 150 s Group	0.067	0.058	25
Rayleigh 20 s Group	0.209	0.154	46
Rayleigh 40 s Group	0.109	0.077	50
Rayleigh 100 s Group	0.086	0.054	61
Rayleigh 1500 s Group	0.122	0.086	25
	$\overline{\delta t}$ (s)††	$\overline{\delta t}$ (s)	%
P_n	2.48	1.43	67
S_n	3.34	2.60	39

† - CRUST5.1 + S16B30
†† - CRUST5.1

7.5 Azimuthal anisotropy

Simultaneous with the isotropic maps we have estimated 2Ψ anisotropic maps for group velocity following the procedure described by Barmin et al. (2000). This procedure allows us to apply different relative damping parameters, α_0 and α_{anis}, to the isotropic and anisotropic terms of the estimated model. The larger the values of the damping parameters, the smoother will be the resulting maps.

As shown in Figure 7.10, strong damping of anisotropy produces a very long wavelength pattern of azimuthal anisotropy in group velocity similar to the pattern obtained in the global scale phase velocity study of Trampert and Woodhouse (1996). In this figure, our 50 s and 100 s group velocity maps are compared with the global scale 40 s and 80 s phase velocity maps. The differences in the period between the group and phase velocity maps is designed to compensate partially for the fact that phase velocities sample deeper than group velocities at a particular period.

To quantify the correlation between two maps of azimuthal anisotropy, we use the coherence function defined by Griot et al. (1998) which takes into account differences in the directions of the fast axes ($\psi_1(\theta,\phi)$, $\psi_2(\theta,\phi)$) and the amplitudes ($A_1(\theta,\phi)$, $A_2(\theta,\phi)$; $A = (U_1^2 + U_2^2)^{1/2}$) of the two maps. The coherence K as a function of rotation angle ψ, varying between $-90°$ and $90°$, is defined as follows:

$$K(\psi) = \frac{\sum_{\theta}\sum_{\phi} A_1(\theta,\phi)\, A_2(\theta,\phi)\, \sin\,\theta\, \exp\left(-\dfrac{(\psi_1(\theta,\phi) - \psi_2(\theta,\phi) + \psi)^2}{2D_{cor}^2}\right)}{\left(\sum_{\theta}\sum_{\phi} \sin\,\theta\, A_1^2(\theta,\phi)\right)^{1/2} \left(\sum_{\theta}\sum_{\phi} \sin\,\theta\, A_2^2(\theta,\phi)\right)^{1/2}}. \tag{7.11}$$

Here D_{cor} is the uncertainty in the anisotropic direction, and was set to equal 10°. The coherence between the group velocity and the phase velocity maps shown in Figure 7.10 is displayed as the solid lines in Figures 7.11a and 7.11b. If the correlation between the group and phase velocity maps were perfect, the coherence functions would peak with unit amplitude at a differential angle of 0° and would display no side-lobes. For the comparison between the 100 s group velocity and the 80 s phase velocity (Figure 7.10b), the coherence function peaks at about -4° with an amplitude of 0.35 and a side-lobe centered at about ±90°. This represents substantial similarity between the two maps.

Although the long wavelength part of the estimated group velocity maps is in substantial agreement with the global study of Trampert and Woodhouse, the information content in these maps is low. We would like to reduce the scale of the estimated variations in azimuthal anisotropy in a stable, continuous way in the attempt to reveal more information about the variations in the fabric and mineral orientation of the uppermost mantle. To do so, the damping of azimuthal anisotropy must be reduced which will make the estimates more sensitive to noise, both signal generated and other.

The anisotropic damping parameter for the group velocity maps shown in Figure 7.10 is $\alpha_{anis} = 5000$. When we reduce α_{anis} from 5000 to 3000 and then to 1500 the correlation with the global model degrades dramatically, as the dashed and dotted lines in Figures 7.11 a and 7.11b demonstrate. The coherence between our estimated maps also changes strongly as the damping parameters are reduced as shown in Figures 7.11c and 7.11d. Thus, both the pattern and amplitude of anisotropy are affected by the choice of the strength of damping. However, isotropic maps do not

change significantly with changes of α_{anis}. As a rule they. became slightly more smooth as α_{anis} decreases. Overall rms misfit statistics for the isotropic model. the isotropic model with smooth azimuthal anisotropy. and the isotropic model with smaller scale azimuthal anisotropy are presented in Table 3. Typically, rms misfit reductions are much easier to achieve by reducing the damping of the isotropic model than by introducing azimuthal anisotropy.

The resulting Rayleigh wave group velocity maps at 50 s and 100 s period for moderate damping ($\alpha_{anis} = 1500$) are shown in Figure 7.12. In these maps, in contrast with those in Figure 7.10, the largest anomalies are associated with the Baltic, Siberian and Canadian shields and the fast directions in the Arctic Ocean are nearly perpendicular to those in the highly damped maps in Figure 7.10. In addition, the fast directions are predominantly perpendicular to plate boundaries along the Atlantic MOR (Mid-Oceanic Ridge) and in the Bering Sea along the Aleutian Arc, but are almost parallel to the Arctic MOR. This may be due to mineral orientation caused by relatively fast plate motions in the Atlantic and North-Western Pacific and much slower speeds in the Arctic Ocean. Finally, as demonstrated by Figure 7.13, the patterns of anisotropy in the 50 s and 100 s Rayleigh wave maps are exceptionally well correlated, which may indicate the continuity of the pattern of anisotropy at least through 100 - 150 km of the uppermost mantle for a significant part of the studied area (North America, Greenland, the Baltic shield, some parts of the Northern Eurasia).

Although the high correlation between the long wavelength component of our regional scale group velocity maps with the global scale phase velocity maps of Trampert and Woodhouse is encouraging, the strong dependence of the estimated maps on arbitrarily chosen damping parameters should give us pause in attempting to interpret the maps quantitatively.

7.6 Discussion

Isotropic group velocity maps provide strong constraints on the shear velocity of the crust and upper mantle and on crustal thickness across the Arctic. Because group velocity sensitivity kernels are more complicated than phase velocity kernels (e.g., Rodi et al., 1975), interpreting them directly in terms of causative structures is not entirely straightforward. However, our experience with the inverse problem in various regions around the world (e.g., Villaseñor et al., 2000) indicates that the maps at certain periods do identify some of the key elements of the model. For example, low velocity anomalies on the 20 s maps are typically associated with sedimentary basins. Anomalies on the 40 s maps are inversely related to crustal thicknesses in continental areas, so that low velocities typically imply thick continental crust and high velocities imply thin crust. The 40 s map predominantly samples the upper mantle under oceanic areas. At periods of 100 s and above, the maps are preferentially sensitive to the uppermost mantle beneath both continents and oceans. With these observations in mind, it is worth noting the major features on the isotropic group velocity maps and what they may mean.

Nearly all of the major sedimentary basins seen in Figure 7.14 (Laske and Masters, 1997) are associated with low velocities on the 20 s Rayleigh and Love wave group velocity maps. These include sedimentary basins in the Chukchi and Beaufort Seas, the Lincoln Sea north of Greenland, Baffin Bay, the Greenland Sea, the Barents Sea, the Kara Sea, and the E. Siberian Sea. The observation of distinct low velocity anomalies associated with relatively small basins in the Lincoln and Greenland Seas north and east of Greenland, respectively, clearly characterizes the spatial resolution of the group velocity maps. Our studies of Central Asia (Ritzwoller and Levshin (1998);

Ritzwoller et al. (1998)) demonstrated that periods shorter than 20 s will produce even better images of sedimentary basins. Unfortunately, our data set at shorter periods needs to be developed further before we are able to obtain these maps. In continental regions, in particular, age, chemical composition, lithology, and the tectonic history of the sediments also influence group velocities. Some sedimentary basins, e.g., the Enisei-Khatanga trough in Northern Siberia, do not appear as low velocity anomalies on the short period group velocity maps due to partial metamorphism of the sediments and interpenetration of the sediments with trap basalts.

The Amerasia and Eurasia Basins are imaged at 20 s and 40 s period in Figures 7.7 and 7.8. The high velocity anomaly coincident with the Eurasia Basin extends nearly to the continental shelf on the 40 s map all around the Arctic Ocean. The shape of the Amerasia Basin on the 40 s map also appears to be fairly accurately resolved.

We clearly observe continental low velocity anomalies on the 40 s Rayleigh wave map which typically signify regions of thickened crust. Low velocity anomalies are associated with the Verkhoyanski Range, the Chersky Range, Kamchatka, the Koryakia and Okhotsk-Chuckotsk volcanic belts in North-Eastern Siberia, as well as the Brooks Range, the Alaska Range, and Yukon Plateau in Northern America.

Mid-ocean ridges (MOR) appear in Rayleigh wave group velocity maps around the world at periods of 40 s and above. The Arctic MOR, however, does not manifest itself on the 40 s Rayleigh wave map in Figure 7.7. Oceanic low velocity anomalies of mantle origin do not appear in the Arctic until nearer to 100 s period. This is typical of slower spreading ridges. There are, however, two significant Artic low velocity anomalies at long periods. The first and more prominent is associated with the Iceland hotspot and the northward continuation of this anomaly adjacent to the Mohns Ridge toward the Fram Strait between Greenland and Svalbard. The thermal halo of this hot spot in the mantle, manifested as a low velocity anomaly in most of the dispersion maps, is considerably broader than the surface expression of the hot spot. The second anomaly runs from the Laptev Sea to the Mendeleev Ridge. Interestingly, this anomaly is not obviously coincident with the seismically active Arctic MOR. At 150 s period, the low velocities are more nearly coincident with the aseismic Mendeleev Ridge.

There are two very striking features on the long period maps under continents at high latitudes. The first is the expression of the continental shields. The Russian Platform, Siberian Shield, Canadian Shield, and Greenland Shield are imaged clearly on the 100 s and 150 s Rayleigh and Love wave maps in Figures 7.7 and 7.8. The two large Asian shields are separated by a relative low velocity anomaly adjacent to the Urals that becomes more pronounced at longer periods. The second striking feature is the low velocity anomaly that follows the Pacific Rim of Asia from Taiwan to Kamchatka. Figure 7.7 shows that this feature probably extends to the Pacific Rim of North America along the Alaskan and Canadian coasts.

Because the long-period (e.g., 100 s period) Rayleigh and Love wave maps provide information about the uppermost mantle, they should compare favorably with the P_n and S_n velocities seen in Figure 7.9. Comparison is, in fact, very good in regions of good data coverage. The striking similarity of the high velocities of P_n and Rayleigh waves in Northern Greenland is especially noteworthy. Relatively low velocities across Southern Greenland in comparison with velocities across the Canadian shield are in agreement with recent evidence from post-glacial rebound that Southern Greenland has a thinner elastic lithosphere (J. Wahr, personal communication.)

7.7 Conclusions

We have reported the results of a systematic study of surface wave dispersion, P_n, and S_n velocities across the Arctic region. The spatial resolution of the surface wave group velocity maps (300 - 500 km) is significantly higher than the resolution of global maps, particularly at the shorter periods, or maps obtained in previous regional studies. The resulting maps are robust to changes of damping parameters during the tomographic inversion and provide a very satisfactory fit to the observed dispersion curves.

The estimated isotropic group velocity maps clearly display the signatures of sedimentary and oceanic basins, crustal thickness variations, and upper mantle anomalies under both continents and oceans. They provide new constraints on the structure of sedimentary basins, the crust and upper mantle of the Arctic region. Comparison of the long-period group velocity maps with maps of P_n and S_n velocities demonstrates significant similarity in the pattern of the body and surface wave velocity distributions across the region in shield areas, along the tectonic belts of North-Eastern Eurasia and North-Western America, and along the Atlantic and Arctic MORs.

Preliminary maps of azimuthal anisotropy are encouraging in that they provide a consistent pattern of the orientation of fast directions both within our own data set and relative to the study of Trampert and Woodhouse (1996). This is especially true in the oceans. However, both the amplitudes and the patterns of anisotropy depend strongly on damping and further efforts are needed to determine which features of anisotropy are robust.

The next step in interpreting these results is the joint inversion of the observed isotropic group velocity maps with the maps of P_n and S_n and, perhaps, phase velocity.

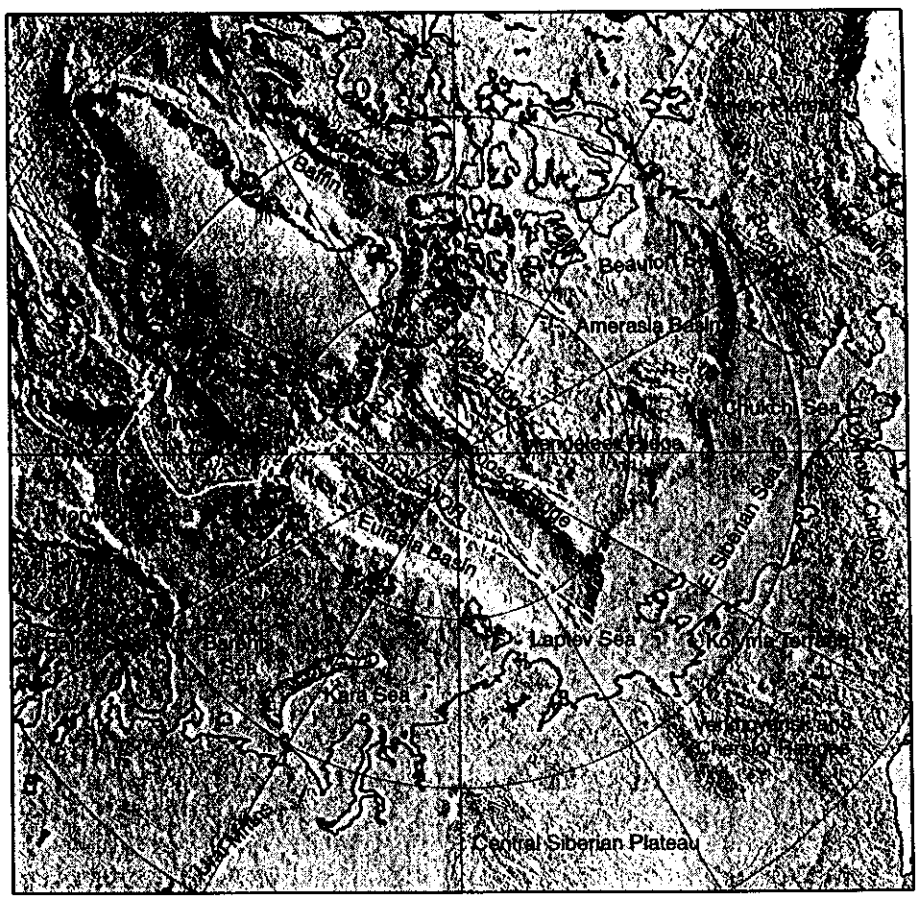

Figure 7.1: Major physiographic features above 60°N latitude.

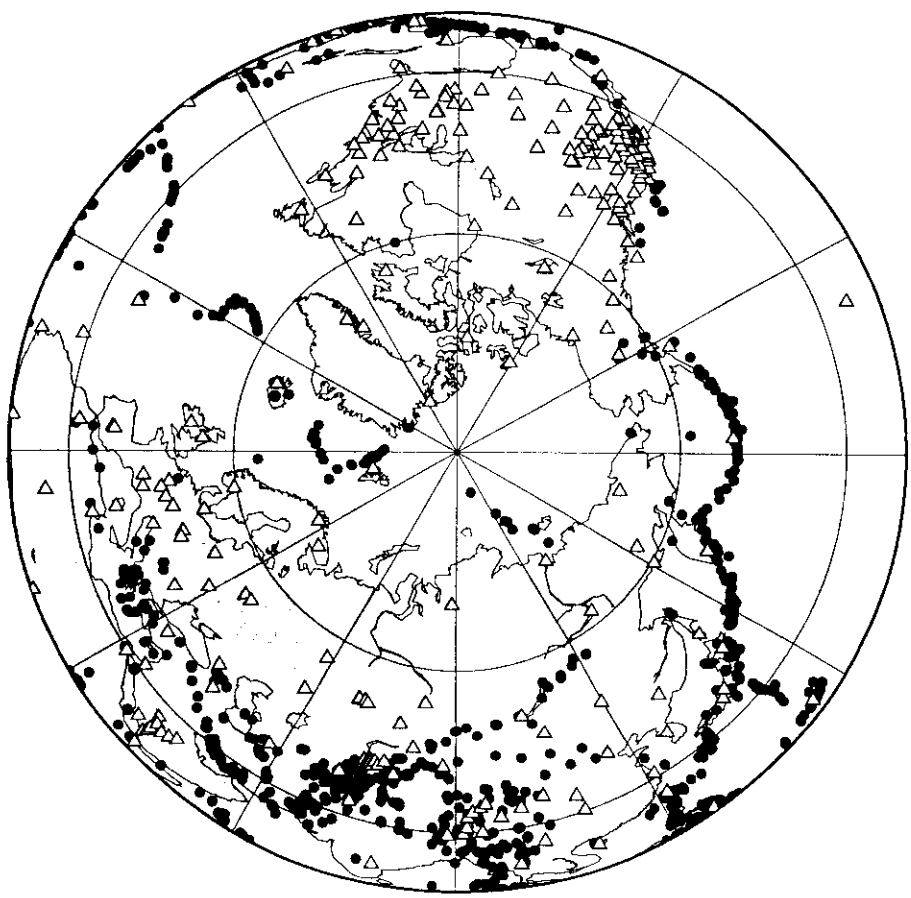

Figure 7.2: Location of the 250 stations (triangles) and 1100 events (dots) used in this study.

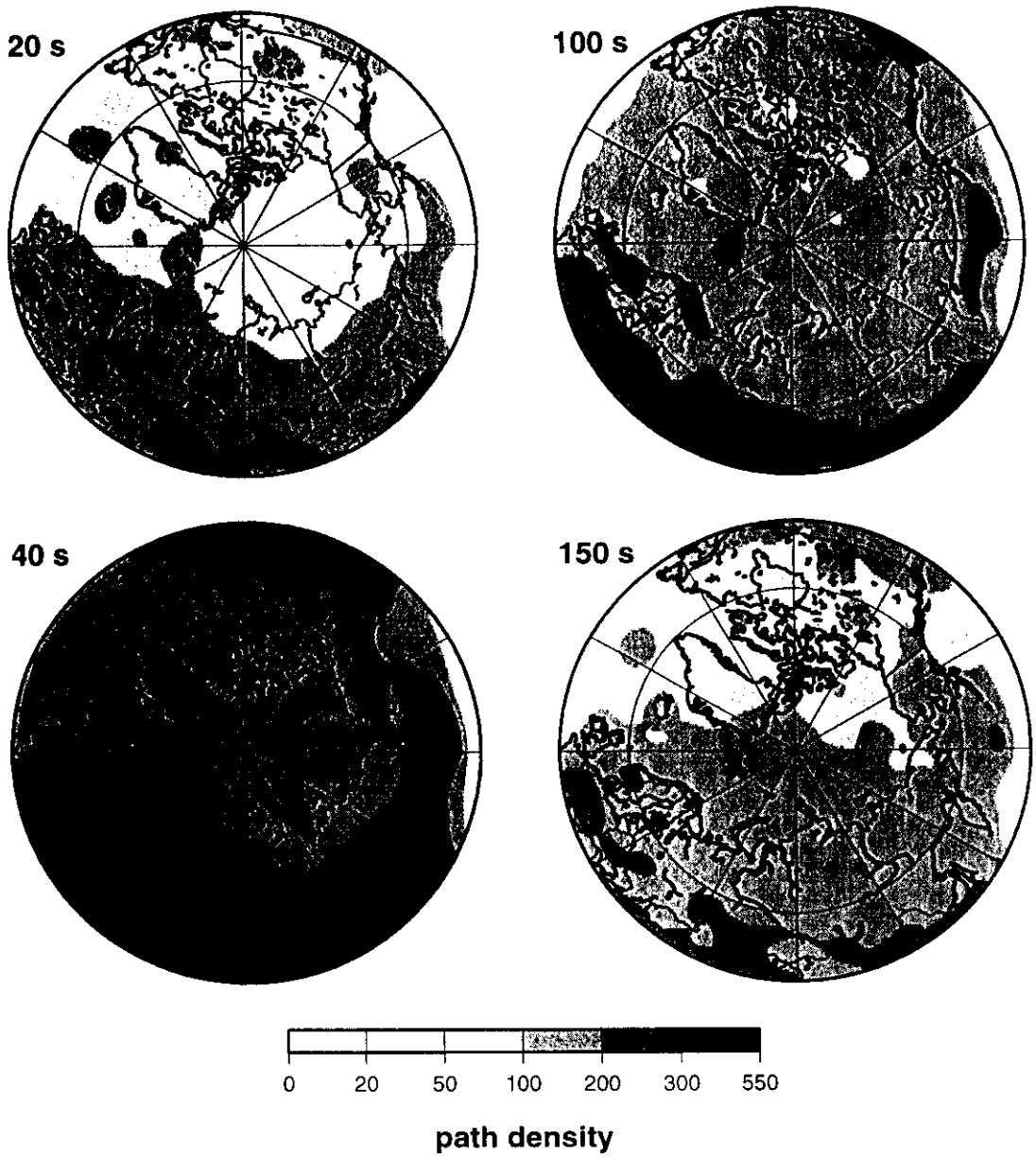

Figure 7.3: Path density for Rayleigh waves at the four indicated periods. Path density is defined as the number of rays intersecting a 2° square cell ($\sim$ 50,000 km^2).

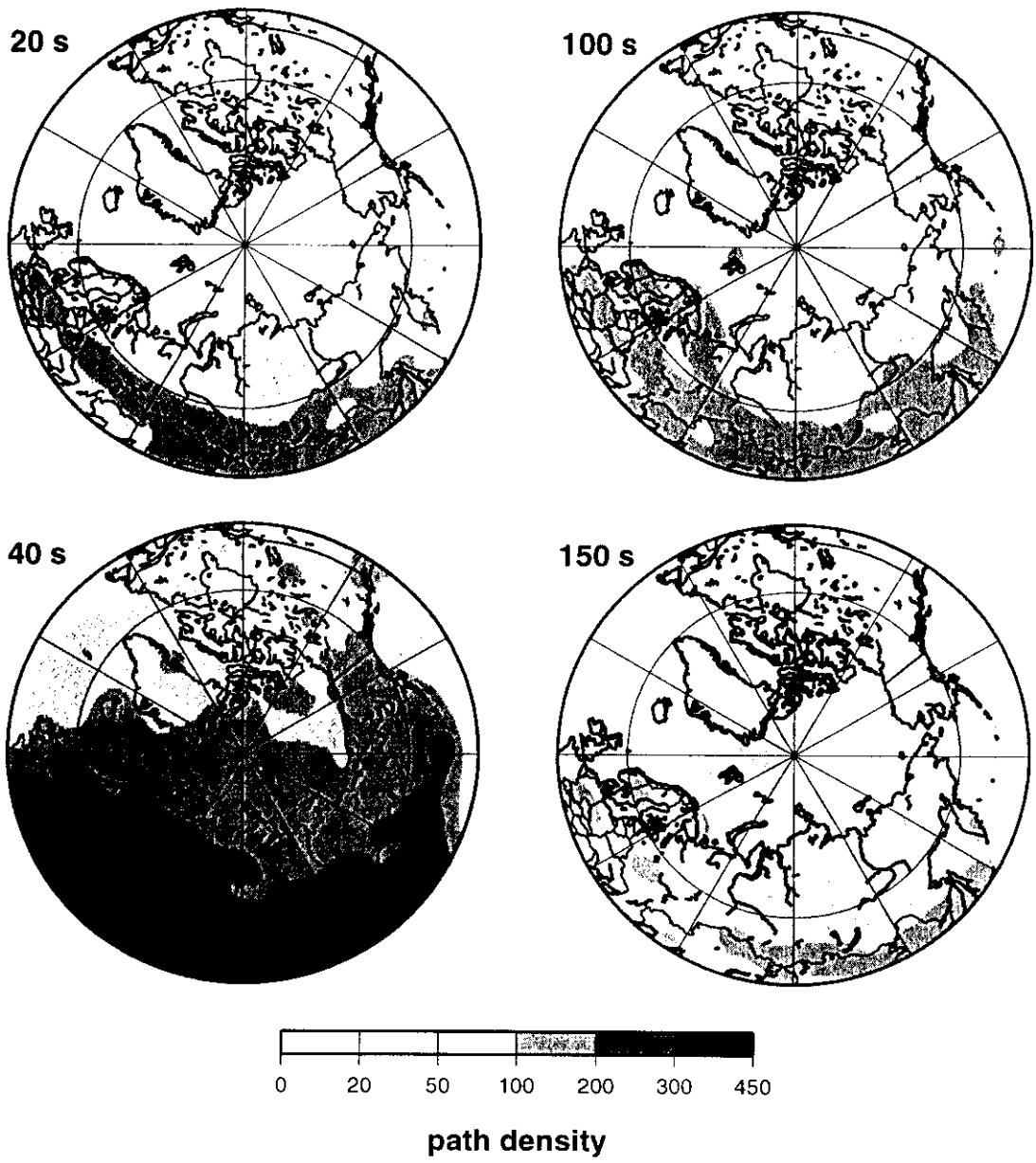

Figure 7.4: Path density for Love waves. See Fig. 7.3 for a definition.

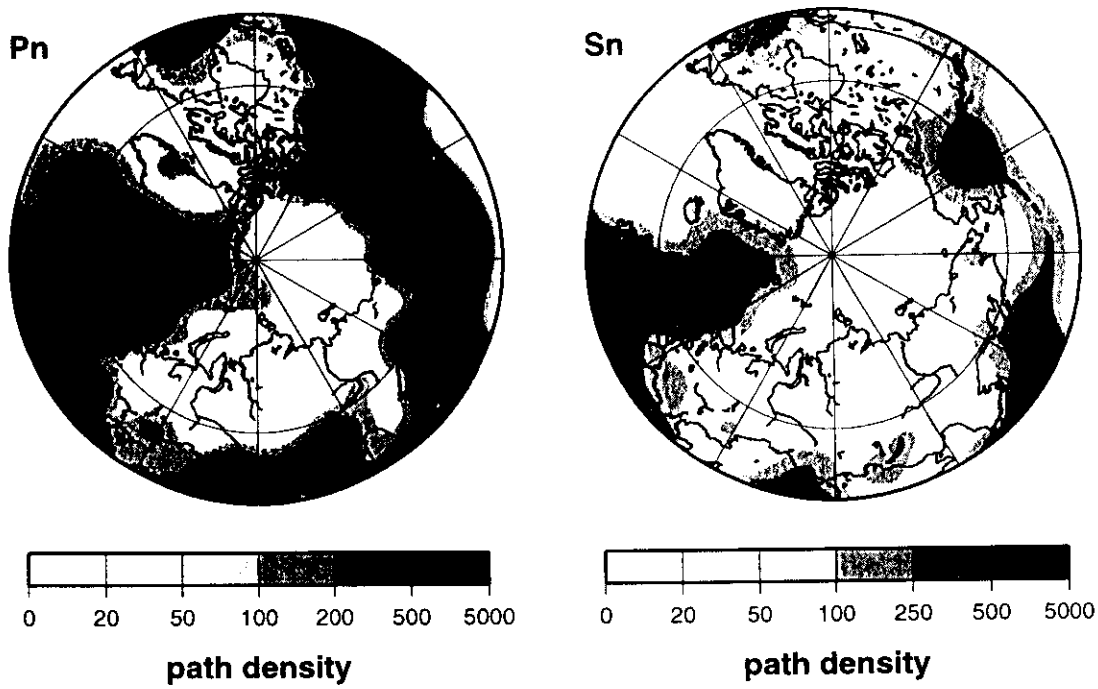

Figure 7.5: Path density for P_n and S_n. See Fig. 7.3 for a definition.

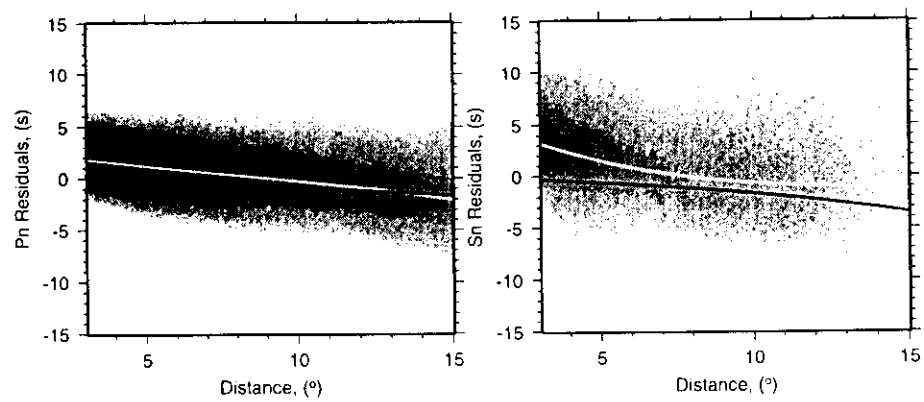

Figure 7.6: Shaded plots of the density of P_n and S_n travel time residuals (observed minus predicted from CRUST5.1) versus epicentral distance with respect to CRUST5.1. White lines are the estimated trends of P_n and S_n travel times versus epicentral distance that are used for the distance corrections, $\delta(\Delta)$. Black lines are similar trends predicted for the model ak135.

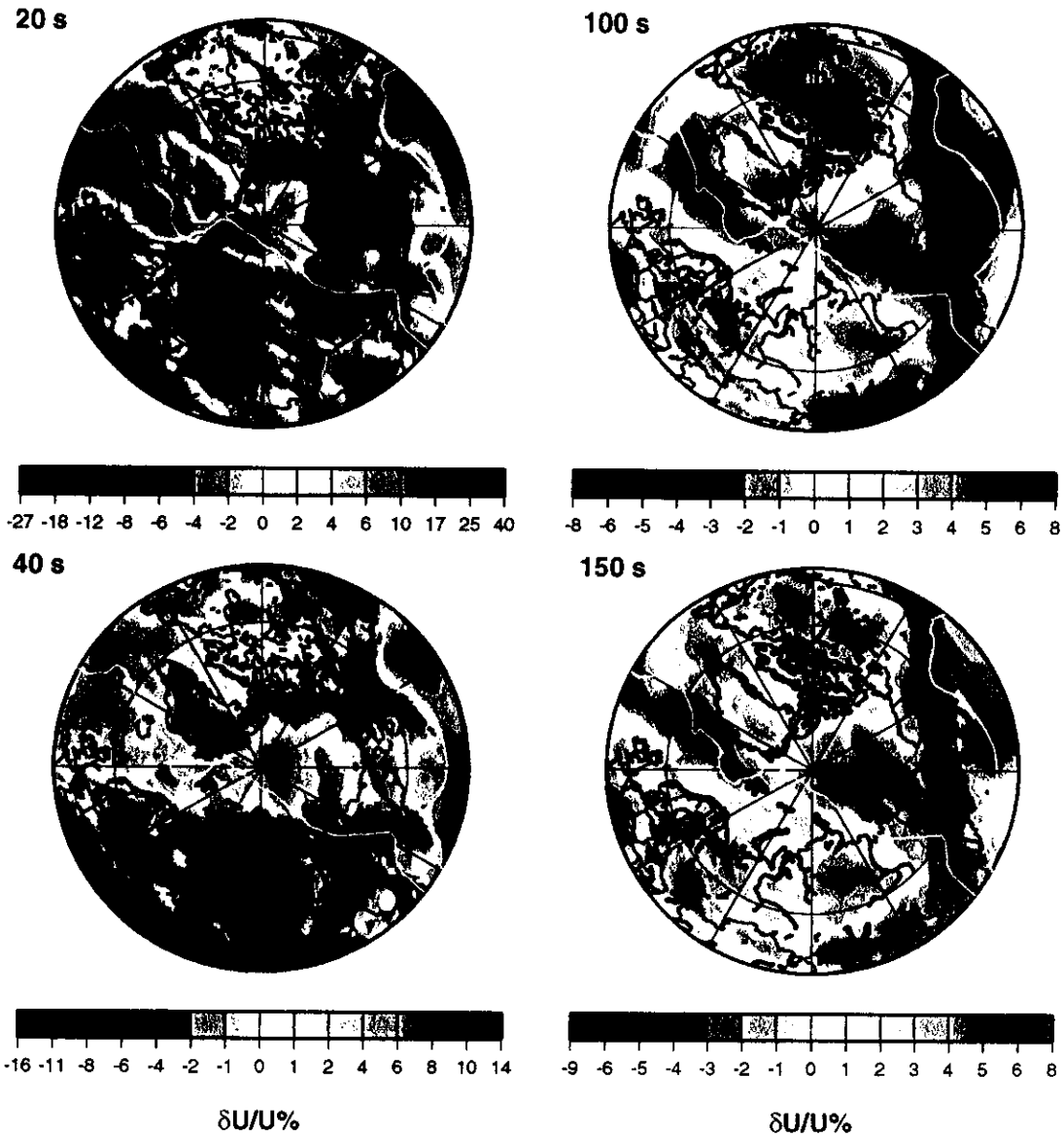

Figure 7.7: Estimated Rayleigh-wave group velocity maps at the indicated periods. $\delta U/U$ is the relative deviation of group velocity from the average value U across the map (in %). White lines are plate boundaries. Reference velocities are as follows:.

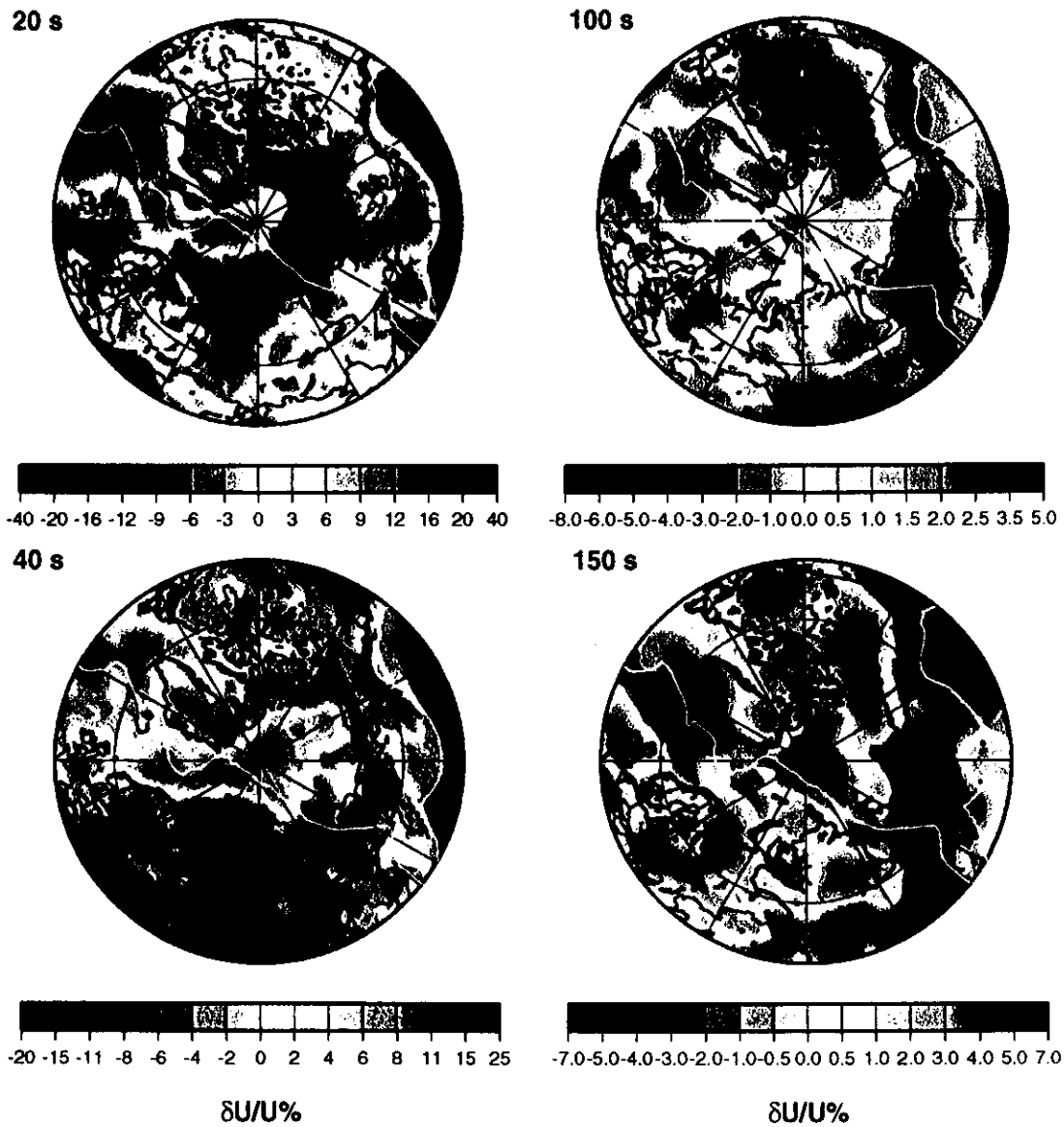

Figure 7.8: Estimated Love-wave group velocity maps at the indicated periods. Reference velocities are as follows:.

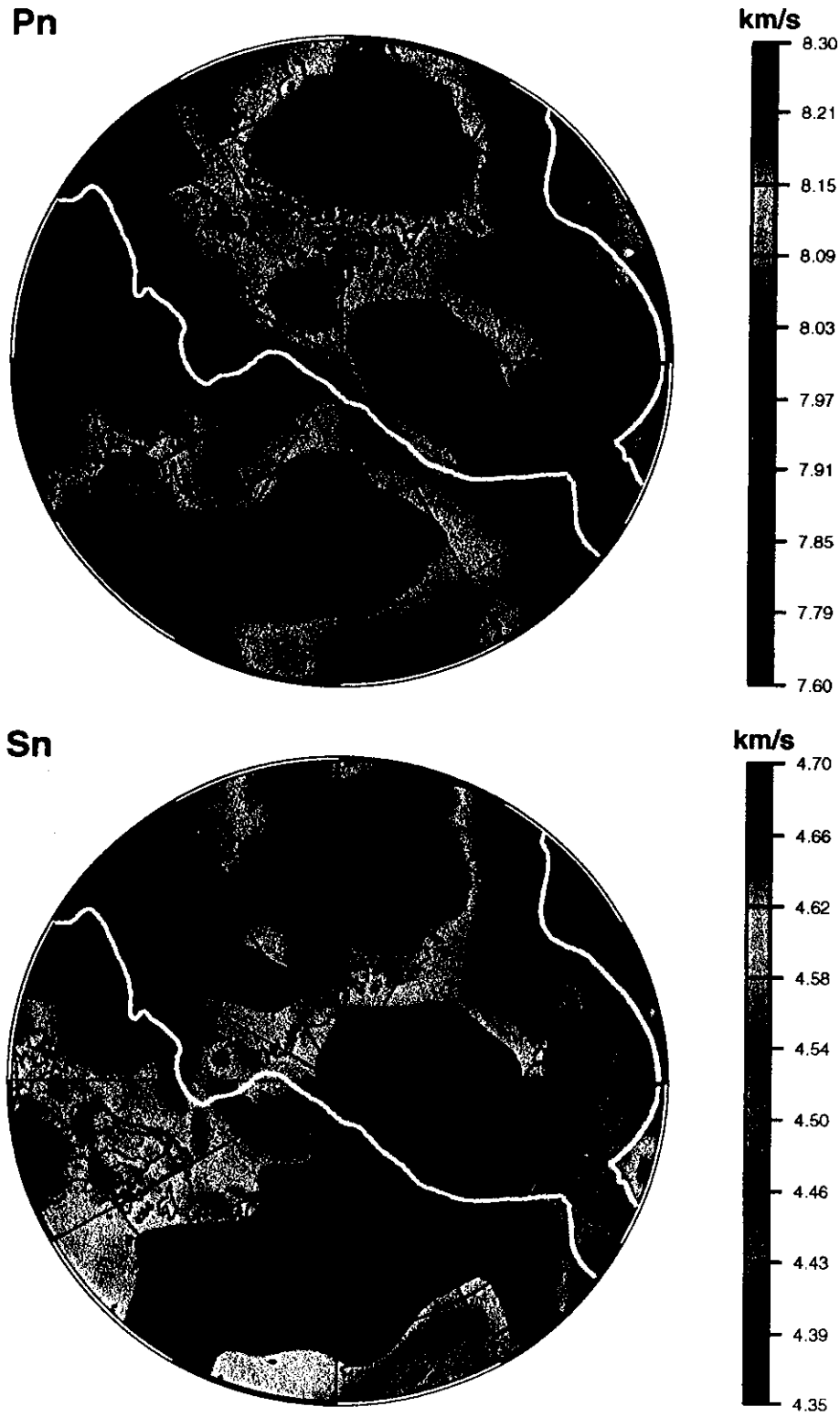

Figure 7.9: P_n and S_n velocities across the Arctic region. Units are km/s. Grey areas have path densities less than 20 paths per a 2° square cell.

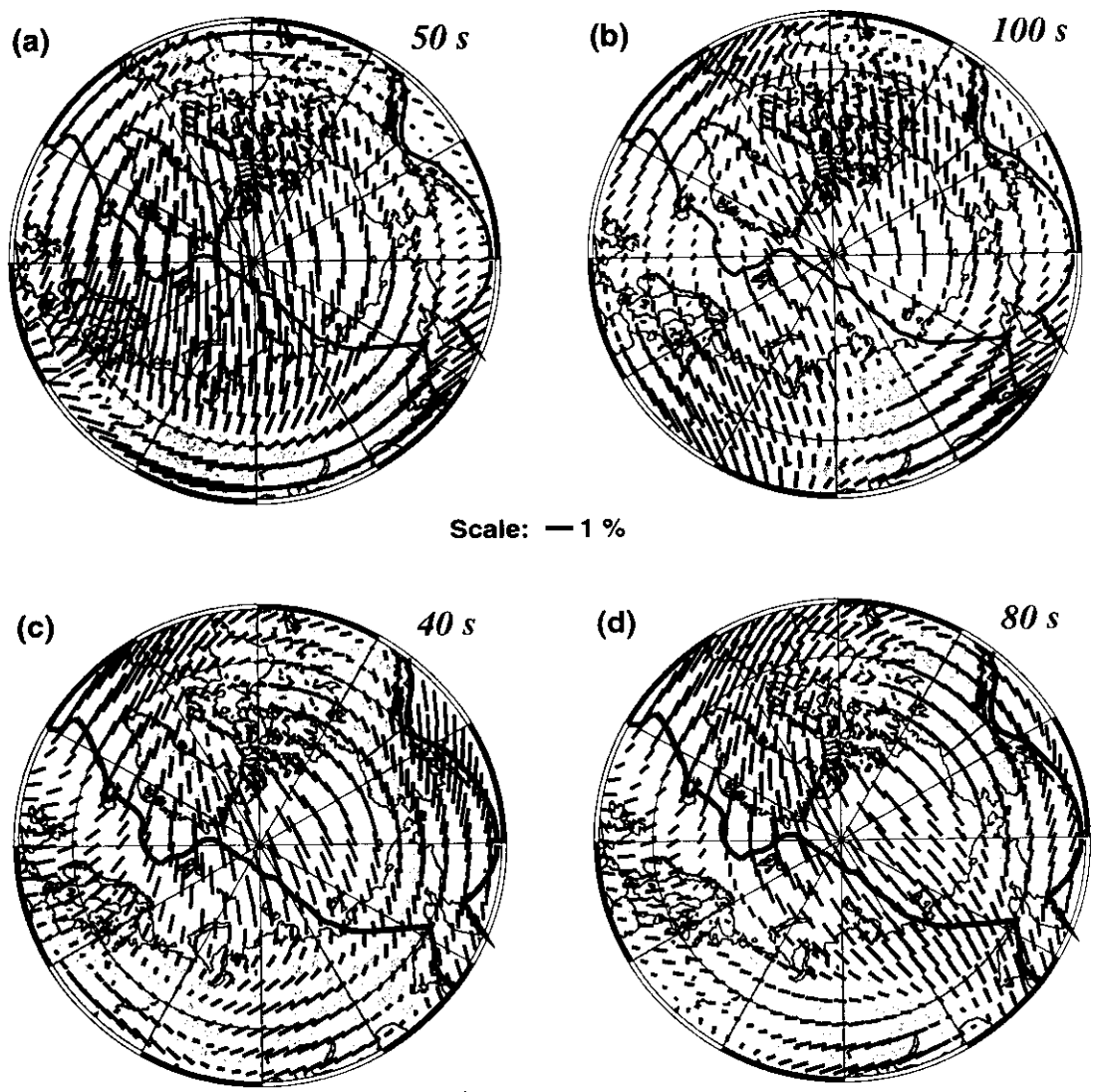

Figure 7.10: The 2Ψ component of azimuthal anisotropy of Rayleigh wave group velocity at the indicated periods. (a, b) Strongly damped group velocity ($\alpha_{anis} = 5000$). (c, d) Phase velocity from Trampert and Woodhouse (1996). The bars indicate the 2Ψ fast directions. The size of the bars is proportional to the ratio of the anisotropic and the isotropic components.

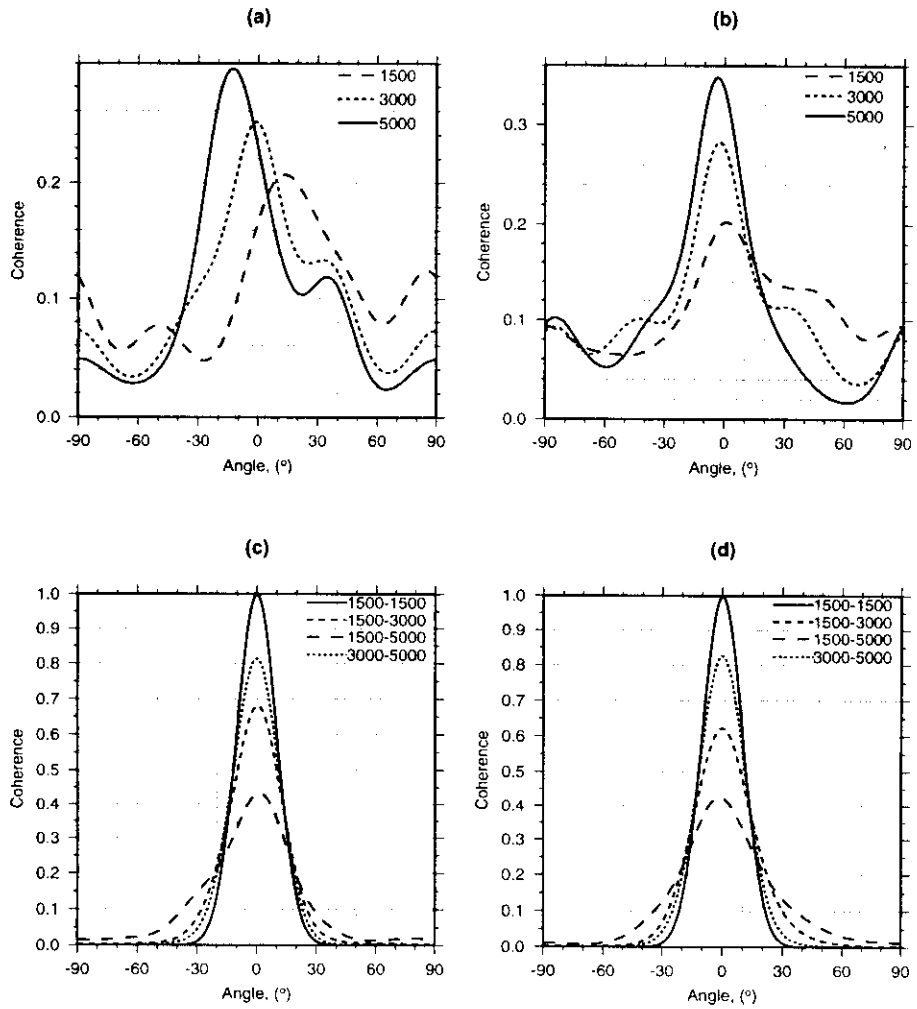

Figure 7.11: The influence of damping on the coherence between Rayleigh wave 2Ψ azimuthal anisotropy maps. (a) Coherence between group velocity anisotropy maps at 50 s period and the global phase velocity anisotropy map at 40 s. Several dampings of the group velocity maps are shown. (b) Similar to (a) but here is the coherence between group velocity anisotropy maps at 100 s period at a variety of dampings and the global phase velocity anisotropy map at 80 s. (c) Coherence between our estimated Rayleigh wave group velocity anisotropy maps at 50 s period obtained using different damping parameters. Contrast the result for self-coherence (solid line). (d) Same as (c), but for the 100 s Rayleigh wave. Numbers in the upper right corner of each graph indicate the magnitude of the damping parameter α_{anis}.

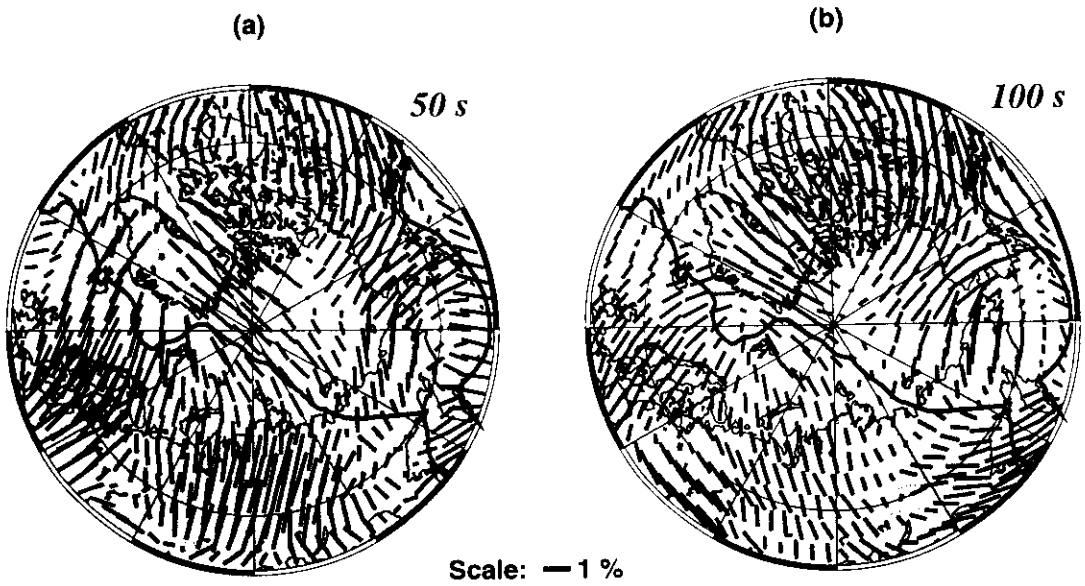

Figure 7.12: Estimated 2Ψ azimuthal anisotropy of Rayleigh wave group velocity at the indicated periods for moderate damping of anisotropy ($\alpha_{anis} = 1500$). (a) 50 s period. (b) 100 s period.

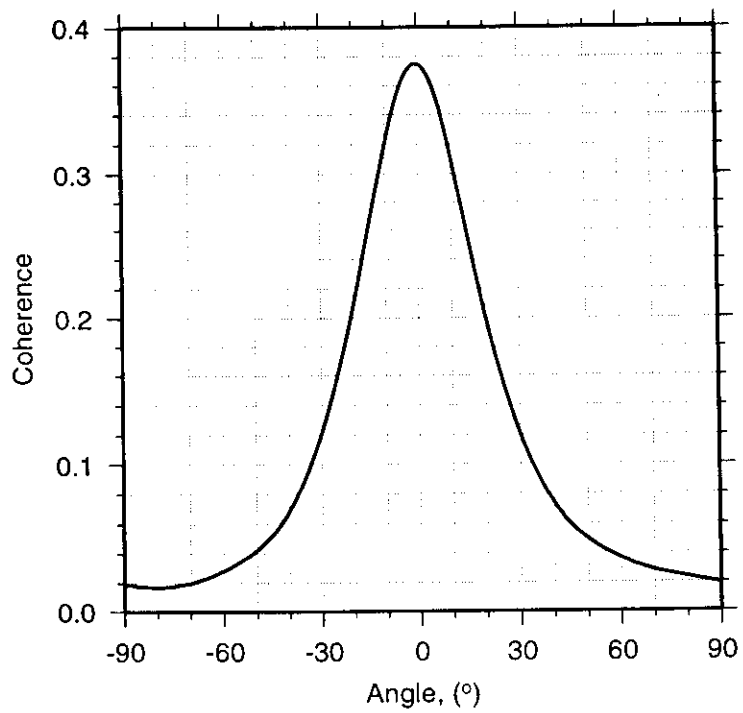

Figure 7.13: Coherence between the two maps shown in Figure 7.12.

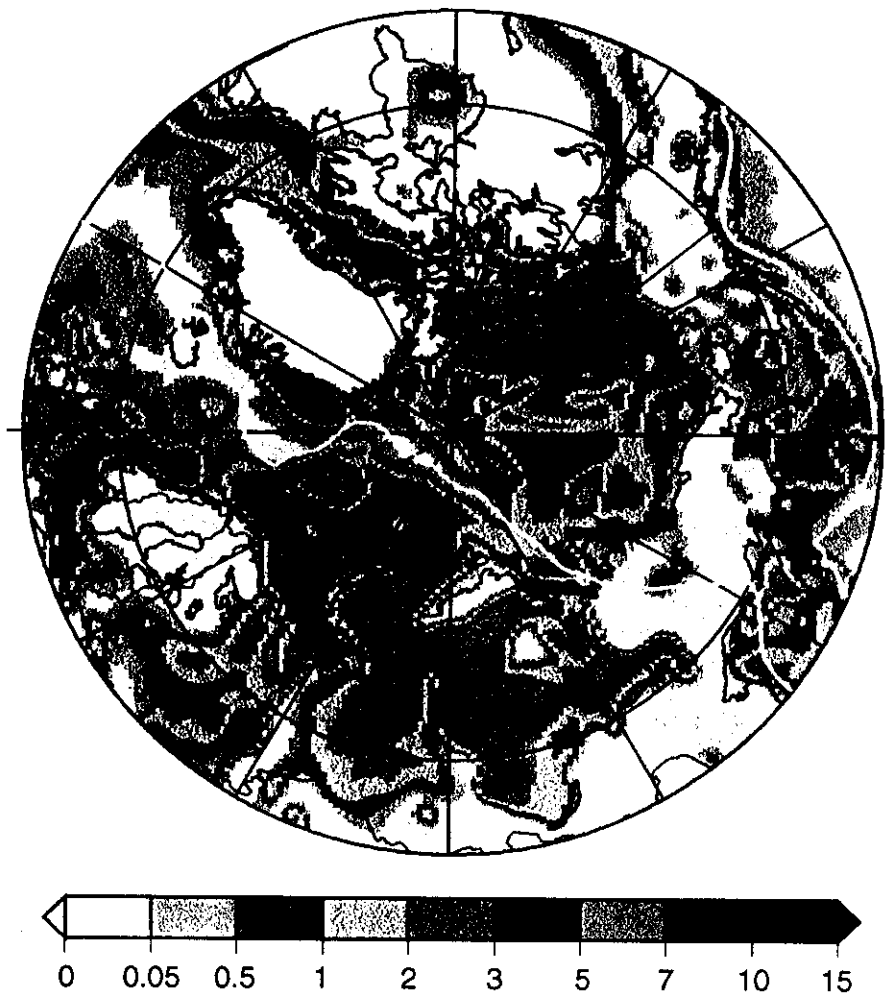

Figure 7.14: Thickness of sediments across the Arctic (Laske and Masters, 1997).

9. Isotropic 3-D Shear Velocity Model Estimation: Central Asia

Summary

We have obtained a shear velocity model for the crust and upper mantle beneath Central Eurasia by simultaneous inversion of broadband group and phase velocity maps of fundamental-mode Love and Rayleigh waves. The model is parameterized in terms of velocity depth profiles on a discrete 2 $\times$ 2 degree grid. The model is isotropic for the crust and for the upper mantle below 220 km but, to fit simultaneously long period Love and Rayleigh waves, the model is transversely isotropic in the uppermost mantle, from the Moho discontinuity to 220 km depth. We have incorporated newly available a priori models for the crust and sedimentary cover, and used them as starting models for the inversion procedure. The crustal part of the estimated model shows good correlation with known surface features such as sedimentary basins and mountain ranges. The velocity anomalies in the upper mantle are related to differences between tectonic and stable regions. Old, stable regions such as the East European , Siberian, and Indian cratons are characterized by high upper-mantle shear velocities. Other large high velocity anomalies occur beneath the Persian Gulf and the Tarim block. Slow shear velocity anomalies are related to regions of current extension (Red Sea and Andaman ridges) and are also found beneath the Tibetan and Turkish-Iranian plateaus, structures originated by continent-continent collision. A large low velocity anomaly beneath western Mongolia might be related to a hypothesized mantle plume. A clear low velocity zone in vSH between Moho and 220 km exists across most of Eurasia but it is absent for vSV. The character and magnitude of anisotropy in the model is on average similar to PREM, with the most prominent anisotropic region occurring beneath the Tibetan Plateau.

1. Introduction

This paper presents a new, high-resolution shear velocity model for the crust and upper mantle of Central Eurasia, obtained by inversion of broadband surface-wave group and phase velocities. We have two main motivations for conducting this study. First, knowledge of the regional structure of the Eurasian crust and upper mantle is fundamental for understanding the tectonic framework and mantle dynamics, posing constraints on possible models of geodynamic evolution. Second, knowledge of the seismic velocity structure is necessary to determine seismic event locations accurately and therefore for monitoring the Comprehensive Nuclear-Test-Ban Treaty (CTBT). The effect of crustal and upper mantle structure is especially important for locating small events, which are recorded only at regional distances. At these close distances body waves propagate exclusively in

the crust and upper mantle and their travel times are affected by strong lateral heterogeneities in this region, and are poorly predicted by one-dimensional Earth models. The Eurasian continent is a natural choice for this type of seismic study. It provides a unique opportunity to study ongoing processes related to continental growth and collision and, from the CTBT monitoring viewpoint, Central Asia is an important and challenging region. A number of nuclear test sites are located in regions of significant structural complexity in Central Asia (Figure 9.1). The study of Eurasia using seismic methods benefits from the Earth's largest intraplate seismic activity, related to the continent-continent collision occurring along the Tethyan orogen (Figure 9.1).

Eurasia is the Earth's largest continent, and contains large regions which have been assembled only relatively recently, over the last 500 m.y. Morphologically it is composed of an assemblage of micro-plates and cratons, separated by mountain ranges or fold belts. The most important event in the recent tectonic history of the continent is the Indo-Asian collision, responsible for the formation of the Himalayas and the Tibetan Plateau. This collision, initiated around 55-50 Ma. ago when the northward moving Indian plate collided with Asia, still continues and provides the opportunity for testing models of continental collision dynamics and continent formation. A large number of researchers have studied the seismic structure of Central Asia, and particularly the Tibetan Plateau. (See Molnar (1988) and Ritzwoller and Levshin (1998) for a review.) Tomographic body wave studies have proven successful in imaging mantle structures, such as subducted slabs, back-arc basins and plumes. However, they provide little information on crustal and uppermost mantle structure, especially in regions without seismic sources and/or receiving stations. Therefore, the structure of large regions of stable Eurasia has not been imaged by body wave studies. Surface wave tomography allows us to fill in these gaps and to improve constraints in the crust and uppermost mantle. Recent advancements in seismic instrumentation, and the installation of high-quality regional networks has improved the quality and resolution of surface wave studies.

2. Data

The data used in this study consist of surface-wave group and phase velocity maps. These maps represent the local group or phase velocity of the fundamental-mode Rayleigh or Love wave at each period, and have been obtained by tomographic inversion of group and phase velocity measurements (dispersion curves). The Rayleigh wave velocity maps used in this study range in period from 15 s to 200 s, and from 15 s to 150 s for Love waves.

The group velocity maps used in this study derive from the dataset of Ritzwoller and Levshin (1998), which has increased in size by about a factor of three. In this continental-scale study they compiled waveform data for events in Eurasia and along the surrounding plate boundaries from global broadband seismograph networks (GSN, Geoscope) and regional networks (CDSN, KAZNET, KNET, MEDNET). Group velocity dispersion curves were measured manually by analysts using the frequency-time analysis method (FTAN) of Levshin et al. (1992). Vertical component seismograms were used to measure Rayleigh wave dispersion, and horizontal component seismograms rotated to the transverse component were used for Love waves. This has resulted now into more than 29,000 measured Rayleigh wave dispersion curves, and more than 22,500 Love wave dispersion curves across Eurasia (20,000 Rayleigh measurements and 16,500 Love measurements inside the model region). The bandwidth of each measurement depends on the ability of the analyst to identify the direct fundamental-mode arrival. At short periods (below 30 s) this arrival may be obscured by scattered waves. For longer periods the fundamental mode may be poorly excited,

particularly for events with magnitudes smaller than 5.0. In addition, it is difficult to obtain high quality measurements for long period Love waves. This procedure results in a different number of measurements for each period, wave type, and location, and consequently a variable resolution of the maps. Figure 9.2 illustrates the differences in ray-path coverage for Love and Rayleigh waves with periods of 40 s and 100 s.

Phase velocity maps have been obtained from the dataset of Trampert and Woodhouse (1995). Unlike the group velocity dataset of Ritzwoller and Levshin (1998), this is a global dataset, derived exclusively from global networks (GSN, Geoscope). The measurement method is automatic and is described in detail in Trampert and Woodhouse (1995). The period range of all measured dispersion curves is identical (40 s 150 s) resulting in the same data coverage for all periods (Figure 9.2). The complete dataset comprises 23,000 measurements for Rayleigh waves, and 16,000 for Love waves. Because this is a global dataset, the ray-path coverage reflects the distribution of global seismicity and global broadband networks, with the highest path density in the northwest Pacific area (Figure 9.2). On the other hand, the dataset of Ritzwoller and Levshin (1998) exhibits its highest path density in Central Asia due to the choice of seismic sources and the existence of dense regional networks (e.g., KNET, Kazakh network, Tibetan Plateau PASSCAL array, etc.).

Because of the distribution of earthquakes and seismic stations, both datasets exhibit considerable redundancy, due to very similar paths. This allows consistency tests, outlier rejection, and the estimation of measurement uncertainties (Ritzwoller and Levshin, 1998). In this procedure ("cluster analysis") measurements with very similar ray paths are binned to produce a cluster or summary ray, resulting in a reduced, cleaner dataset. After this procedure the resulting group velocity dataset consists of 14,000 measurements for Rayleigh waves and 12,000 for Love waves. The phase velocity dataset is reduced to 16,000 Rayleigh wave measurements and 11,000 for Love waves distributed worldwide.

Rather than utilizing the group and phase velocity maps obtained by Ritzwoller and Levshin (1998) and Trampert and Woodhouse (1995) we have estimated new maps using their datasets (significantly incremented for group velocities). The reason is the different parameterization and properties of the two sets of maps. In order to invert phase and group velocity maps simultaneously, it is desirable to make their characteristics more homogeneous. The group velocity maps of Ritzwoller and Levshin (1998) were obtained on a $2^\circ \times 2^\circ$ grid using the method of Yanovskaya and Ditmar (1990). This method is a generalization to two dimensions of a classical one dimensional Backus-Gilbert approach, and sphericity is approximated by an inexact earth flattening transformation. On the other hand, the maps of Trampert and Woodhouse (1995) were parameterized in terms of a spherical harmonic expansion up to degree and order 40. We use the tomographic inversion method of Barmin et al. (2000) to obtain new group and phase velocity maps on a $2^\circ \times 2^\circ$ grid. This method uses spherical geometry, applies spatial smoothing constraints, and allows for the estimation of spatial resolution and amplitude bias of the tomographic images. Examples of the newly obtained group and phase velocity maps are shown in Figure 9.3. Surface wave velocity maps have been obtained for the following periods: Rayleigh group velocities for 15, 20, 25, 30, 40, 50, 60, 70, 80, 90, 100, 125, 150, 175, and 200 seconds; Love group velocities for the same periods only up to 150 seconds; and Love and Rayleigh phase velocities for 50, 60, 70, 80, 90, 100, 125, and 150 seconds. These surface wave dispersion maps will be the data used to invert for shear velocity structure, amounting to a total of 44 velocity data for each geographical grid point.

3. A priori information on crustal structure

In recent years new information on global crustal structure has become available. One of the most important contributions is the global crustal model CRUST5.1 of Mooney et al. (1998). This model is on a $5^\circ \times 5^\circ$ grid, and for each grid point the model is parameterized in terms of a depth profile or column. The columns are divided in two layers of sediments, and a three-layer crystalline crust, in addition to ice and water layers. Thickness, seismic wave velocities (P and S) and density are provided for each layer of the model and also for the uppermost mantle. Although the availability of this model is a great improvement, its resolution (5 degree cells) is not optimal for regional studies, and some large features are not present in the model (e.g., the Tarim basin).

Laske and Masters (1997) have recently compiled a new global sediment model on a $1^\circ \times 1^\circ$ grid. Sedimentary cover in this model is parameterized by three layers. Layer thickness, wave velocities (P and S) and density are assigned for each model cell. The sources of the model in oceans are published digital high-resolution maps, averaged for each $1^\circ \times 1^\circ$ cell. In oceanic basins for which such digital maps are not available (e.g., the Arctic and North Atlantic), the sediment thickness was hand-digitized using atlases and maps. The sediment thickness in most of the continental areas was obtained by digitizing the Tectonic Map of the World (EXXON production research group, 1985).

In addition to global maps, more detailed regional maps and models are available for Eurasia. The Russian Institute of Physics of the Earth (IPE) has published contour maps of sediment and crustal thickness for most of Eurasia (Kunin et al., 1987). These maps are available in digital form from the Cornell Digital Earth project (Seber et al., 1997). Recently a new model of Eurasian crustal thickness has become available, as part of an effort of obtain a global model on a on a $1^\circ \times 1^\circ$ grid (G. Laske, personal communication, 1999). This model utilizes recent data from seismic profiles in Eurasia, but contains large gaps in regions where no seismic refraction data are available (e.g., Afghanistan, Pakistan and Mongolia).

These a priori models of crustal structure are very important for obtaining our shear velocity model. Because the problem of inverting surface wave velocities for shear structure is non-linear, we linearize the problem and solve it iteratively. In this case, to guarantee the convergence of the method to the global minimum solution, it is important to have a good starting model. Therefore a priori models are extremely useful as starting models for velocity structure inversions. Some parameters of the a priori models, such as crustal and sediment thickness, are usually well constrained, especially in regions that have been the target of extensive active source seismic experiments. Other parameters, such as sediment and crystalline crust velocities are, in general, less well know. This knowledge of the properties of the a priori model can also be used in the inversion procedure. Variables that are well known a priori can be tightly constrained to remain near their starting or reference values, while constraints on other variables can be loosened.

4. Inversion method

We parameterize our three-dimensional shear velocity model in terms of one-dimensional, depth-dependent velocity profiles determined at each node of a $2^\circ \times 2^\circ$ grid. In this point-by-point inversion, the data are the values at the grid point of spatially smoothed group and phase velocity maps for Rayleigh and Love waves at all periods. Each depth profile is divided into 4 layers: sediments, crystalline crust, uppermost mantle (Moho 220 km), and 220 400 km (Figure 9.4).

Surface topography, and water and ice layers are also considered in the model, but their thickness and velocity are kept constant. For an isotropic parameterization, the model variables estimated in the inversion are: sediment velocity (constant), basement topography, crystalline crust velocity (constant and slope), Moho topography, uppermost mantle velocity (constant and slope), and velocity between 220 km and 400 km. He have chosen this simple parameterization in order to enhance the resolving power of the data while maintaining a physically reasonable model. However, as it will be discussed later, this simple isotropic parameterization is unable to fit simultaneously the long period Love and Rayleigh wave data in large regions in Eurasia. This discrepancy between long period Love and Rayleigh wave data in continental regions is well known, and has been addressed before by permitting transverse isotropy in the uppermost mantle (Dziewonski and Anderson, 1981). We have also incorporated transverse isotropy in our parameterization, by introducing two shear velocities, vSH and vSV, between Moho and 220 km depth, with the constraint that vSH = vSV at 200 km (Figure 9.4). The velocity of horizontally polarized S waves, vSH, affects Love wave velocities, and the velocity for vertically polarized S waves, vSV, affects Rayleigh waves. Therefore, the introduction of these two velocities effectively decouples the Love and Rayleigh wave velocities for long periods, allowing the inversion to fit them simultaneously. The inversion method uses the general linear inverse approach and is described further by Ritzwoller et al. (2000, manuscript in preparation).

The starting model for the inversion is a combination of a priori crustal and mantle models. Sediment thickness and velocities are obtained form the global map of Laske and Masters (1997). Where available, we use the new Eurasia crustal thickness map (G. Laske, personal communication, 1999), and we fill the gaps with the IPE map of crustal thickness (Kunin et al., 1987; Seber et al., 1997) and CRUST5.1 (Mooney et al., 1998). The resulting reference models of sediment and crustal thickness are shown in Figure 9.5. For the mantle we use as a starting model the model S16B30 (Masters et al., 1996). This is an isotropic global mantle model, containing only very long wavelength features. Using this compilation of a priori information, for each point in our $2^\circ \times 2^\circ$ grid we construct a starting depth profile, following the parameterization shown in Figure 9.4. The starting model is isotropic (vSH = vSV) but during the inversion, transverse isotropy will be introduced between the top of the mantle (below Moho) and 220 km depth.

5. Results

Figure 9.6 shows a typical example of the inversion results and data fit. The estimated models shown here correspond to a grid node located in western Mongolia (48 N, 95 E), using isotropic and transversely isotropic parameterizations. The estimated isotropic model (Figure 9.6a) is unable to fit simultaneously the Love and Rayleigh wave data, although it develops a prominent low velocity zone below the Moho in the attempt to do so. The model fits Love wave group velocities well but overestimates Rayleigh wave velocities between 40 s and 100 s (Figure 9.6a, top right panel). Interestingly, the situation is reversed for phase velocities: the model fits the long period Rayleigh data (80 s 150 s) well, but under-predicts long period Love wave velocities.

Transverse isotropy has been invoked in previous studies to explain this Love wave-Rayleigh wave discrepancy for periods relevant to the upper 200 km or so of the mantle (e.g., Dziewonski and Anderson, 1981). The introduction of two velocities in this depth range, vSH for horizontally polarized S waves and vSV for vertically polarized S waves, effectively decouples the two data types, because Rayleigh waves are sensitive mostly to vSV while Love waves are sensitive to vSH.

Figure 9.6b shows the inversion results and data fit for a transversely isotropic parameterization. In the region between Moho and 220 km depth, vSH is greater than vSV and a low velocity zone is present in vSH but not in vSV. This parameterization substantially improves data fit, as shown in Figure 9.6b. Love and Rayleigh wave velocities are now fit simultaneously, although the model still underestimates Love wave group velocities between 50 s and 60s. We have adopted this transversely isotropic parameterization for all grid points in the model. Our goal is to define a simple model parameterization, while maintaining a physically reasonable model. For the model described in this section, 8 parameters are estimated for each depth profile based on 44 data points (surface wave velocities).

Comparisons between surface wave group and phase velocity maps and predicted maps from the estimated shear velocity model provide a qualitative estimate of the data fit. Figure 9.7 shows maps for 50 s Rayleigh wave group velocities and 100 s Rayleigh wave phase velocities, and theoretical maps calculated from our estimated shear velocity model. The agreement between the maps and model predictions is fairly good, particularly for long-wavelength features.

The resolution of the shear velocity model (depth profile) at a given grid point depends on the resolution and quality of the surface wave velocity maps for that point. Maps for each period and wave type have different spatial resolutions depending on the path density, azimuthal coverage and quality of the measurements used (see Figure 9.2). For group velocities, coverage is very high inside the model region (box in Figure 9.2), but decreases across the Arabian peninsula and southern India. Path density for phase velocities is in general lower than for group velocities (50 ray paths for each $2^\circ \times 2^\circ$ node on average; Figure 9.2). The Arabian peninsula and southern India are also regions of lower phase velocity path coverage, so we expect lower quality of the shear velocity model in these areas. Path density and azimuthal coverage are fairly good for the rest of the model. Because the inversion procedure is on a point-by-point basis and the surface wave velocity maps extend well beyond the model boundaries, edge effects do not occur. In terms of depth resolution, a degradation is expected below 220 km because of the number and quality of measurements decrease toward longer periods, especially for Love waves.

The crustal part of the shear velocity model is presented here as maps of sediment and crustal thickness (Figure 9.8). Results correlate well with known tectonic features, such as sedimentary basins, cratons and orogens. Estimates of sediment and crustal thickness after inversion are similar to the starting values, and all major sedimentary basins are present in the final model. This is a predictable result because low velocity features associated with major basins are clearly present in the short period surface wave velocity maps (e.g., Ritzwoller and Levshin, 1998). Crustal thicknesses beneath the Himalayas, Hindu-Kush, Tibetan Plateau and Tien Shan are not significantly changed relative to the starting model. However, in the Caucasus, Urals and Zagros the estimated crustal thickness is smaller that the starting model, resulting in less prominent crustal roots for these regions (Figure 9.8b).

The upper mantle velocity structure (vSV) at a depth of 100 km is shown in Figure 9.9a. The most obvious features of the model are the high velocity anomalies associated with the East European platform, Siberian platform, and northern Indian shield. Some other positive anomalies smaller in extent are found beneath large sedimentary basins: eastern Mediterranean, Caspian Depression, Persian Gulf, and Tarim basin. Low velocities are associated with a segment of the Alpine-Himalaya collision zone extending from Turkey to Iran and Afghanistan. The western Arabian peninsula, Red Sea, and the Afar triangle region in northeast Africa are also underlain by large low velocity anomalies. Large low velocity regions also extend beneath Indochina and the

South China Sea, and beneath Mongolia, with its largest anomalies occurring southwest of lake Baikal. Smaller low velocity anomalies can also be found in northern Tibet, and south of lake Balkhash.

For comparison, Figure 9.9b shows the S velocity model of Bijwaard et al. (1998), obtained by inversion of body wave arrival times from the dataset of Engdahl et al. (1998). The agreement is very good in regions where both models are well constrained, with most of all long-wavelength features present in both models, although the magnitude of the velocity anomalies is generally smaller in the model of Bijwaard et al. (1998). When comparing both models we must take into account that the model of Bijwaard et al. (1998) is an isotropic model of S-wave velocity, vS, which is unconstrained for shallow layers without seismic sources and/or receivers (e.g., the East European and Siberian cratons).

The strength and distribution of transverse isotropy is shown in Figure 9.10 as the difference between vSH and vSV at 80 km depth. Values greater than zero indicate transverse isotropy with vSH ¿ vSV and negative values indicate reverse anisotropy in which vSV ¿ vSH. Because of our parameterization, the difference between vSV and vSH is largest just beneath Moho and decreases to zero at 220 km depth. This situation is analogous to PREM for which the difference vSH - vSV just beneath Moho is 0.22 km/s, equivalent to a intrinsic anisotropy of 4.8%. At 80 km depth, the difference vSH - vSV for PREM is 0.15 km/s or 3.4%. As can be seen in Figure 9.10, the mantle beneath Eurasia is transversely isotropic with average values similar to PREM. Regions of larger than average anisotropy are also found beneath north and central Tibet, Afghanistan and Burma. Anisotropy is large in the western Arabian peninsula but this result is less reliable than for other regions because of the decrease in coverage of the surface wave velocity maps in this area. The reliability of the vSH model is in general lower than the vSV model due to the smaller number and quality of the Love wave data at long periods. In addition, the existence of reverse anisotropy (vSV ¿ vSH) is questionable, occurring predominantly in regions where the long period group and phase velocity maps are inconsistent (e.g., in the East European Platform). We expect that the incorporation of additional phase and group velocity data will improve the agreement between the maps and eliminate these anomalous regions.

The existence of a low velocity zone (LVZ) is determined by the sign of the vertical gradient of vSH and vSV between Moho and 220 km depth. A negative velocity gradient indicates a LVZ and a positive gradient indicates the absence of a LVZ. Figure 9.11 shows that a LVZ in vSH is pervasive across Eurasia, but is very small or absent in vSV. This behavior in the uppermost mantle is consistent with PREM. Regions with a pronounced low velocity zone (greater than PREM) in vSH include both mountain ranges and stable continental blocks. Tectonically active regions, including the Tibetan Plateau, Hindu-Kush and Zagros, exhibit the most well developed low velocity zones. Some stable regions such as the western part of the East European platform, Kazakh platform, Arabian peninsula and Indian subcontinent also display prominent low velocity zones in vSH.

6. Discussion

As shown in Figure 9.9, the old, stable cratons located north of the Alpide-Himalayan orogenic belt are characterized by high upper-mantle shear velocities. High shear velocities are also found beneath the Indian shield, the southern Tibetan Plateau, and the Tarim basin (Figure 9.9). While high shear velocities in the upper mantle are usually interpreted as an indication of old, cold, thick lithospheric blocks, the structures associated with low velocity anomalies are more difficult

to interpret. Large low velocity anomalies are associated with young, extensional plate boundaries, as the Red Sea and Andaman ridges. The low velocity anomaly beneath central and northern Tibet has received a great deal of attention (see Molnar, 1988) because of its implications for the origin and mechanism for the formation of the Tibetan plateau. However, although clearly present in our model and in the model of Bijwaard et al. (1998), it is not one of the most prominent anomalies in magnitude or in extension. Based upon the presence of this low velocity region and other evidence (e.g., widespread Quaternary volcanism and inefficient Sn propagation) Molnar et al. (1993) proposed that the high-velocity Indian lithosphere has not been underthrusted beneath the Tibetan Plateau, and that crustal thickening has occurred by north-south shortening of southern Eurasia's crust. As a result, flow in the mantle under Tibet is probably from west to east, because it would be blocked in the west by the keel of the Tarim block. This is supported by the orientation of SKS fast polarization directions (McNamara et al., 1994) and by evidence of correlated crust and mantle strain fields in Tibet (Holt, 2000). Anisotropy (transverse isotropy) in our model is largest beneath Tibet (Figure 9.9) although the relationship between mantle flow and the strength of transverse isotropy is poorly understood.

One of the most prominent upper mantle low velocity regions is located in the Middle East, extending from Turkey to Iran and western Afghanistan (Figure 9.9). This low velocity anomaly coincides with the Turkish-Iranian continental plateau, formed by the collision between the Arabian and Eurasian plates. This collision is the result of the closing of the Neo-Tethys Ocean by northward subduction of oceanic lithosphere beneath Eurasia. In Iran and western Afghanistan, the low velocity anomaly is bounded to the south by high velocities, part of the Arabian plate. The low velocity anomaly is also a prominent feature in the global model of Bijwaard et al. (1998; Figure 9.9b) and in Pn tomography studies (e.g., Hearn and Ni, 1994), and is also coincident with a region of high S-wave attenuation (Kadinsky-Cade et al., 1981) and Neogene volcanism (Kazmin et al., 1986). The combination of these observations suggests a hot or perhaps partially molten uppermost mantle beneath the Turkish-Iranian Plateau. This anomalously hot upper mantle could be a remnant of the backarc extension regime that dominated this region from the Jurassic to the Neogene (Dercourt et al., 1986). The presence of hot, molten upper mantle weakens the lithosphere, allowing larger deformation associated with the Arabian plate-Eurasia collision. This results in the observed diffuse intraplate seismicity that extends well to the north of the plate boundary delineated by the Zagros Main Thrust. Furthermore, the buoyancy associated with hot upper mantle, combined to the buoyancy due to the deep continental roots in the region, can contribute to maintain the high topography of the plateau.

Another significant upper-mantle low velocity anomaly is centered in western Mongolia, WSW of lake Baikal (Figure 9.9). The central part of this anomaly coincides with the Hangay Dome area of central Mongolia. The Hangay Dome is characterized by recent uplift, diffuse extension and regionally upwarped topography (Cunningham, 1998). This is also a region of recent Cenozoic volcanism and high heat flow (with a maximum of approximately 80 mW/m2). There is a remarkable agreement between the shape of the velocity anomaly (Figure 9.9a) and the heat flow anomaly (Figure 5a of Cunningham, 1998). This region in Mongolia has previously been interpreted to overlie a mantle plume or asthenospheric diapir that also extends beneath the Baikal region in Siberia (Windley and Allen, 1993). This region displays high seismic activity, and has been the place of some of the largest intraplate earthquakes recorded during this century (i.e., 1905 and 1957). Tectonic stresses produced by the impingement of the mantle plume on the base of the lithosphere might be responsible for the seismotectonic behavior of the region (Cunningham, 1998).

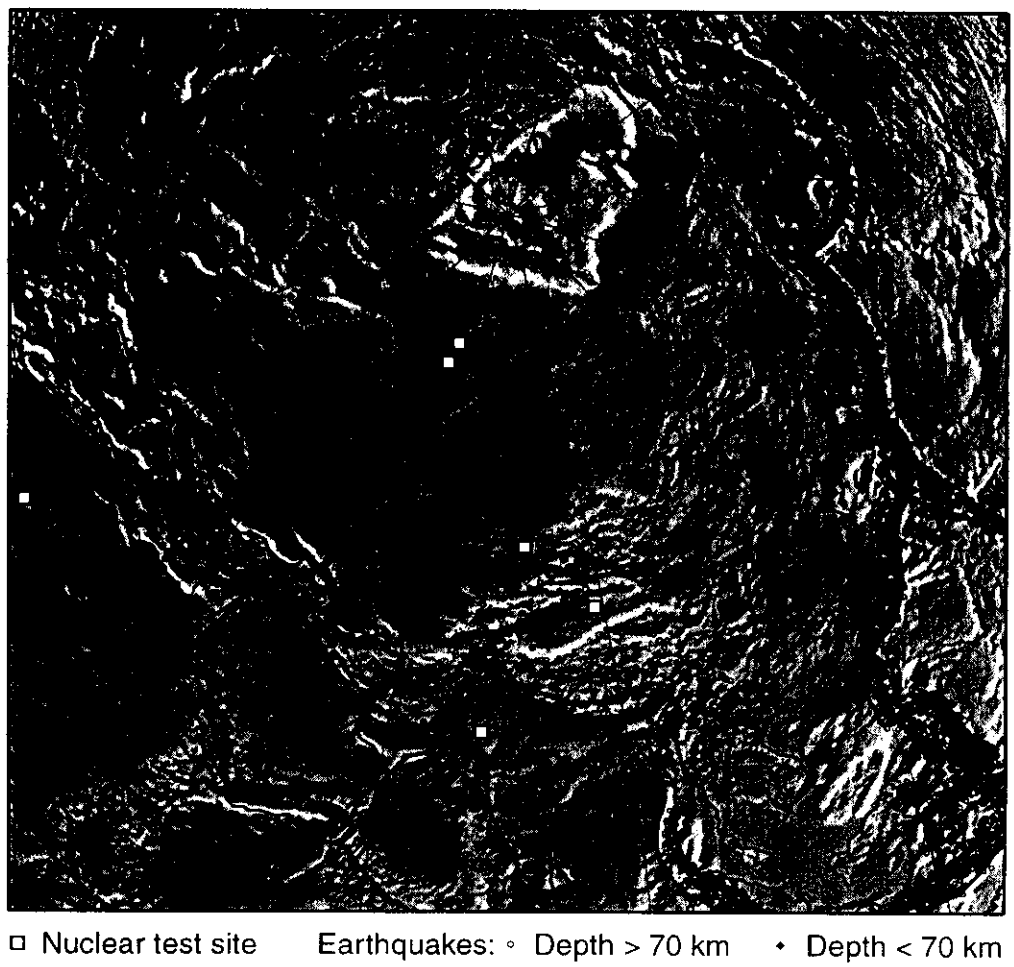

Figure 9.1: Location map of the studied region. The thick black box outlines the boundaries of the shear velocity model presented here. Earthquake hypocenters are from the dataset of Engdahl et al. (1998). Note the high level of diffuse intraplate seismicity extending from the eastern Mediterranean to Southeast Asia. White squares show the location of nuclear test sites in the region.

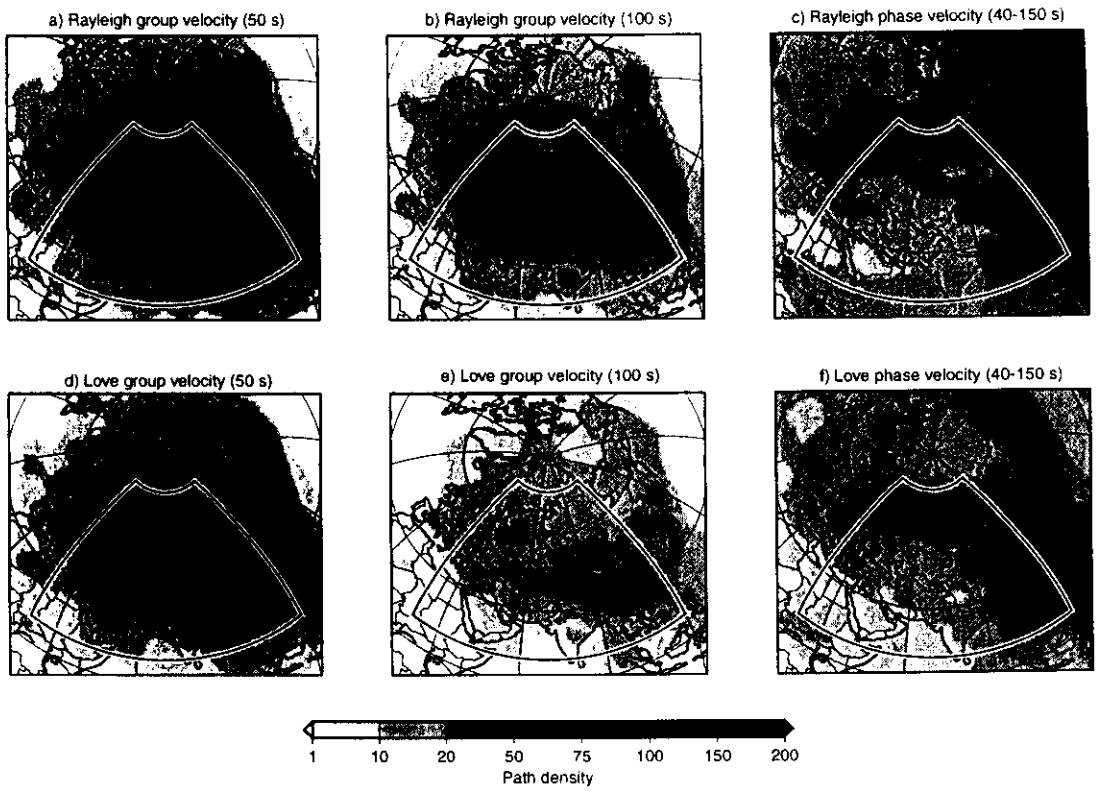

Figure 9.2: Path density maps for group and phase velocity for the following waves and periods: a) 50 s Rayleigh wave group velocity, b) 100 s Rayleigh wave group velocity, c) 50-150 s Rayleigh wave phase velocity, d) 50 s Love wave group velocity, e) 100 s Love wave group velocity, and f) 50-150 s Love wave phase velocity. Path density is defined as the number of great circle ray paths that cross each $2^\circ \times 2^\circ$ degree cell. For group velocities, path density maps are different for each wave type and period. For phase velocities, the distribution of paths for each wave type is identical for the entire period band of the measurements (50 s 150 s).

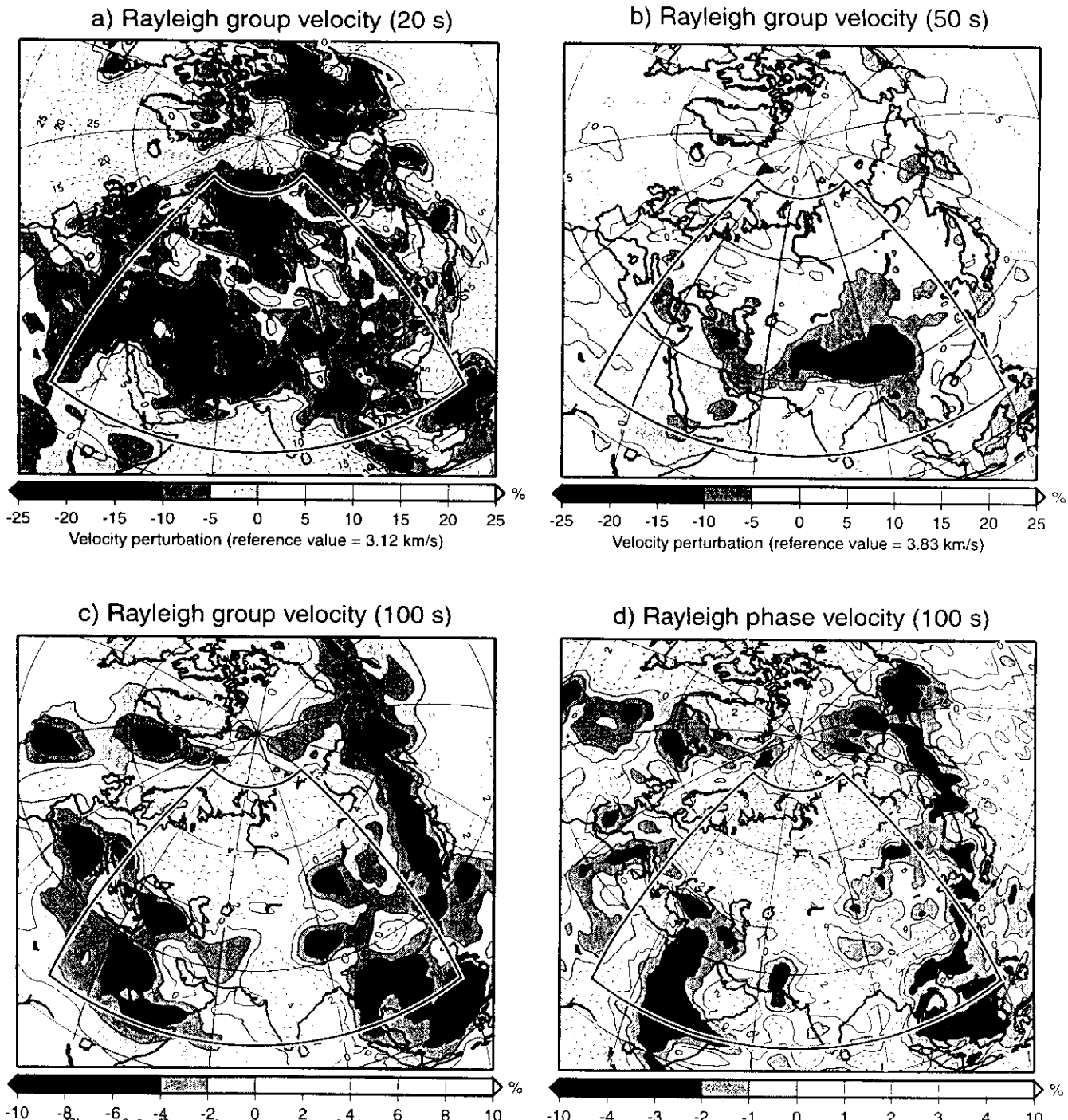

Figure 9.3. Examples of group and phase velocity maps obtained by tomographic inversion of surface wave dispersion measurements: a) 20 s Rayleigh wave group velocity, b) 50 s Rayleigh wave group velocity, c) 100 s Rayleigh wave group velocity, and d) 100 s Rayleigh wave phase velocity.

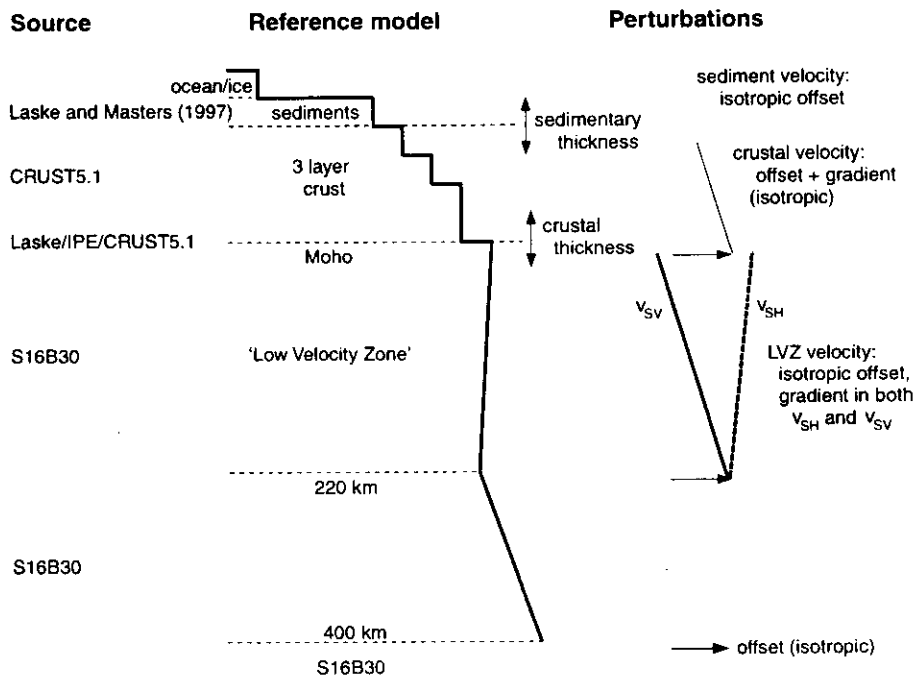

Figure 9.4: Parameterization of the shear velocity model. A one-dimensional velocity profile is estimated for each node of the 2° × 2° degree geographic grid.

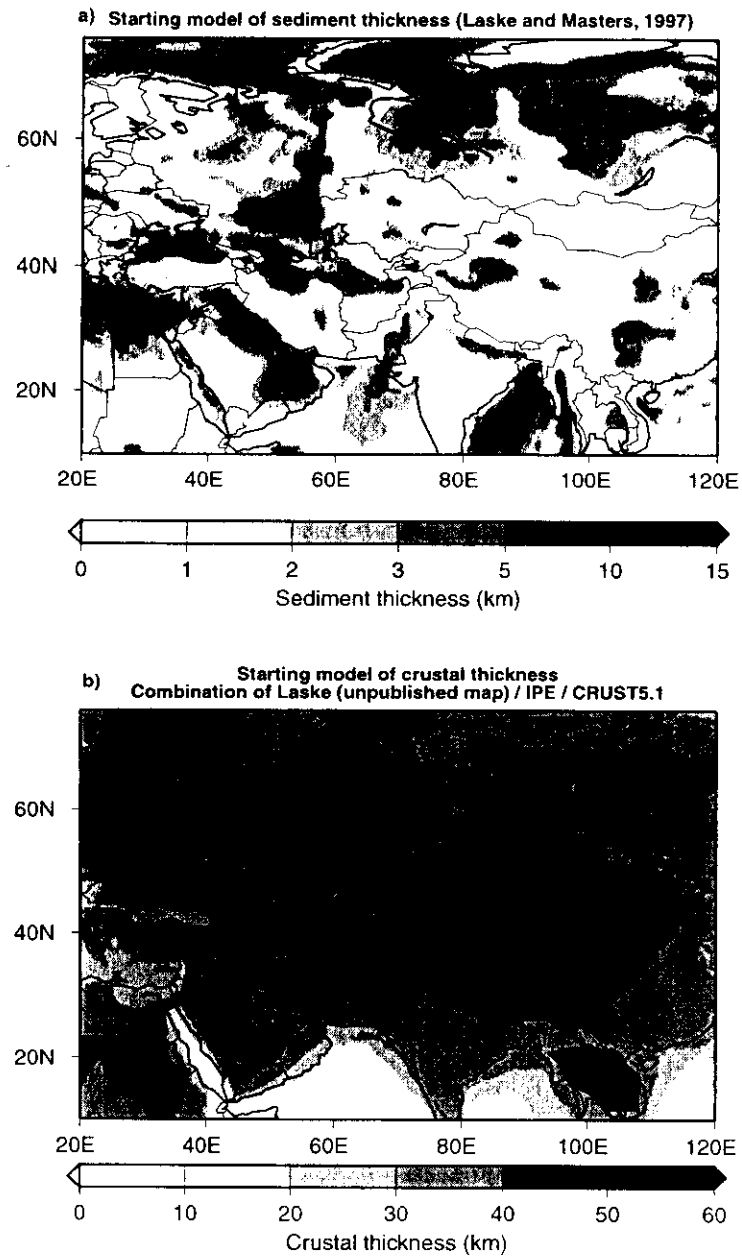

Figure 9.5: A priori crustal information used as starting/reference model for the shear velocity inversion: a) sediment thickness model of Laske and Masters (1997), and b) crustal thickness model obtained by combining regional models for Eurasia (Kunin et al., 1987; G. Laske, personal communication) and global models (Mooney et al., 1998).

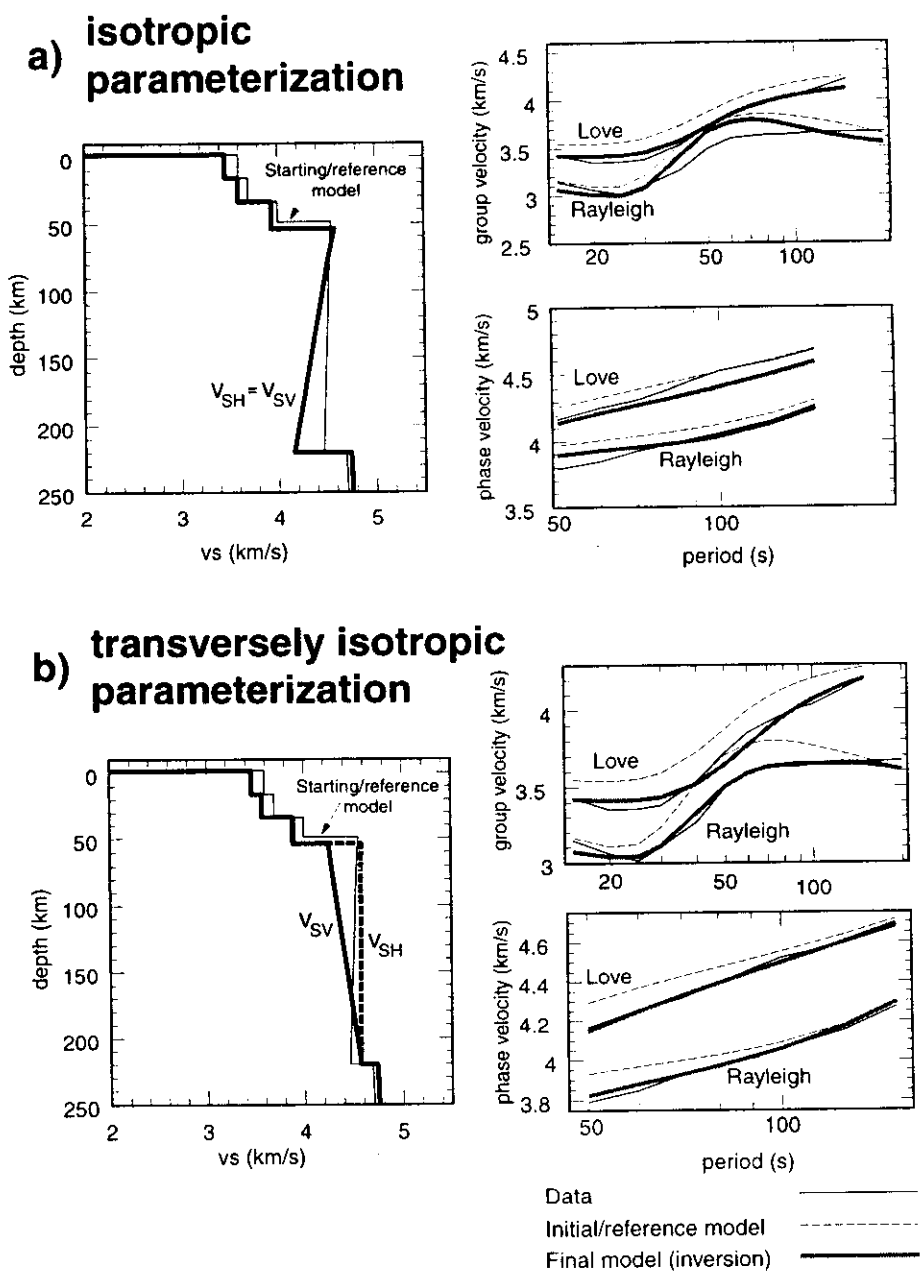

Figure 9.6: Inversion results and data fit for a point in western Mongolia with coordinates 48 N, 95 E. a) Isotropic model parameterization (vSH = vSV). The left panel shows the starting and final (after inversion) models. The top right panel shows the data fit for group velocities (period band 20 s 200 s), and the bottom right panel shows the data fit for phase velocities (period band 50 s 150 s). The thin solid lines represent the data, the thin dashed lines show the predictions from the starting model, and the thick gray lines are the result of the inversion. b) Transversely isotropic parameterization (vSH not equal to vSV between Moho and 220 km depth, and isotropic for all other depths). Symbols as in previous panels.

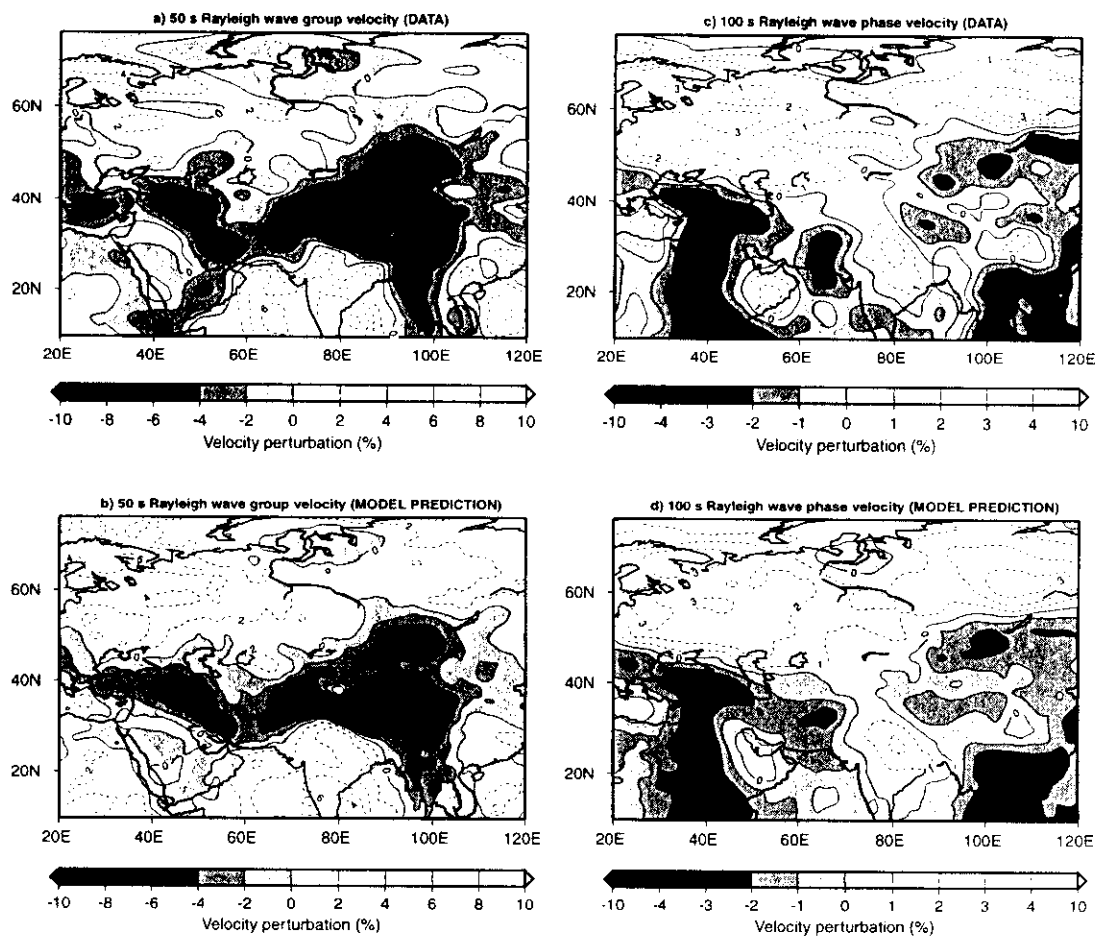

Figure 9.7: Comparison between surface wave group and phase velocity maps (data) and predictions from the shear velocity model obtained in this study: a) group velocity map for 50 s Rayleigh waves (data), b) model predictions, c) phase velocity map for 100 s Rayleigh waves (data), and d) model predictions.

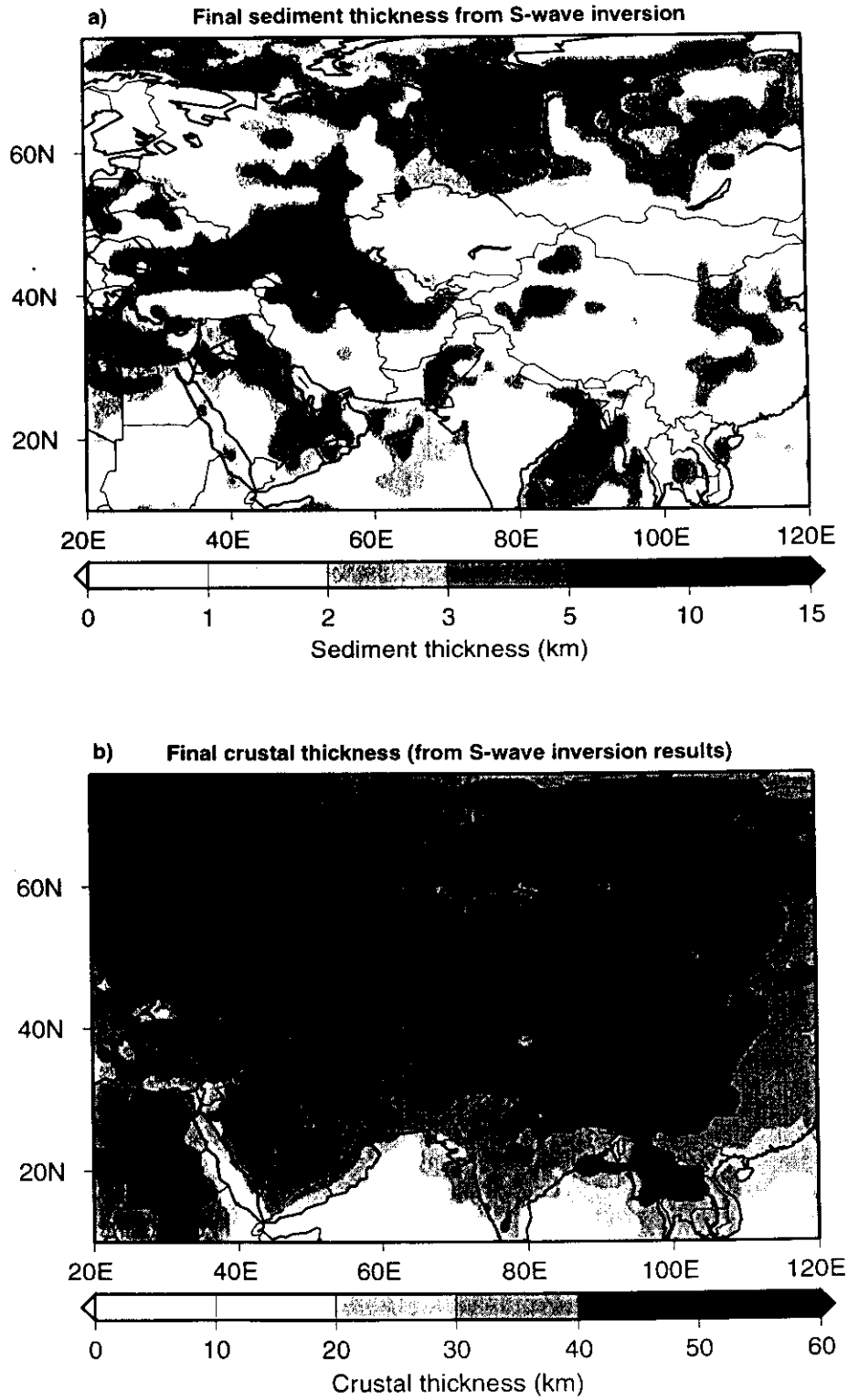

Figure 9.8: Inversion results for a) sediment and b) crustal thicknesses. Compare results with starting/reference model (Figure 9.5).

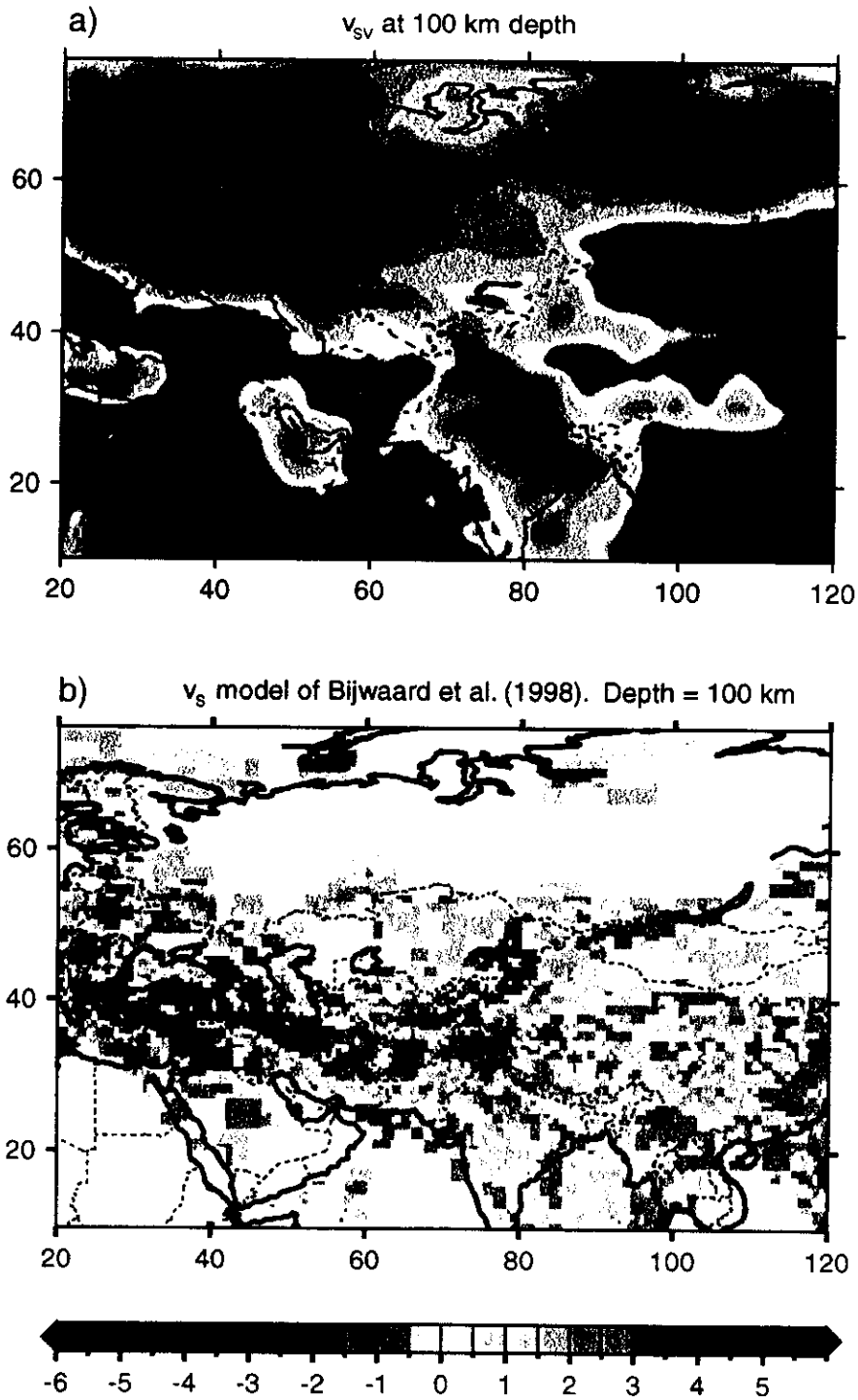

Figure 9.9: Shear velocity structure in S-wave velocity perturbation (%) at 100 km depth). a) vSV velocity obtained in this study by inversion of surface wave velocities. b) vS model of Bijwaard et al. (1998) obtained by inversion of S-wave arrival times.

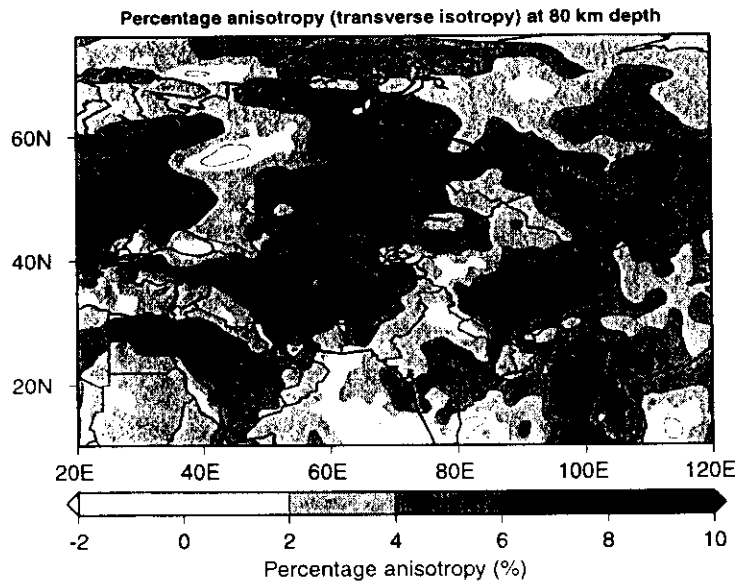

Figure 9.10: Strength of anisotropy (transverse isotropy) at 80 km depth. The values displayed are percentage anisotropy, defined as 200(vSH - vSV)/ (vSH+vSV). Positive values indicate vSH ¿ vSV. The percentage anisotropy value for PREM at 80 km depth is 3.4%.

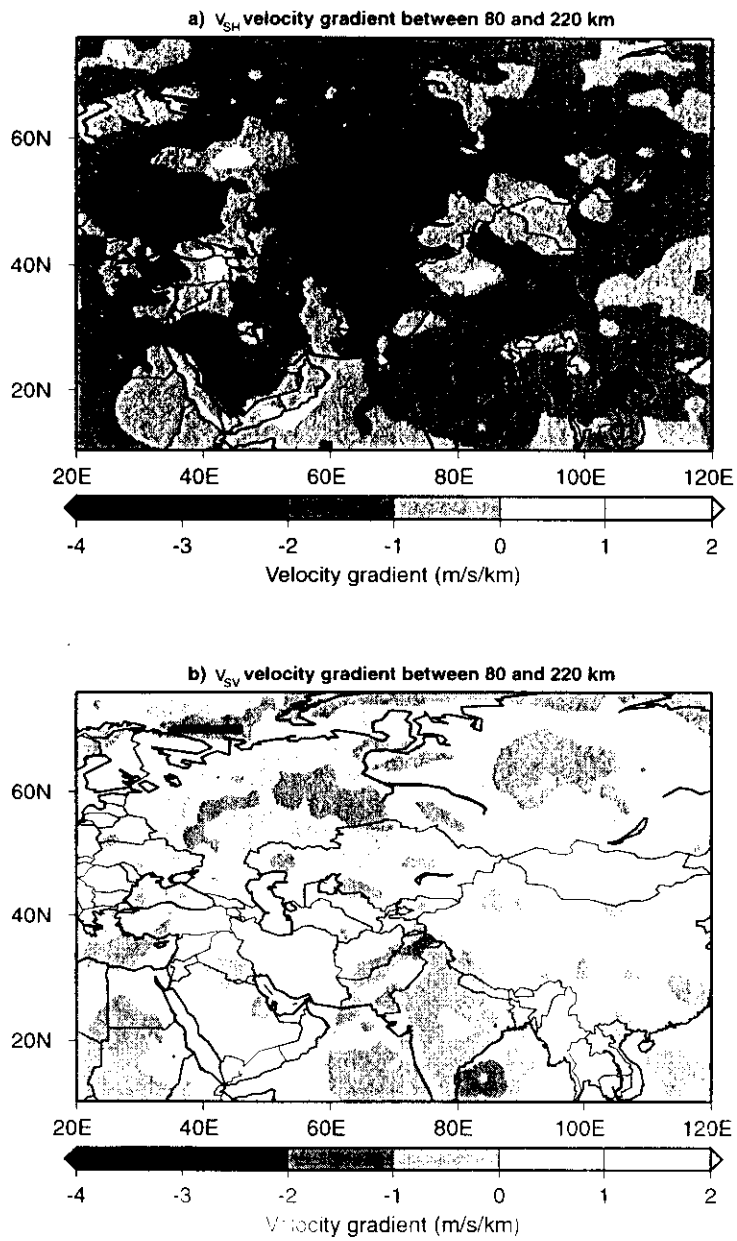

Figure 9.11: Velocity gradient of the shear velocity model between Moho and 220 km depth. A positive value indicates that velocity increases with depth. A negative value indicates the existence of a low velocity zone in this depth range. Units are m/s/km. a) Velocity gradient for vSH, and b) velocity gradient for vSV. A low velocity zone is pervasive for vSH and mostly absent for vSV.

References

Ch. 1 - 10

Aki, K., and P.G. Richards, Quantitative Seismology, **II**, W.H. Freeman and Co., 1980.

Alsina, D., and R. Snieder, Constraints on the velocity structure beneath the Tornquist-Teisseyre Zone from beam-forming analysis, *Geophys. J. Int.*, *126*, 205-218, 1996.

Anderson, J., W. E. Farrell, K. Garcia, J. Given, H. Swanger, Center for Seismic Studies Version 3 Database: Schema Reference Manual, CSS Technical Report C90-01, September, 1990.

Arfken, G., Mathematical methods for physicists, Academic Press, third edition, New York, 1985.

Aurenhammer, F., Voronoi diagrams: A survey of fundamental geometric data structure, *Assoc. Comput. Mach. Comput. Surv.*, **23** (3), 345-405, 1991.

Backus, G., and J.F. Gilbert, Resolving power of gross earth data, *Geophys. J. R. Astron. Soc.*, *16*, 169-205, 1968.

Backus, G., and J.F. Gilbert, Uniqueness in the inversion of inaccurate gross earth data, *Philos. Trans. R. Soc. London, Ser. A*, *266*, 123-192, 1970.

Barmin, M.P., A.L. Levshin, and M.H. Ritzwoller, A fast and reliable method for surface wave tomography, *PA-GEOPH*, in press, 2000.

Bijwaard, H., W. Spakman, and E.R. Engdahl, Closing the gap between regional and global travel time tomography, *J. Geophys. Res.*, **103**, 30055- 30078, 1998.

Bird, P., and M.N. Toksoz, Strong attenuation of Rayleigh waves in Tibet, *Nature*, *266*, 161-163, 1977.

Biswas, N. N., Earth-flattening procedure for the propagation of Rayleigh waves, *Pageoph.*, **96**, 61-74, 1972.

Biswas, N. N. and L. Knopoff, Exact Earth-flattening calculation for Love waves, *Bull. Seism. Soc. Am.*, **60**, 1123-1137, 1970.

Bolt, B. A. and J. Dorman, Phase and group velocities of Rayleigh waves in a spherical, gravitating Earth, *J. Geophys. Res.*, **66**, 2965-2981, 1961.

Bourjot, L., and B. Romanowicz, Crust and upper mantle tomography in Tibet using surface waves, *Geophys. Res. Lett.*, *19*, 881-884, 1992.

Brandon, C., and B. Romanowicz, A "no-lid" zone in the central Chang-Thang platform of Tibet: Evidence from pure path phase velocity measurements of long-period Rayleigh waves, *J. Geophys. Res.*, *91*, 6547-6564, 1986.

Braun, J., and M. Sambridge, A numerical method for solving partial differential equations on highly irregular evolving grids, *Nature*, **376**, 665-660, 1997.

Byerly, P., The dispersion of seismic waves of the Love type and the thickness of the surface layer of the Earth under the Pacific, *Beitr. Geophys.*, *26*, 27-33, 1930.

Calcagnile, G., and G. F. Panza, Crust and upper mantle structure under the Baltic Shield and Barents Sea from the dispersion of Rayleigh waves, *Tectonophysics*, *47*, 59-71, 1978.

Calcagnile, G., and G. F. Panza, Crustal and upper mantle structure beneath the Apennines region as inferred from the study of Rayleigh waves, *J. Geophys.*, *45*, 319-327, 1979.

Calcagnile, G., and G. F. Panza, Upper mantle structure of the Apulian plate from Rayleigh waves, *Pure Appl. Geophys.*, *118*, 823-830, 1980.

Calcagnile, G., and G. F. Panza, Crustal and upper mantle structure of the Mediterranean area derived from surface-wave data, *Phys. Earth Planet. Inter.*, *60*, 163-168, 1990.

Calcagnile, G., G. F. Panza, and L. Knopoff. Upper mantle structure of north-central Italy from Rayleigh waves phase velocities, *Tectonophysics, 56*, 51-63, 1979.

Calcagnile, G., U. Mascia, V. del Gaudio, and G. F. Panza, Deep structure of southeastern Europe from the dispersion of Rayleigh waves, *Tectonophysics, 110*, 93-111, 1985.

Cara, M., Filtering of dispersed wave trains, *Geophys. J. R. Astron. Soc., 33*, 65-80, 1973.

Chapman, C. H., The Earth flattening transformation in body wave theory, *Geophys. J. R. Astron. Soc.*, **35**, 55-70, 1973.

Chan, W.W., and B.J. Mitchell, Surface wave dispersion, crustal structure and sediment thickness variations across the Barents shelf. Geoph. J. R. astr. Soc., 80, 329-344, 1985.

Chan, W. W., and B.J. Mitchell, Regional variations in the crustal structure of Northern Canada from surface wave dispersion, Geodynamics, 6, 53-69, 1986.

Chen, W.-P., and P. Molnar, Short-period Rayleigh wave dispersion across the Tibetan Plateau, *Bull. Seismol. Soc. Am., 65*, 1051-1057, 1975.

Chun, K.Y, and T. Yoshii, Crustal structure of the Tibetan Plateau: A surface wave study, *Bull. Seismol. Soc. Amer., 67*, 735-750, 1977.

Coles, R.L. and P.T. Taylor, Magnetic anomalies. In The Arctic Ocean Region, The Geology of North America, A. Grantz, L. Johnson, and J. F. Sweeney (eds), Boulder, Colorado, GSA, L, 119 - 132, 1990.

Cunningham, W.D., Lithospheric controls on late Cenozoic construction of the Mongolian Altai, *Tectonics*, **17**, 891-902, 1998.

Curtis, A., B. Dost, J. Trampert and R. Snieder, Eurasian fundamental mode surface wave phase velocities and their relationship to tectonic structures, *J. Geophys. Res.*, **103**, No. B11, pp. 26,919-26,947, 1998.

Curtis, A. and J. H. Woodhouse, Crustal and upper mantle shear velocity structure beneath the Tibetan plateau and surrounding regions from inter-event surface wave phase velocity inversion, *J. Geophys. Res.*, **102**, No. B6, pp. 11,789-11,813, 1997.

Dahlen, F. A., The normal modes of a rotating, elliptical Earth, *Geophys J. R. Astron. Soc.*, **16**, 329-367, 1968.

Das, T., and G. Nolet, Crustal thickness using high frequency Rayleigh waves, *Geophys. Res. Lett., 22*, 539-542, 1995.

Dercourt, J. and 18 others, Geological evolution of the Tethys belt from the Atlantic to the Pamirs since the Lias, *Tectonophysics*, **123**, 241-315, 1986.

Derr, J., A comparison of free oscillations of oceanic and continental Earth-models, *Bull. Seism. Soc. Am.*, **57**, 1047-1061, 1967.

Ditmar, P.G., and T.B. Yanovskaya, A generalization of the Backus-Gilbert method for estimation of lateral variations of surface wave velocity (in Russian), *Izv. Akad. Nauk SSSR, Fiz. Zemli, 6*, 30-60, 1987.

Dost, B., Upper mantle structure under western Europe from fundamental and higher mode surface waves using the NARS array, *Geophys. J. Int., 100*, 131-152, 1990.

Dziewonski, A. M., Bloch, S., and M. Landisman, 1969. A technique for the analysis of transient seismic signals, *Bull. seism. Soc. Am.*, **59**, 427 - 444, 1969.

Dziewonski, A.M., On regional differences in dispersion of mantle waves, *Geophys. J. R. Astron. Soc., 22*, 289-325, 1971.

Dziewonski, A. M., and D. L. Anderson, Preliminary reference Earth model. *Phys. Earth Planet. Inter., 25*, 297-356, 1981.

Dziewonski, A. M., S. Bloch, and M. Landisman, 1969. A technique for the analysis of transient seismic signals, *Bull. Seismol. Soc. Am., 59*, 427-444, 1969.

Dziewonski, A.M., T.-A. Chou, and J.H. Woodhouse, Determination of earthquake source parameters from waveform data for studies of global and regional seismicity, *J. Geophys. Res., 86*, 2825-2852, 1981.

Dziewonski, A. M., J. Mills, and S. Bloch, Residual dispersion measurements: a new method of surface wave analysis, *Bull. seism. Soc. Am.*, **62**, 129 - 139, 1972.

Egorkin, A.A., Levshin, A.L., and A.N. Yakobson, Study of the deep structure of the Barents Sea shelf by seismic surface waves. In Numerical modeling and analysis of geophysical processes, Comput. Seismology, 20, Allerton Press, N.-Y., 197-201, 1988.

Ekström, G., J. Tromp, and E.W.F. Larson, Measurements and global models of surface wave propagation, *J. Geophys. Res.*, *102*, 8137-8158, 1997.

Engdahl, E.R., van der Hilst, R. and Buland, R., Global teleseismic earthquake relocation with improved travel times and procedures for depth determination. *Bull. Seism. Soc. Am.*, **88**, 722-743, 1998.

Ewing, W.M., W.S. Jardetsky, and F. Press, *Elastic Waves in Layered Media*. McGraw-Hill, New York, 1957.

EXXON production research group, Tectonic map of the world, 1985.

Feng, C.C., and T. Teng, Three-dimensional crust and upper mantle structure of the Eurasian continent, *J. Geophys. Res.*, *88*, 2261-2272, 1983a.

Feng, C.C., and T. Teng, An error analysis of FTAN, *Bull. Seismol. Soc. Am.*, *73*, 143-156, 1983b.

Feng, R., J.S. Zhu, Y. Y. Ding, G.Y. Chen, Z. Q. He, S. B. Yang, H. N. Zhou, and K. Z. Sun, Crustal structure in China from surface waves, *Chin. Geophys.*, Engl. Transl., *2*, 273-289, 1983.

Franklin, J.N., Well-posed stochastic extensions of ill-posed linear problems, *J. math. Analysis Applic.*, **31**, 682-716, 1970.

Friederich, W., Propagation of seismic shear and surface waves in a laterally heterogeneous mantle by multiple forward scattering, *Geophys. J. Int.*, **136**, 180-204, 1998.

Gao, S., P.M. Davis, H. Liu, P.D. Slack, Y.A. Zorin, N.A. Logatchev, M. Kogan, P.D. Burkholder, and R.P. Meyer, Asymmetric upwarp of the asthenosphere beneath the Baikal rift zone, Siberia, *J. Geophys. Res.*, *99*, 15,319-15,330, 1994.

Geller, R. J. and S. Stein, Normal modes of a laterally heterogeneous body: a one-dimensional example, *Bull. Seism. Soc. Am.*, **68**, 103-116, 1978.

Gilbert, F. and G. E. Backus, A computational problem encountered in a study of the Earth's normal modes, *Proc. Fall Joint Computer Conference, 1968, of Am. Federation of Information Processing Soc.*, 1273-1277, 1969.

Golitzin, B.B., On dispersion and attenuation of surface seismic waves (in Russian), *Izv. Russ. Acad. Sci.*, *2*, 1912.

Grand, S. P. and D. V. Helmberger, Upper mantle shear structure beneath Asia from multi-bounce S waves, *Phys. Earth Planet. Int.*, **41**, 154-169, 1985.

Grand, S.P., R.D. van der Hilst, and S. Widiyantoro, Global seismic tomography: a snapshot of convection in the Earth, *GSA Today*, **7**,4, 1-7, 1997.

Griot, D.A., J.P. Montagner, and P. Tapponier, Surface wave phase velocity tomography and azimuthal anisotropy in Central Asia, *J. Geophys. Res.*, **103**, 21215-21232, 1998.

Griot, D.A., J.P. Montagner, and P. Tapponier, Confrontation of mantle seismic anisotropy with two extreme models of strain, in Central Asia, *Geoph. Res. Let.*, **25**, 1447-1450, 1998.

Gutenberg, B., Dispersion und extinktion von seismischen oberflachenwellen und der aufbau der obersten erdschechten, *Phys. Z.*, *25*, 377-381, 1924.

Gutenberg, B., Uber gruppengeschwindigkeit bei erbebebwellen, *Phys. Z.*, *27*, 111-114, 1926.

Gutenberg, B., and C.F. Richter, On seismic waves, *Beitr. Geophys.*, *47*, 73-131, 1936.

Guterch, A., M. Grad, R. Materzak, and E. Perchuć, Deep structure of the Earth's crust in the contact zone of the Paleozoic and Precambrian Platform of Poland (TTZ), *Tectonophysics*, *128*, 251-279, 1986.

Hearn, T.M. and Ni, J.F., P_n velocities beneath continental collision zones: the Turkish-Iranian plateau, *Geophys. J. Int.*, **117**, 273-283, 1994.

Hearn, T., N. Beghoul, and M. Barazangi, 1991. Tomography of the western United States from regional arrival times, *J. Geoph. Res.*, **96**, 16,369-16,381, 1991.

Herrin, E., and T. Goforth, Phase matched filters: application to the study of Rayleigh waves, *Bull. Seismol. Soc. Am.*, *67*, 1259, 1977.

Herrmann, R. B. (ed.), *Computer programs in Earthquake seismology*, Saint-Louis University, **2**, 1978.

Hill, R.I., I.H. Campbell, G.R. Davies, and R.W. Griffiths, Mantle plumes and continental tectonics, *Science*, *256*, 186-193, 1992.

Holt, W.E., Correlated crust and mantle strain fields in Tibet, *Geology*, *28*, 67-70, 2000.

Hurtig, E., G. Gräss, and R.-P. Oesburg, Velocity variation in the upper mantle beneath TE and EEP, *Tectonophysics*, *56*, 33-144, 1979.

James, M.B. and M.H. Ritzwoller, Feasibility of truncated perturbation expansions to approximate Rayleigh wave eigenfrequencies and eigenfunctions in heterogeneous media, *Bull. Seism. Soc. Am.*, **89**, 433-442, 1999.

Jeffreys, H., The effect on Love waves of heterogeneity in the lower mantle, *Mon. Not. R. Astron. Soc., Geophys. Suppl.*, *2*, 101-111, 1928.

Jeffreys, H., The surface waves of earthquakes, *Mon. Not. R. Astron. Soc., Geophys. Suppl.*, *3*, 253-261, 1935.

Jobert, N., and G. Jobert, An application of ray theory to the propagation of waves along a laterally heterogeneous spherical surface, *Geophys. Res. Lett.*, **10**, 1148-1151, 1983.

Jobert, N., B. Journet, G. Jobert, A. Hirn, and S.-K. Zhong, Deep structure of southern Tibet inferred from the dispersion of Rayleigh waves through a long-period seismic network, *Nature*, *313*, 386-388, 1985.

Johnson, L., and G. Brass, Marine arctic science capability making big strides, EOS, *Trans. Am. Geophys. Un.*, **79**, 345-349, 1998.

Kadinsky-Cade, K., Barazangi, M., Oliver, J. and Isacks, B., Lateral variations of high-frequency seismic wave propagation at regional distances across the Turkish and Iranian Plateaus, *J. Geophys. Res.*, **86**, 9377-9396, 1981.

Kanamori, H. and D. L. Anderson, Importance of physical dispersion in surface wave and free oscillation problems: review, *Rev. Geophys. Space Phys.*, **15**, 105-112, 1977.

Kazmin, V.G., Sbortshikov, I.M., Ricou, L.E., Zonenshain, L.P., Boulin, J. and Knipper, A.L., Volcanic belts as markers of the Mesozoic-Cenozoic active margin of Eurasia, *Tectonophysics*, **123**, 123-152, 1986.

Kennett, B.L.N., E.R. Engdahl, and R. Buland, Constraints on seismic velocities in the Earth from travel times, *Geophys. J. Int.*, **122**, 108-124, 1995.

Kijko, A., and B.J. Mitchell, Multimode Rayleigh-wave attenuation and Q in the crust of the Barents shelf, *J. Geoph. Res.*, **88**, 3315-3328, 1983.

Kim, W.-Y., V. V. Kazakov, A. G. Vanchugov, and D. W. Simpson, Broadband and array observations at low noise sites in Kazakhstan: Opportunities for seismic monitoring of a Comprehensive Test Ban Treaty, *Monitoring a Comprehensive Test Ban Treaty*, edited by E. S. Husebye and A.M. Dainty, pp. 467-482, Kluwer, Norwell, Mass., 1995.

Knopoff, L., Observation and inversion of surface wave dispersion, *Tectonophysics*, *13*, 497-519, 1972.

Knopoff, L., The thickness of the lithosphere from dispersion of surface waves, *Geophys. J. R. Astron. Soc.*, *74*, 55-81, 1983.

Knopoff, L., and F.-S. Chang, Upper mantle structure under the Tibetan Plateau, in *Geological and Ecological Studies of the Qinghai-Xizang Plateau*, vol. *1*, pp. 627-632, edited by Liu D.S., Gordon and Breach, New York, 1981.

Knopoff, L., and A.A. Fouda, Upper mantle structure under the Arabian Peninsula, *Tectonophysics*, *26*, 121-134, 1975.

Knopoff, L., and F.A. Schwab, Apparent initial phase of a source of Rayleigh waves, *J. Geophys. Res.*, *73*, 755-760, 1968.

Kozhevnikov, V. M., and M. P. Barmin, Dispersion curves of Rayleigh wave group velocities for several regions of the Asian continent, in *Izv. Akad. Nauk SSSR, Fiz. Zemli*, no. 9, 16-25, 1989.

Kozhevnikov, V. M., D. E. Lokshtanov, and M. P. Barmin, Shear-velocity structure of the lithosphere for nine large tectonic regions of the Asian continent, in *Izv. Akad. Nauk SSSR, Fiz. Zemli*, no. 1, 61-70, 1992.

Krueger, F., and K. Stammler, The German Regional Seismic Network (GRSN) used as mid- and long-period array, *Eur. Geophys. Soc. Newsl.*, *58*, 57, 1996.

Kunin, N. Y., *et al.*, Basement surface relief map, Inst. of Phys. of the Earth, Acad. of Sci., Minist. of Geol. of the Russ. Fed., Moscow, 1987.

Lander, A.V., A.L. Levshin, L.I. Ratnikova, and A.N. Yakobson, Peculiarities of the deep structure of Northern Eurasia from seismic surface wave data (in Russian), *Proc. Acad. Sci. USSR*, *285 (4)*, 845-848, 1985.

Lander, A. V., Dispersion characteristics of Rayleigh waves on the Asiatic Arctic shelf and structural features of the Laptev Sea, In Problems of Seismological Information Science, Comput. Seismology, 21, Allerton Press, NY, 142-145, 1989.

Landisman, M., A. Dziewonski, and Y. Sato, Recent improvements in the analysis of surface wave observations, *Geophys. J. R. Astron. Soc.*, *17*, 369-403, 1969.

Laske, G., Global observations of off-great-circle propagation of long-period surface waves, *J. Geophys. Res.*, *90*, 605-621, 1995.

Laske, G., and G. Masters, Constraints on global phase velocity maps from long-period polarization data, *J. Geophys. Res.*, *101*, 16,059-16,075, 1996.

Laske, G. and Masters, G., A global digital map of sediment thickness (abstract), *EOS Trans. AGU*, **78**,, F483, 1997.

Leach, R.R., D.B. Harris, and W.R. Walter, Phase matched filtering of after-shock sequences to detect Rayleigh waves in low SNR seismograms, *Proceedings of the 20th Annual Seismic Research Symposium on Monitoring a Comprehensive Test Ban Treaty*, DoD & DoE, 458-465, 1998.

Lerner-Lam, A. L., and T. H. Jordan, Earth structure from fundamental and higher-mode waveform analysis, *Geophys. J. R. Astron. Soc.*, *75*, 759-797, 1983.

Lévêque, J.-J., L. Rivera, and G.W. Wittlinger, On the use of checker-board test to assess the resolution of tomographic inversions, *Geophys. J. Int.*, *115*, 313-318, 1993.

Levshin, A., and K. A. Berteussen, Anomalous propagation of surface waves in the Barents Sea as inferred from NORSAR recordings, *Geophys. J. R. Astron. Soc.*, 56, 97-118, 1979.

Levshin, A.L., and M. H. Ritzwoller, Characteristics of surface waves generated by events on and near the Chinese nuclear test site, *Geophys. J. Int.*, *123*, 131-149, 1995.

Levshin, A.L. and M.H. Ritzwoller, Automated detection, extraction, and measurement of regional surface waves, *PAGEOPH*, in press, 2000.

Levshin, A. L., V.F. Pisarenko, and G. A. Pogrebinsky, On a frequency-time analysis of oscillations, *Ann. Geophys.*, *28*, 211-218, 1972.

Levshin, A. L., L. Ratnikova, and J. Berger, Peculiarities of surface wave propagation across central Eurasia, *Bull. Seismol. Soc. Am.*, *82*, 2464-2493, 1992.

Levshin, A. L., M. H. Ritzwoller, and L. I. Ratnikova, The nature and cause of polarization anomalies of surface waves crossing northern and central Eurasia, *Geophys. J. Int.*, *117*, 577-590, 1994.

Levshin, A.L., M.H. Ritzwoller, and J.S. Resovsky, Source effects on surface wave group travel times and group velocity maps, *Phys. Earth Planet. Int.*, **115**, 293 - 312, 1999.

Levshin, A.L., M.H. Ritzwoller, and S.S. Smith, Group velocity variations across Eurasia, in *Proceedings of the 18th Seismic Research Symposium on Monitoring a CTBT*, edited by J.F. Lewkowicz, J.M. McPhetres, and D.T. Reiter, pp. 70-79, Phillips Lab., Hanscom AFB, Mass., 1996.

Levshin, A.L., M.H. Ritzwoller, M.P. Barmin, A. Villasenor, New constraints on the Arctic crust and uppermost mantle: Surface wave group velocities, P_n, and S_n, *Phys. Earth Planet. Int.*, in press, 2000.

Levshin, A. L., T. B. Yanovskaya, A. V. Lander, B. G. Bukchin, M. P. Barmin, L. I. Ratnikova, and E. N. Its, *Seismic Surface Waves in a Laterally Inhomogeneous Earth*, edited by V. I. Keilis-Borok, Kluwer, Norwell, Mass., 1989.

Li, X.D., and B. Romanowicz, Global mantle shear velocity model developed using nonlinear asymptotic coupling theory, *J. Geophys. Res.*, *101*, 22245-22272, 1996.

Lognonné, P., Normal modes and seismograms in an anelastic rotating Earth, *J. Geophys. Res.*, **96**, 20309-20319, 1991.

Lognonné, P. and B. Romanowicz, Modelling of coupled normal modes of the Earth: the spectral method, *Geophys. J. Int.*, **102**, 365-395, 1990.

Lomax, A., and R. Snieder, The contrast in the upper mantle shear-wave velocity between the East European Platform and tectonic Europe obtained with genetic algorithm inversion of Rayleigh-wave group velocity dispersion, *Geophys. J. Int.*, *123*, 169-182, 1995.

Love, A.E.H., *Some Problems in Geodynamics*, Cambridge Univ. Press, New York, 1911. (Reprinted Dover, New York, 1967.)

Luh, P. C., Normal modes of a rotating, self gravitating inhomogeneous Earth, *Geophys. J. R. Astron. Soc.*, **38**, 187-224, 1974.

Lyon-Caen, H., Comparison of the upper mantle shear wave velocity structure of the Indian Shield and the Tibetan Plateau and tectonic implications, *Geophys. J. R. Astron. Soc.*, *86*, 727-749, 1986.

Madariaga, R. I., Toroidal free oscillations of the laterally heterogeneous Earth, *Geophys. J. R. Astron. Soc.*, **27**, 81-100, 1972.

Makris, J., and A. Ginzburg, The Afar depression: Transition between continental rifting and sea floor spreading, *Tectonophysics. 141*, 199-214, 1987.

Mantovani, E., G. Nolet, and G. F. Panza, Lateral heterogeneity in the crust of the Italian region from regionalized Rayleigh-wave group velocities, *Ann. Geophys., 3*, 519-530, 1985.

Marquering, H., R. Snieder, and G. Nolet, Waveform inversions and the significance of surface mode coupling, *Geophys. J. Int.*, **124**, 258-270, 1996.

Masters, G., S. Johnson, G. Laske, and H. Bolton, A shear-velocity model of the mantle, *Philos. Trans. R. Soc. London, Ser. A. 354*, 1385-1411, 1996.

McNamara, D.E., Owens, T.J., Silver, P.G. and Wu, F., Shear wave anisotropy beneath the Tibetan Plateau, *J. Geophys. Res.*, **98**, 12003-12017, 1994.

McNamara, D.E., T.J. Owens, and W.R. Walter, Observations of regional phase propagation across the Tibetan Plateau, *J. Geophys. Res., 100*, 22,215-22,229, 1995.

Menke, W. *Geophysical Data Analyses: Discrete Inverse Theory*. New York, Academic Press, 1989.

Mindevalli, O.Y., and B. J. Mitchell, Crustal structure and possible anisotropy in Turkey from seismic surface wave dispersion, *Geophys. J. Int., 98*, 93-106, 1989.

Mohr, P., Ethiopian flood basalt province, *Nature, 303*, 577-584, 1983.

Molnar, P., A review of geophysical constraints on the deep structure of the Tibetan plateau, the Himalaya and the Karakoram, and their tectonic implications., *Phil. Trans. R. Soc. Lond.*, A326: 33-88, 1988.

Molnar, P., P. England, and J. Martinod, Mantle dynamics, uplift of the Tibetan Plateau, and the Indian Monsoon, *Rev. Geophys., 31*, 357-396, 1993.

Montagner, J.P., and H.C. Nataf, A simple method for inverting the azimuthal anisotropy of surface waves, *J. Geophys. Res., 91*, 511-520, 1986.

Montagner, J.P., and T. Tanimoto, Global anisotropy in the upper mantle inferred from the regionalization of phase velocities, *J. Geophys. Res., 95*, 4794-4819, 1990.

Montagner, J.P., and T. Tanimoto, Global upper mantle tomography of seismic velocities and anisotropies, *J. Geophys. Res., 96*, 20337-20351, 1991.

Mooney, W.D., G. Laske, and G. Masters, CRUST 5.1: A global crustal model at 5 degrees by 5 degrees, *J. Geophys. Res.*, **103**, 727-747, 1998.

Morris, S. P. and R. J. Geller, Toroidal modes of a simple laterally heterogeneous sphere, *Bull. Seism. Soc. Am.*, **72**, 1155-1166, 1982.

Mueller, S., and C. Sprecher, Upper mantle structure along a profile through the eastern Alps from Rayleigh wave dispersion, in *Alps, Apennines, Hellenides*, edited by H. Closs, *Int. Geodyn. Comm. Sci. Rep., 38*, 40-44, 1978.

Muyzert, E., and R. Snieder, The influence of errors in source parameters on phase velocity measurements of surface waves, *Bull. Seismol. Soc. Am., 86*, 1863-1872, 1996.

Nakanishi, I., and D. L. Anderson, World-wide distribution of group velocity of mantle Rayleigh waves as determined by spherical harmonic inversion, *Bull. Seismol. Soc. Am.*, **72**, 1185-1194, 1982.

Nataf, H.-C., and Y. Ricard, 3SMAC: An a priori tomographic model of the upper mantle based on geophysical modeling, *Phys. Earth Planet. Inter., 95*, 101-122, 1996.

Neuenhofer, H., F. Mariller, and G. F. Panza, Crust and upper mantle structure in the Bohemian Massif from the dispersion of Rayleigh waves, *Gerlands Beitr. Geophys., 90*, 514-520, 1981.

Nishimura, C.E., and D.W. Forsyth, Rayleigh wave phase velocities in the Pacific with implications for azimuthal anisotropy and lateral heterogeneities, *Geophys. J. Int., 94*, 479-501, 1988.

Nolet, G., The upper mantle under western Europe inferred from the dispersion of Rayleigh wave modes, *J. Geophys., 43*, 265-276, 1977.

Nolet, G., Wave form tomography, in *Seismic Tomography with Applications in Global Seismology and Exploration Geophysics*, edited by G. Nolet, pp. 301-322, D. Reidel, Norwell, Mass., 1987.

Oliver, J., A summary of observed surface wave dispersion, *Bull. Seismol. Soc. Am., 52*, 81-86, 1962.

Panza, G.F., H. Neuenhofer, and G. Calcagnile, Contribution to phase velocity investigation of Rayleigh waves in middle Europe, *Pure Appl. Geophys.*, *116*, 1299-1306, 1978.

Panza, G. F., S. Mueller, and G. Calcagnile, The gross features of the lithosphere-asthenosphere system in Europe from seismic surface waves and body waves, *Pure Appl. Geophys.*, *118*, 1209-1213, 1980.

Parker, R.L., *Geophysical Inverse Theory*, Princeton, NJ, Princeton University Press, 1994.

Patton, H., Crustal and upper mantle structure of the Eurasian continent from the phase velocity and Q of surface waves. *Rev. Geophys.*, *18*, 605-625, 1980.

Pavlis G., H. Al-Shukri, H. Mahdi, and D. Repin, JSP arrays and networks in Central Asia, *IRIS Newsl.*, *XIII (2)*, 10-12, 1994.

Pedersen, H. A., M. Camillo, and N. Balling, Changes in the lithospheric structure across the Sorgenfrei-Tornquist Zone inferred from dispersion of Rayleigh waves, *Earth Planet. Sci. Lett.*, *128*, 37-46, 1994.

Pekeris, C. L., Accuracy of the Earth-flattening procedure in propagation around a sphere, *Phys. Rev.*, **70**, 519-522, 1946.

Pines, I., T.-L. Teng, and R. Rosenthal, A surface wave dispersion study of the crustal and upper mantle structure of China, *J. Geophys. Res.*, *85*, 3829-3844. 1980.

Pollitz, F.F., Surface wave scattering from sharp lateral discontinuities, *J. Geophys. Res.*, **99**, 21,891-21,909, 1994.

Press, F., Determination of crustal structure from phase velocity of Rayleigh waves, I, Southern California, *Geol. Soc. Am. Bull.*, *67*, 1647-1658, 1956.

Press, F., M. Ewing, and J. Oliver, Crustal structure and surface wave dispersion in Africa, *Bull. Seismol. Soc. Am.*, *46*, 97-103, 1956.

Pulliam, J., and R. Snieder, Ray perturbation theory, dynamic ray tracing and the determination of Fresnel zones, *Geoph. J. Int.*, **135**, 463-469.

Quinlan, D.M., Datascope: A relational database system for scientists, *Eos Trans. AGU*, *75 (44)*, Fall Meet. Suppl., F431, 1994.

Rezapour, M. and R.G. Pearce, Bias in surface wave magnitude M_s due to inadequate distance corrections, *Bull. Seism. Soc. Am.*, **88**, 43 - 61, 1998.

Rial, J.A. and M.H. Ritzwoller, Characteristics of Lg propagation across South America, *Geophys. Jour. Int.*, **131**, 401-408, 1997.

Ritzwoller, M.H., and E.M. Lavely, Three-dimensional seismic models of the Earth's mantle, *Rev. Geophys.*, *33*, 1-66, 1995.

Ritzwoller, M.H. and A.L. Levshin, Eurasian surface wave tomography: Group velocities, *J. Geophys. Res.*, **103**, 4839 - 4878 1998.

Ritzwoller, M.H. and A.L. Levshin, Estimating shallow shear velocities with marine multi-component seismic data, *Geophysics*, submitted, June, 2000.

Ritzwoller, M.H., A.L. Levshin, and L.I. Ratnikova, Surface wave tomography across Tibet, *Eos Trans. AGU*, *77 (46)*, Fall Meet. Suppl., F675, 1996a.

Ritzwoller, M.H., A.L. Levshin, L.I. Ratnikova, Intermediate period group velocity maps across Central Asia, Western China, and parts of the Middle East, *Geophys. J. Int.*, **134**, 315-328, 1998.

Ritzwoller, M.H., A.L. Levshin, D.M. Tremblay, and M.B. James, Broadband surface wave dispersion across the Antarctic Plate, *Eos Trans. Am. Geophys. Un.*, *77* (46), Fall Meet. Suppl., F477, 1996c.

Ritzwoller, M.H., A.L. Levshin, L.I. Ratnikova, and D.M. Tremblay, High resolution group velocity variations across Central Asia, in *Proceedings of the 18th Seismic Research Symposium on Monitoring a CTBT*, edited by J.F. Lewkowicz, J.M. McPhetres, and D.T. Reiter, pp. 98-107, Phillips Lab., Hanscom AFB, Mass., 1996b.

Ritzwoller, M.H., A.L. Levshin, S.S. Smith, and C.S. Lee, Making accurate continental broadband surface wave measurements, in *Proceedings of the 17th Seismic Research Symposium on Monitoring a CTBT*, edited by J.F. Lewkowicz, J.M. McPhetres, and D.T. Reiter, pp. 482-490, Phillips Lab., Hanscom AFB, Mass., 1995.

Ritzwoller, M.H., M.P. Barmin, A. Villaseñor, A.L. Levshin, E.R. Engdahl, W. Spakman, and J. Trampert, Construction of a 3-D P and S model of the crust and upper mantle to improve regional locations in W. China, Central Asia, and parts of the Middle East, *Proceedings of the 21th Annual Seismic Research Symposium on Monitoring a Comprehensive Test Ban Treaty*, DoD & DoE, 656-665, 1999.

Rodi, W.L., P. Glover, T.M.C. Li, and S.S. Alexander, A fast, accurate method for computing group-velocity partial derivatives for Rayleigh and Love modes, *Bull. Seis. Soc. Am.*, **65**, 1105-1114, 1975.

Romanowicz, B.A., Constraints on the structure of the Tibet Plateau from pure-path phase velocities of Love and Rayleigh waves, *J. Geophys. Res.*, *87*, 6865-6883, 1982.

Romanowicz, B., M. Cara, J. F. Fels and D. Rouland, Geoscope: A French initiative in long period, three component, global seismic networks, *Eos, Trans. AGU*, *65*, 753-754, 1984.

Russell, D. W., R. B Herrman, and H. Hwang, Application of frequency-variable filters to surface wave amplitude analysis, *Bull. Seismol. Soc. Am.*, *78*, 339-354, 1988.

Saito, M., Theory for the elastic-gravitational oscillation of a laterally heterogeneous Earth, *J. Phys. Earth*, **19**, 259-270, 1971.

Sambridge, M., J. Braun, and H. McQueen, Geophysical parameterization and interpolation of irregular data using natural neighbors, *Geophys. J. Int.*, **122**, 837-857, 1995.

Seber, D., Vallve, M., Sandvol, E.A., Steer, D.N. and Barazangi, M., Middle East tectonics: applications of geographic information systems (GIS), 1997.

Sloan, S.W., A fast algorithm for constructing Delaunay triangulation in the plane, *Adv. Eng. Software*, **9** (1), 34-55, 1987.

Smith, M.L., and F.A. Dahlen, The azimuthal dependence of Love and Rayleigh wave propagation in a slightly anisotropic medium, *J. Geophys. Res.*, **78**, 3321-3333, 1973.

Snieder, R., Large-scale waveform inversion of surface waves for lateral heterogeneity, 2, Application to surface wave in Europe and Mediterranean, *J. Geophys. Res.*, *93*, 12067-12080, 1988.

Snieder, R. Global inversions using normal modes and long-period surface waves, in *Seismic Tomography: Theory and Practice*, edited by H.M. Iyer and K. Hirahara, pp. 23-63, Chapman and Hall, New York, 1993.

Snieder, R., and H. Paulssen, Future deployment of the NARS array, in *Proceedings of the Europrobe Symposium, Jablonna 1991*, edited D.G. Gee and M. Beckholmen, pp. 129-132, C Warsawa, 1993.

Spackman, W., Delay-time tomography of the upper mantle below Europe, Mediterranean, and Asia Minor, *Geophys. J. Int.*, *107*, 309-332, 1991.

Spackman, W., S. Van der Lee, and R. Van der Hilst, Travel-time tomography of the European-Mediterranean mantle down to 1400 km, *Phys. Earth Planet. Inter.*, *79*, 3-74, 1993.

Spakman, W., and H. Bijwaard, Irregular cell parametrization of tomographic problems, *Ann. Geophys.*, **16**, 18, 1998.

Spakman, W., and H. Bijwaard, Irregular cell parametrization of tomographic inverse problems, *PAGEOPH*, in press, 2000.

Stange, S., and W. Friederich, Surface wave dispersion and upper mantle structure beneath southern Germany from joined inversion of network recorded teleseismic events, *Geophys. Res. Lett.*, *20*, 2375-2378, 1993.

Stevens, J.L., and S.M. Day, The physical basis for m_b : M_s and variable frequency magnitude methods for earthquake/explosion discrimination, *J. Geophys. Res.*, *90*, 3009-3020, 1985.

Stevens, J.L., and K.L. McLaughlin, Improved methods for regionalized surface wave analysis, *Proceedings of the 17th Annual Seismic Research Symposium on Monitoring a CTBT*, 171-180, 1997.

Stevens, J.L. and K.L. McLaughlin, Optimization of surface wave identification and measurement, *PAGEOPH*, in press, 2000.

Stoneley, R., The effect of the ocean on Rayleigh waves, *Mon. Not. R. Astron. Soc., Geophys. Suppl.*, *1*, 349-356, 1926.

Stoneley, R., Dispersion of waves in a double surficial layer, *Mon. Not. R. Astron. Soc., Geophys. Suppl.*, *2*, 527-531, 1928.

Su, W., R. L. Woodward, and A.M. Dziewonski, Degree 12 model of shear velocity heterogeneity in the mantle, *J. Geophys. Res.*, *99*, 6945-6980, 1994.

Suetsugu, D., and I. Nakanishi, Surface waves tomography for the upper mantle beneath the Pacific ocean. Part I: Rayleigh wave phase velocity distribution, *J. Phys. Earth*, **33**, 345-368, 1985.

Sultanov, D.D., J.R. Murphy, and Kh.D. Rubinstein, A seismic source summary for Soviet peaceful nuclear explosions, *Bull Seismol. Soc. Am.*, **89**, 640-647, 1999.

Takeuchi, H. and M. Saito, Seismic surface waves, *Methods Comput. Phys.*, **11**, 217-295, 1972.

Tarantola, A., and A. Nersessian, Three-dimensional tomography without block, *Geophys. J. R. astr. Soc.*, *76*, 299-306, 1984.

Tanimoto, T., and D. L. Anderson, Lateral heterogeneity and azimuthal anisotropy of the upper mantle: Love and Rayleigh waves 100-250 s, *J. Geophys. Res.*, *90*, 1842-1858, 1985.

Tikhonov, A.N., On the solution of improperly posed problems and the method of regularization, *Dokl. Akad. Nauk SSSR*, **151**, 501, 1963.

Trampert, J., Global seismic tomography; the inverse problem and beyond, *Inverse Problems*, **14**, 371-385, 1998.

Trampert, J., and J. Woodhouse, Global phase velocity maps of Love and Rayleigh waves between 40 and 150 seconds, *Geophys. J. Int.*, *122*, 675-690, 1995.

Trampert, J., and J. Woodhouse, Global azimuthal anisotropy, *Eur. Geophys. Soc. Newsl.*, *58*, 57, 1996.

Vaccari, F., and G. F. Panza, v_p/v_s estimation in south-western Europe from p-wave tomography and surface wave tomography analysis, *Phys. Earth Planet. Inter.*, *78*, 229-237, 1993.

van der Hilst, R.D, S. Widiyantoro, and E.R. Engdahl, Evidence for deep mantle circulation from global tomography, *Nature*, **386**, 578-584, 1997.

Vdovin, O., J.A. Rial, M.H. Ritzwoller, and A.L. Levshin, Surface wave inversion of the South American lithosphere (SISAL), *Eos Trans. AGU*, *77 (46)*, Fall Meet. Suppl., F464, 1996.

Vdovin, O., J.A. Rial, A.L. Levshin, and M.H. Ritzwoller, Group-velocity tomography of South America and the surrounding oceans, *Geophys. J. Int.*, **136**, 324-340, 1999.

Vdovin, O.Y., Surface wave tomography of South America and Antarctica, *Ph. D. Thesis*, Department of Physics, University of Colorado at Boulder, 1999.

Vernon, F., The Kyrghyz Seismic Network, *IRIS Newsl.*, *13*, 7-8, 1994.

Vernon, F., Mellors, R.J., J. Berger, A.M. Al-Amri, and J. Zollweg, Initial results from the deployment of broad-band seismometers in the Saudi Arabian Shield, in *Proceedings of the 18th Seismic Research Symposium on Monitoring a CTBT*, edited by J.F. Lewkowicz, J.M. McPhetres, and D.T. Reiter, pp. 108-117, Phillips Lab., Hanscom AFB, Mass., 1996.

Villaseñor, A., M.H. Ritzwoller, A.L. Levshin, M.P. Barmin, E.R. Engdahl, W. Spakman, and J. Trampert, Shear velocity structure of Central Eurasia from inversion of surface wave velocities, *Phys. Earth Planet. Int.*, in press, 2000.

Wessel, P., and W.H. F. Smith, Free software helps map and display data, *Eos Trans. AGU*, *72*, 441, 1991.

Wessel, P., and W.H. F. Smith, New version of the Generic Mapping Tools released, *Eos Trans. AGU*, *76*, 329, 1995.

White, R., and D. McKenzie, Magmatism at rift zones: The generation of volcanic continental margins and flood basalts, *J. Geophys. Res.*, *94*, 7685-7729, 1989.

Wier, S., Surface wave dispersion and Earth structure in south-eastern China, *Geophys. J. R. Astron. Soc.*, *69*, 33-47, 1982.

Windley, B.F. and Allen, M.B., Mongolian plateau: Evidence for a late Cenozoic mantle plume under central Asia, *Geology*, **21**, 295-298, 1993.

Woodhouse, J. H., On Rayleigh's principle, *Geophys. J. R. Astron. Soc.*, **46**, 11-22, 1976.

Woodhouse, J. H., The calculation of the complete normal mode spectrum of the Earth using finite difference methods, Seismic Discrimination Semiannual Technical Summary, Lincoln Laboratory, MIT, March 31, 1981.

Woodhouse, J. H., The calculation of the eigenfrequencies and eigenfunctions of the free oscillations of the Earth and the Sun, in: *Seismological Algorithms* (D. J. Doornbos, ed.), 321-370, 1988.

Woodhouse, J. H. and F. A. Dahlen, The effect of a general aspherical perturbation on the free oscillations of the Earth, *Geophys. J. R. Astron. Soc.*, **53**, 335-354, 1978.

Wu, F.T., and A. Levshin, Surface wave group velocity tomography of East Asia, *Phys. Earth Planet. Inter.*, *84*, 59-77, 1994.

Wu, F.T., A.L. Levshin, and V.M. Kozhevnikov, Rayleigh wave group velocity tomography of Siberia, China, and the vicinity, *Pure Appl. Geophys.*, *149*, 447-473, 1997.

Yanovskaya, T.B., and P.G. Ditmar, Smoothness criteria in surface wave tomography, *Geophys. J. Int.*, *102*, 63-72, 1990.

Yanovskaya, T. B., G. F. Panza, P. G. Ditmar, P. Suhadolc, and S. Mueller, Structural heterogeneity and anisotropy based on 2-D phase velocity patterns of Rayleigh waves in western Europe, *Atti Acad. Naz. Lincei*, *1*, 127-135, 1990.

Zeng, Y., T.-L. Teng, and K. Aki, Surface wave mapping of the crust and upper mantle in the Arctic Region, *Bull. Seismol. Soc. Am.*, *79*, 1520-1541, 1989.

Zhang, Y.-S., Three-dimensional velocity structure beneath East Asia and its tectonic implication, *Mantle Dynamics and Plate Interactions in East Asia, Geophys. Monogr. Ser.*, edited by M.F.J. Flower and S.-L. Chung, AGU, Washington, D.C., in press, 1997.

Zhang, Y.-S., and T. Lay, Global surface wave phase velocity variations, *J. Geophys. Res.*, **101**, 8415-8436, 1996.

Zhang, Y.-S., and T. Tanimoto, High resolution global upper mantle structure and plate tectonics, *J. Geophys. Res.*, *98*, 9793-9823, 1993.

Zhao, L.-S., and J. Xie, Lateral variations in compressional velocities beneath the Tibetan Plateau from P_n travel-time tomography, *Geophys. J. Int.*, *115*, 1070-1084, 1993.

Zhou, H., A high-resolution P wave model for the top 1200 km of the mantle, *J. Geophys. Res.*, **101**, 27791-27810, 1996.

Zielhuis, A., and G. Nolet, Shear velocity variations in the upper mantle beneath central Europe, *Geophys. J. Int.*, *117*, 695-715, 1994.

Zonenshain, L. P., M. I. Kuzmin, and L. M. Natapov, *Geology of the USSR: A Plate-Tectonic Synthesis, Geodyn. Ser.*, vol. 21, edited by B. M. Page, AGU, Washington, D. C., 1990.

Ch. 11

Abo-Zena, A.M., 1979, Dispersion function computations for unlimited frequency values, *Geophys. J. R. astr. Soc.*, **58**, 91-105.

Akal, T., J.M. Berkson, 1986, eds., *Ocean Seismo-Acoustics: Low Frequency Underwater Acoustics*, Plenum Press, New York, Proc. SACLANT ASW Research Center Symposium, La Spezia, Italy, June 1985.

Aki, K., and P.G. Richards, 1980, *Quantitative Seismology: Theory and Methods*, I, W. H. Freeman and Co, San Francisco.

Al-Husseini, M.I., J.B. Glover, and B.J. Barley, 1981, Dispersion patterns of the ground roll in eastern Saudi Arabia, *Geophysics*, **46**, 121-137.

Bachman, R.T., 1983, Elastic anisotropy in marine sedimentary rocks, *J. Geophys. Res.*, **88**, 539-545.

Barmin, M.P., A.L. Levshin, and M.H. Ritzwoller, 2000, A fast and reliable method for surface wave tomography, *Pure and Appl. Geophys.*, in press.

Bautista, E. O., R.D. Stoll, 1995, Remote determination of in situ sediment parameters using Love waves, *J. Ac. Soc. Am.*, **98**, 1090-1096.

Bibee, D.L. and L.M. Dorman, 1991, Implications of deep-water seismometer array measurements for Scholte wave propagation, in J.M. Hovem *et al.* (eds.), *Shear Waves in Marine Sediments*, Kluwer Academic Publ., Dordrecht, Netherlands, 395-402.

Blonk, B., 1995, Removal of scattered surface waves from seismic data, *Thesis Technishe Universiteit Delft.*

Caldwell, J., 1999, Marine multi-component seismology,*The Leading Edge*, **18**, no. 11, 1274-1282.

Cara, M., 1973, Filtering of dispersed wave trains, *Geophys. J. R. astr. Soc.*, **33**, 65 - 80, 1973.

Dosso, S. E., and G.H. Brooke, 1995, Measurement of seismo-acoustic ocean-bottom properties in the high Arctic,*J. Ac. Soc. Am.*, **98**, 1657-66.

Dziewonski, A.M., Bloch, S., and M. Landisman, 1969. A technique for the analysis of transient seismic signals, *Bull. seism. Soc. Am.*, **59**, 427 - 444.

Ernst, F., and G. Herman, 1998, Removal of guided waves from seismic data in laterally varying media, *Wave Motion*, **28**, 173-189.

Essen, H.-H., I. Grevemeyer, R. Herber, and W. Weigel, 1998, Shear-wave velocity in marine sediments on young oceanic crust: constraints from dispersion of Scholte waves, *Geophys. J. Int.*, **132**, 227-234.

Ewing, J., A. Carter, G. H. Sutton and N. Barstow, 1992, Shallow Water sediment properties derived from high-frequency shear and interface waves, *J. Geophys. Res*, **9**, 4739-4762.

Frivik, S. A., and J.M. Hovem, 1995, Geotechnical investigation using interface waves for determination of shear properties in the upper seafloor, *Challenges of Our Changing Global Env.*, Conf. Proc., OCEANS 95 MTS/IEEE, 1840-5, 1995.

Gabriels, P., R. Snieder, and G. Nolet, 1987, In situ measurements of shear-wave velocity in sediments with higher-mode Rayleigh waves, *Geoph. Prosp.*, **35**, 187-196.

Gaiser, J.E., 1996, Multicomponent V_p/V_s correlation analysis, *Geophysics*, **61**, 1137-1149.

Hamilton, E. L., 1979, V_p/V_s and Poisson's ratios in marine sediments and rocks, *J. Acoust. Soc. Am.*, **66** 1093-1101.

Hamilton, E.L., 1980, Geoacoustic modeling of the sea floor, *J. Acoust. Soc. Am.*, **68**, 1313-1340.

Harvey, D.J., 1981, Seismogram synthesis using normal mode decomposition: the locked mode approximation, *Geophys J. R. Astron. Soc.*, **66**, 37-69.

Haskell, N.A., 1953, The dispersion of surface waves on multilayered media, *Bull. Seism. Soc. Am.*, **43**, 17-34.

Herrmann, R.B. (Ed.), 1978, *Computer programs in earthquake seismology*, **2**, St. Louis University.

Herrmann, R.B., and D.R. Russell, 1990, Ground roll: Rejection using adaptive phase-matched filters, *Geophysics*, **55**, 776-781.

Hovem, J.M., M.D. Richardson, and R.D. Stoll, 1991, eds., *Shear Waves in Marine Sediments*, Kluwer Academic Publishers, Dordrecht, 1992, Proc. Conference on Shear Waves in Marine Sediments, La Spezia, Italy, October 1990.

Kawashima, S., M. Kimura, 1998, Determination of shear wave velocity profile using Scholte waves in marine sediments, *Jpn. J. Appl. Phys.*, **1**, Regul. Pap., Short Notes Rev. Pap., v.37, 3156-60.

Kennett, B.L.N., 1983, *Seismic wave propagation in stratified media*, Cambridge University Press.

Kennett, B. L. N., 1984, Guided-wave propagation in laterally varying media I theoretical development, *Geophys. J. R. Astron. Soc.*,**79**, 235-255.

Knopoff, L.,1972, Observation and inversion of surface wave dispersion, *Tectonophysics*, **13**, 497-519.

Levshin, A.L., Pisarenko, V.F., and G.A. Pogrebinsky, 1972, On a frequency-time analysis of oscillations, *Ann. Geophys.*, **28**, 211 - 218.

Levshin, A.L., T.B. Yanovskaya, A.V. Lander, B.G. Bukchin, M.P. Barmin, L.I. Ratnikova, and E.N. Its, 1989, *Seismic surface waves in a laterally inhomogeneous Earth*, (ed. V.I. Keilis-Borok), Kluwer Publ., Dordrecht.

Mari, J.L.,1984, Estimation of static correction for shear-wave profiling using the dispersion properties of Love waves, *Geophysics*, **49**, 1169-1179.

Marsden, D., 1993, Static corrections - A review, Part I, II, and III, *The Leading Edge*, **12**, no. 1-3.

Meissner, R., H. Stumpel, and F. Theilen, 1985, Shear wave studies in shallow sediments, in *Handbook of Geophysical Exploration*, ed. by G. Dohr, Geophysical Press, London, pp. 224-253.

Neigauz, M.G., and G.V. Shkadinskaya, 1972, Method for calculating surface wave Rayleigh waves in a vertically inhomogeneous half-space, in *Computational Seismology* (Ed. V.I. Keilis-Borok), Consultants Bureau, New York, 88-92.

Nolet, G., and L.M. Dorman, 1996, Waveform analysis of Scholte modes in ocean sediment layers, *Geophys. J. Int.*, **125**, 385-96.

Odom, R.I., M. Park, J.A. Mercer, R.S. Crosson, and P. Paik, 1996, Effects of transverse isotropy on modes and mode coupling in shallow water, *J. Acoust. Soc. Am.*, **100**, 2079-2092.

Park, C.B., R.D. Miller, and J. Xia, 1999, Multichannel analysis of surface waves, *Geophysics*, **64**, 800-808.

Purnell, 1992, Imaging beneath a high-velocity layer using converted waves, *Geophysics*, **57**, 1444-1452.

Rauch, D., 1986, On the role of bottom interface waves in ocean seismoc-acoustics: A review, in Akal, T. and J.M. Berkson (eds.), *Ocean Seismo-Acoustics: Low Frequency Underwater Acoustics*, 623-641.

Ritzwoller, M.H. and E.M. Lavely, 1995, Three-dimensional seismic models of the Earth's mantle, *Revs. of Geophys.*, **33**, 1-66.

Ritzwoller, M.H. and A.L. Levshin, 1998, Eurasian surface wave tomography: Group velocities, *J. Geophys. Res.*, **103**, 4839 - 4878.

Rodi, W.L., P. Glover, T.M.C. Li, and S.S. Alexander, 1975, A fast, accurate method for computing group-velocity partial derivatives for Rayleigh and Love modes, *Bull. Seis. Soc. Am.*, **65**, 1105-1114.

Saatçilar, R., and N. Canitez, 1988, A method for ground-roll elimination, *Geophysics*, **53**, 894-902.

Scholte, J.G.J., 1958, Rayleigh waves in isotropic and anisotropic elastic media, *Meded. en Verhand. KNMI*, **72**, 9-43.

Schwab, F., and L. Knopoff, 1972, Fast surface wave and free mode computations, in *Methods in Computational Physics*, **11**, 87-180, ed. B.A. Bolt, Academic Press, New York.

Shieh, C., and R. Herrmann, 1990, Ground roll: rejection using a polarization filter, *Geophysics*, **55**, 1216-1222.

Snieder, R., 1987, Surface wave holography, in *Seismic tomography, with applications in global seismology and exploration geophysics*, ed. G. Nolet, 323-337, Reidel, Dordrecht.

Smith, D.T., 1986, Geotechnical characteristics of the sea bed related to seismo-acoustics, in Akal, T. and J.M. Berkson (eds.), *Ocean Seismo-Acoustics: Low Frequency Underwater Acoustics*, 483-500.

Stokoe, K.H., and B.L. Rosenblad, 1999, Offshore geotechnical investigations with shear waves, *1999 Offshore Technology Conference*, Houston, Texas, 3-6 May, OTC 10823, 1-9.

Stoll, R.D., 1989, *Sediment Acoustics*, Springer - Verlag, New York.

Stoll, R.D., G.M. Bryan, R. Flood, D. Chayes, and P. Manley, 1988, Shallow seismic experiments using shear waves, *J. Acoust. Soc. Am.*, **83**, 93-102.

Stoll, R.D., E. Bautista, and R. Flood, New tools for studying sea-floor geotechnical and geoacoustic properties, *J. Acoust. Soc. Am.*, **96**, 2937-2944, 1994a.

Stoll, R.D., G.M. Bryan, and E. Bautista, 1994b, Measuring lateral variability of sediment geoacoustic properties, *J. Acoust. Soc. Am*, **96**, 427-438.

Vdovin, O., J.A. Rial, A.L. Levshin, and M.H. Ritzwoller, 1999, Group-velocity tomography of South America and the surrounding oceans, *Geophys. J. Int.*, **136**, 324-340.

Woodward, R.L. and G. Masters, 1991, Upper mantle structure from long-period differential travel times and free oscillation data, *Geophys. J. Int.*, **109**, 275-293.

Xia, J., R. Miller, and C. Park, 1999, Estimation of shear velocity by inverting Rayleigh wave phase velocity, *Geophysics*, **64**, 691-700.

Zhu, X., Altan S., and J. Li, 1999, Recent advances in multi-component processing, *The Leading Edge*, **18**, no. 11, 1283-1288.